Experiments in Nonlinear Optics with Epsilon-Near-Zero Materials

Mohammad Zahirul Alam

A thesis submitted to the University of Ottawa in partial fulfillment of the requirements for the degree of Doctor of Philosophy in Physics.

Ottawa-Carleton Institute of Physics, Department of Physics,
University of Ottawa
May, 2020

To my parents, Nasrin Akther and Golam Kibria, without whose continuous encouragement and numerous sacrifices I would have been a day labourer in the Middle East.

In memory of my late grandfather Nurul Haque.

ABSTRACT

Nonlinear optics is the study of interactions of materials with intense light beams made possible by the invention of laser. Arguably the most trivial but technologically most important nonlinear optical effect is the intensity-dependent nonlinear refraction: an intense light beam can temporarily and reversibly change the refractive index of a material. However, the changes to the refractive index of a material due to the presence of a strong laser beam are very weak—maximum on the order of 10^{-3}—and tend to be a small fraction of the linear refractive index. It must be noted that at optical frequencies vacuum has a refractive index of 1 and glass has a refractive index of 1.5. Thus, one of the foundational assumptions of nonlinear optics is that the nonlinear optical changes to material properties are always a small perturbation to the linear response. In the 58-year history of nonlinear optics, one of the overarching themes of research has been to find ways to increase the efficiency of nonlinear interactions.

This thesis is a collection of six manuscripts motivated by our experimental finding that at least in a certain class of materials the above long-standing view of nonlinear optics does not necessarily hold true. We have found that in a material with low refractive index, known as an epsilon-near-zero material or ENZ material, the nonlinear changes to the refractive index can be a few times larger than the linear refractive index, i.e.

the nonlinear response becomes the dominant response of the material in the presence of an intense optical beam.

We believe that the results presented in this thesis collectively make a convincing case that ENZ materials are a promising platform for nonlinear nano-optics.

ACKNOWLEDGEMENTS

I want to start by thanking my advisor and mentor Professor Robert W. Boyd for his unwavering support for me through many ups and downs. He continues to teach me how to ask the right questions and the importance of revising and re-revising my thoughts until I can express them with clarity.

I want to thank all the members of the Boyd lab and the CERC group, past and present, who made it such a special place to learn and ask questions. I want to particularly thank Israel De Leon and Jeremy Upham for guiding me during my early days in the lab. I learned half of what I know from my conversations with Giulio Vampa, Robert Fickler, Peter Banzer, Enno Giesse, Sebastian Schulz, Orad Reshef, Ebrahim Karimi, Omar Magaña-Loaiza, Lisa Ackermann, Yiyu Zhou, Saumya Choudhary, Filippo Miatto, Mikko Huttunen, Rasoul Alaee, J. Upham, Akbar Safari, Kashif Awan, and Samuel Lemieux. Every one of these conversations was extremely rewarding. I am also indebted to all scientists who have visited our group in Ottawa over the last eight years. Perhaps the most exciting highlight of my graduate education has been the discussion sessions organized by Bob in his office with most of the great optical physicists of the current era.

A particular thanks to my office mate Akbar Safari for teaching me what order and organization really mean, and for his long-standing support, especially during the toughest of times.

I fondly recall those early days when Kashif and I used to debate about world politics – such wonderful distraction from science.

I am forever indebted to my wife Fatima Uddin for her patience and sacrifices during the very challenging last year of my graduate studies.

Above all, I want to thank my parents for making the decision to move to Dhaka, Bangladesh – roughly four years after I was born in an aspiring village – so that I could receive a better education. They also supported me by agreeing to let me build my own destiny in Canada after withdrawing consecutively from the premier medical college and the premier engineering school of Bangladesh. I am forever indebted to my brother for his generosity, sacrifices and continuous support. I thank the unknown visa officer at the Canadian embassy who issued me that student visa so many years ago especially after the six refusals by the Embassy of the United States. All these things happened because I was destined to study optics. Thus, this thesis is a collection of personal stories.

CONTENTS

1 INTRODUCTION

> If Lorentz had allowed for a slight anharmonicity in his description of the electron as a harmonically-bound particle he could well have arrived at the theoretical derivation of a large variety of nonlinear optical effects. But Lorentz lacked the stimulation of stimulated emission of radiation.
>
> N. Bloembergen [1]

The study of light is essentially the study of how light interacts with materials. In our everyday experience—be it a double rainbow after the rain, caustics in the water waves rolling on a beach, or the characteristics of bifocal eyeglasses—light-matter interactions are governed by the rules of linear optics. The assumption of linear optics is that electrons are harmonically bound to an atom and in response to electromagnetic excitations, they wiggle about their equilibrium positions in harmonic potentials. However, in reality, the binding potentials are not strictly harmonic. When exposed to intense light the excursions of the electrons from their equilibrium positions become large and they feel the anharmonic nature of the potentials. The oscillations of electrons in anharmonic potentials in the presence of a strong electromagnetic radiation, such as from a laser beam, give rise to the nonlinear response of a material to light [2].

Light does not interact with light—it only interacts with materials. Thus, in order to control a light beam with another beam of light, one needs a nonlinear optical material as the mediating platform, i.e. a light beam changes the optical properties of the material and a second light beam feels that change. Nonlinear optics is the study of such interactions of strong light beams with materials. As a field of study nonlinear optics was

born with the discovery of the laser [3][1]. It has long been understood that the ability to induce on-demand, highly efficient and controlled interactions between two beams of light at a subpicosecond time scale may lead to a paradigm shift in technological advancement, specifically in signal processing and computation. However, the nonlinear responses of materials tend to be weak and is considered to be perturbative with respect to the linear response. The overarching theme of research in the 58 years of history of nonlinear optics has been the search for materials and operating conditions under which the efficiency of the nonlinear response can be improved. All advancement in this respect– despite being phenomenal in many ways – has largely been marginal due to the intrinsically weak nonlinear response of common materials specifically in terms of the ability to control properties of a light beam with another light beam.

1.1 THE CASE FOR ZERO PERMITTIVITY

The four Maxwell's equations along with the two constitutive relations form the theoretical basis of the study of electromagnetism. The four Maxwell's equations in phasor form for a harmonic field—for a linear and nonmagnetic material containing no free charges or free current—can be written as[4]

$$\nabla \times \mathbf{E} = i\omega \mathbf{B}, \tag{1a}$$
$$\nabla \times \mathbf{H} = i\omega \mathbf{D}, \tag{1b}$$
$$\nabla \cdot \mathbf{D} = 0, \tag{1c}$$
$$\nabla \cdot \mathbf{B} = 0. \tag{1d}$$

The two constitutive relations are:

$$\mathbf{D} = \epsilon_0 \epsilon_r \mathbf{E}, \tag{2a}$$
$$\mathbf{B} = \mu_0 \mathbf{H}. \tag{2b}$$

In general the relative permittivity (ϵ_r) of a material can be positive (dielectric) or negative (metal). However, the value of the relative permittivity ϵ can also be zero[2]. In a medium with a

1 A notable exception is the two-photon absorption predicted by Maria Goeppert-Mayer in 1931, almost 30 years prior to the invention of the laser.

2 For simplicity we henceforth drop the subscript "r" in ϵ_r to denote relative permittivity.

vanishing permittivity the magnetic field (**H**) becomes curl-free and the Helmholtz's wave equation becomes

$$\nabla^2 \mathbf{E} = 0. \tag{3}$$

Consequently, the propagation constant $k = 2\pi\sqrt{\epsilon}/\lambda$ becomes zero, i.e. the wave accumulates no phase as it propagates through the medium, the phase velocity ($v_p = c/\sqrt{\epsilon}$) diverges, and the wavelength is stretched ($\lambda = \lambda_0/\sqrt{\epsilon}$). Such a medium ($\epsilon \to 0$) is known as an epsilon-near-zero (ENZ) medium [5]–[10].

A whole host of exotic linear optical effects both in the classical and in the quantum domain can occur in an ENZ medium. For example, a wave always exits such a medium perpendicular to the interface as a consequence of the Snell-Descartes-Ibn Sahl law [5], [8], [9], [11]. As a result, emission from such a medium can be highly directive and the phase front can be arbitrarily shaped by shaping the exit facet of an ENZ material. The wavelength of light inside an ENZ medium can be many times larger than the free-space wavelength. Consequently, interactions between two emitters inside an ENZ medium are dominated by the near-field even if the distance between the emitters is physically large [12]. The density of state in a three dimensional isotropic and homogeneous medium can be effectively zero resulting in suppressed spontaneous emission [13].

1.2 BOOSTING NONLINEAR RESPONSE BY ZEROING LINEAR RESPONSE

An applied electric field causes the atoms or molecules to create electric dipole moments that augment the total displacement field **D**. The polarization vector **P** has both linear and nonlinear parts [2]. It is assumed that the nonlinear response is only perturbative to the linear response. Consequently, a power series expansion is performed to include the nonlinear response in the polarization vector as

$$\begin{aligned}\mathbf{P} &= \epsilon_0 \left[\chi^{(1)}\mathbf{E} + \chi^{(2)}\mathbf{E}\mathbf{E}^* + \chi^{(3)}\mathbf{E}\mathbf{E}^*\mathbf{E} + \dots\right] \\ &= \epsilon_0\chi^{(1)}\mathbf{E} + \mathbf{P}_{NL},\end{aligned} \tag{4}$$

where $\chi^{(n)}$ is the nth order susceptibility tensor of different rank and describes how a material responds to the applied electric

field; $\mathbf{P}_{NL}$ is the nonlinear polarization; and * denotes complex conjugate. We can express the displacement field as

$$\mathbf{D} = \epsilon_0(1+\chi^{(1)})\mathbf{E} + \mathbf{P}_{NL} = \epsilon_0\epsilon_r\mathbf{E} + \mathbf{P}_{NL} \tag{5}$$

Typically the linear term in the above equation is many orders of magnitude larger than the nonlinear term. However, in a material with a vanishingly small linear permittivity ($\epsilon \to 0$), the displacement vector $\mathbf{D}$ can become a strong function of the of the nonlinear polarization vector due to the absence of the otherwise dominant linear term, i.e. $\mathbf{D} = \mathbf{P}_{NL}$. As a consequence, the nonlinear wave equation in a medium with zero-permittivity can be expressed as

$$\nabla^2\mathbf{E} = -\frac{\omega^2}{\epsilon_0 c^2}\mathbf{P}_{NL}. \tag{6}$$

Thus in a medium with identically zero perimittivy, the wave propagation dynamics can be strongly affected by the nonlinear response of the medium compared to the case in a standard optical material such as glass.

1.3 MOTIVATION OF THE THESIS

There are many types of nonlinear optical effects, such as harmonic generation, frequency mixing, self-action effects, electro-optic effects, etc. Perhaps the conceptually simplest of all nonlinear optical effects is the intensity-dependence of the refractive index of a material. A strong laser beam can transiently alter the linear refractive index ($n_0 = \sqrt{\epsilon_r}$) of a material in a reversible fashion. This nonlinear effect is known as the intensity-dependent refractive index and is expressed as

$$n = n_0 + \Delta n = n_0 + n_2 I, \tag{7}$$

where I denotes the time-averaged intensity of the optical field and is proportional to $|\mathbf{E}|^2$, and Δn is the total nonlinear contribution to the refractive index. The intensity-dependent nonlinear index coefficient n_2 can be expressed as

$$n_2 = \frac{3\chi^{(3)}}{4\epsilon_0 n_0 \mathrm{Re}\{n_0\}}. \tag{8}$$

In general, irrespective of the value and the microscopic source of the intensity-dependence of the refractive index, the maximum total nonlinear contribution to the refractive index Δn is always limited either by the damage threshold or saturation mechanisms. Thus, even in the presence of a strong laser beam, Δn typically tend to be at least two-three orders of magnitude smaller than n_0.

In an ENZ medium, the near-zero value of the permittivity leads to a near-zero value of the refractive index. Thus, according to Eq. 8, for a given value of third-order susceptibility, the nonlinear refractive index coefficient apparently diverges in an ENZ material.

1.4 ORGANIZATION OF THE THESIS

This thesis is a collection of six manuscripts. In the first experiment, we demonstrate that it is possible to achieve an unprecedentedly strong nonlinear light-matter interaction in an ENZ material. Specifically, we show that it is possible to achieve unity-order nonlinear changes to the refractive index of such material under optical excitation.

In experiments described in the two following chapters, we show that the resonance properties of an optical antenna can be statically and dynamically modified due to the linear and nonlinear responses a thin ENZ substrate. Specifically, we show that a composite thin film (a metasurface) made of an array of optical antennas on a thin ENZ substrate can exhibit roughly a seven orders of magnitude increase in the nonlinear optical response as compared to that of glass. In this case, we exploit the local field enhancement introduced by an optical antenna array and the dynamic variations of their resonances due to changes in the refractive index of the ENZ substrate.

In the fourth chapter, we present an analysis of the nonperturbative nature of the nonlinear index. We answer the question of whether the perturbative expansion to describe the nonlinear response is valid for and ENZ medium.

In the next chapter, we draw an analogy between the well-known space refraction (Snell-Descartes-Ibn Sahl's law) and time refraction. When light passes from one medium to another separated by a temporal boundary, an analogue of Snell's law leads to a change in its wavelength. We experimentally demonstrate that, by exploiting the large nonlinear refraction of an ENZ ma-

terial excited by a strong pump beam, we can change the frequency of a weak probe beam by a value that is almost 70 times larger than previously reported values and using a material that is roughly 30-times shorter in physical length and many orders of magnitude smaller than the effective interaction length compared to previously reported nanophotonic platform.

Light carries both linear and angular momentum. In the final experiment, we show that as a consequence of highly stretched wavelength, the propagation of a light beam is highly nonparaxial in an ENZ material. As a result, the spin angular momentum of a Gaussian beam can be efficiently converted into orbital angular momentum as the beam passes through an ENZ medium. We found that an order of magnitude enhancement of such conversion in the presence of an ENZ thin film compared to standard optical materials such as fused silica.

The thesis concludes with a summary chapter that discusses the potential impact of this work and suggests directions for further investigations.

2 LARGE OPTICAL NONLINEARITY OF INDIUM TIN OXIDE IN ITS EPSILON-NEAR-ZERO REGION

CONTRIBUTION STATEMENT:

Professor Robert Boyd assigned this work to me as a summer project during the second year of my PhD. It ended up being a three-year-long project by the time the paper was published and is the foundational stone of this thesis. This was the first experiment I performed using what was at the time a newly purchased tunable femtosecond laser system. I built the setup and wrote LabVIEW codes for data collection; performed tests using thirteen different samples primarily because we were both confused and excited by the largeness of the nonlinear response; performed data analysis; developed the numerical model of simplified two-temperature dynamics (after working on another model for five months and failing), and wrote the first draft. Subsequently, the paper was revised many times with the help of my two co-authors.

REPORTS

NONLINEAR OPTICS

Large optical nonlinearity of indium tin oxide in its epsilon-near-zero region

M. Zahirul Alam,[1] Israel De Leon,[1,3]* Robert W. Boyd[1,2]

Nonlinear optical phenomena are crucial for a broad range of applications, such as microscopy, all-optical data processing, and quantum information. However, materials usually exhibit a weak optical nonlinearity even under intense coherent illumination. We report that indium tin oxide can acquire an ultrafast and large intensity-dependent refractive index in the region of the spectrum where the real part of its permittivity vanishes. We observe a change in the real part of the refractive index of 0.72 ± 0.025, corresponding to 170% of the linear refractive index. This change in refractive index is reversible with a recovery time of about 360 femtoseconds. Our results offer the possibility of designing material structures with large ultrafast nonlinearity for applications in nanophotonics.

A long-standing goal in nonlinear optics has been the development of materials whose refractive index can be drastically changed using a low-power optical field. Ideally, these materials should possess sub-picosecond time response and be compatible with existing complementary metal-oxide semiconductor (CMOS) fabrication technologies (*1*–*2*). Simple calculus shows that, for a given change ($\Delta\varepsilon$) in the permittivity ε, the resulting change (Δn) in the refractive index n is given for a lossless material by $\Delta n = \Delta\varepsilon/(2\sqrt{\varepsilon})$. We see that this change becomes large as the permittivity becomes small, suggesting that the epsilon-near-zero (ENZ) frequencies of a material system should give rise to strong nonlinear optical properties.

Materials possessing free charges, such as metals and highly doped semiconductors, have zero real permittivity at the bulk plasmon wavelength. A number of authors have reported on the unusual properties of matter under ENZ conditions (*3*–*5*) and on their promise for applications in nonlinear optics (*6*–*10*).

We used commercially available indium tin oxide (ITO), a CMOS-compatible degenerate semiconductor, as the ENZ medium (Fig. 1). The zero-permittivity wavelength of ITO occurs at near-infrared wavelengths and can be tuned by controlling the doping density or by applying a static electric field (*11*, *12*). The *z*-scan technique was used to characterize the intensity-dependent refractive index of ITO for transverse magnetic (TM) polarized light (Fig. 2A) (*13*, *14*). The wavelength-dependent effective nonlinear refractive index coefficient $n_{2(\mathrm{eff})} = \Delta n/I$ (I is the intensity of the laser beam) and effective nonlinear attenuation constant $\beta_{(\mathrm{eff})} = \Delta\alpha/I$ extracted from our measurements are plotted for angles of incidence varying from θ = 0° to θ = 60° (Fig. 2, A and B). The results indicate that ITO exhibits positive $n_{2(\mathrm{eff})}$ and negative $\beta_{(\mathrm{eff})}$, corresponding to self-focusing and saturable absorption, respectively. Our results reveal a substantial wavelength- and angle-dependent enhancement of the material's nonlinear response at ENZ wavelengths. The measured value of $n_{2(\mathrm{eff})}$ (6×10^{-5} cm^2/GW) at the shortest wavelength (970 nm) agrees well with the value reported by Elim *et al.* (*15*). At a wavelength of 1240 nm for normal incidence, $n_{2(\mathrm{eff})}$ and $\beta_{(\mathrm{eff})}$ are ~43 and ~53 times larger than the corresponding values at 970 nm, respectively. For TM-polarized light at oblique incident, the nonlinear response is further enhanced. The enhancement factors, defined relative to the values far from the ENZ spectral region (at λ = 970 nm) at normal incidence, are plotted as functions of θ in Fig. 2C. The enhancement tends to increase with θ for 0° < θ < 60° and decreases sharply for θ > 60°. The maximum enhancement factors, measured at θ = 60°, are 1837 and 2377 for $n_{2(\mathrm{eff})}$ and $\beta_{(\mathrm{eff})}$, respectively. Thus, at λ_0 = 1240 nm, the $n_{2(\mathrm{eff})}$ and $\beta_{(\mathrm{eff})}$ values for θ = 60° are ~43 and ~45 times larger than for normal incidence, respectively.

The temporal dynamics of the optical nonlinear response was studied using a degenerate pump-probe transmission measurement. Here, an intense pump pulse and a weak probe pulse at the same wavelength interact with the sample, and the induced change in probe transmittance ΔT is measured as a function to the time delay τ between the two pulses. The measured temporal response is proportional to the convolution of the probe's temporal envelope with the material's temporal response function. (Fig. 2D). The transient nonlinear response has a rise time no longer than 200 fs (this estimate is limited by our laser pulse duration) and a recovery time of 360 fs. Such ultrafast response would allow all-optical modulation speeds of at least 1.5 THz.

The nonlinear coefficients shown in Fig. 2, A and B, may be slightly overestimated because the *z*-scan method neglects the change in reflectivity caused by Δn (*16*), but this overestimation is no larger than by a factor of ~1.8. In any case, the measured values are extremely large. In particular, the value of $n_{2(\mathrm{eff})}$ = 0.11 cm^2/GW measured at θ = 60° is more than two orders of magnitude larger than that of As_2Se_3 chalcogenide glass (*17*) and ~5 times larger in magnitude than that of a recently proposed highly nonlinear metamaterial (*6*). The optical losses of ITO at ENZ wavelengths can be quite large, although in (*16*) we describe some realistic applications that can tolerate this much loss.

We attribute the observed nonlinearity primarily to a modification of the energy distribution of conduction-band electrons as a consequence of the laser-induced electron heating. We describe the nonlinear optical response by means of a phenomenological two-temperature model (*16*, *18*–*20*). Figure 3A shows the calculated temporal evolution of the free-electron temperature (T_e) and lattice temperature (T_l) of ITO after irradiation by the laser pulse (denoted by the dashed curve). The free-electron temperature exhibits an ultrafast transient and is limited by the electron-phonon relaxation time of the material (*21*). The normalized transient nonlinear response measured via the degenerate pump-probe technique is well described by the temporal profiles of T_e convolved with the probe's intensity envelope, which is plotted as the solid curve in Fig. 2D.

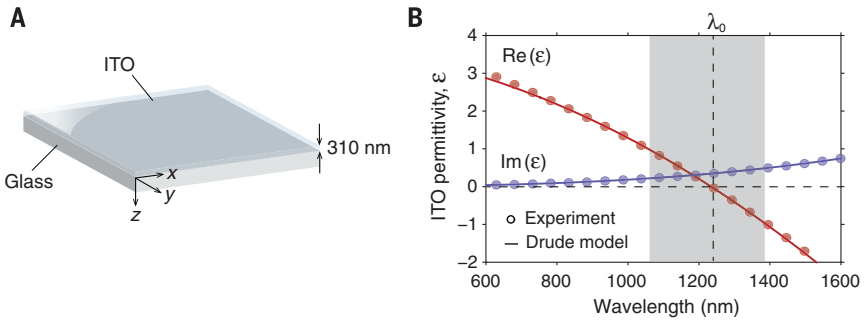

Fig. 1. The ITO sample under investigation and its linear optical response. (**A**) Structure under investigation. (**B**) Linear relative permittivity of the ITO film measured via spectroscopic ellipsometry (symbols) and estimated by the Drude model (lines). The condition Re(ε) = 0 occurs at λ_0 = 1240 nm. The shaded region shows the spectral range investigated in our nonlinear optical characterization.

[1]Department of Physics and Max Planck Centre for Extreme and Quantum Photonics, University of Ottawa, 25 Templeton Street, Ottawa, ON, K1N 6N5, Canada. [2]Institute of Optics and Department of Physics and Astronomy, University of Rochester, Rochester, NY 14627, USA. [3]School of Engineering and Sciences, Tecnológico de Monterrey, Monterrey, Nuevo León 64849, Mexico.
*Corresponding author. Email: ideleon@itesm.mx

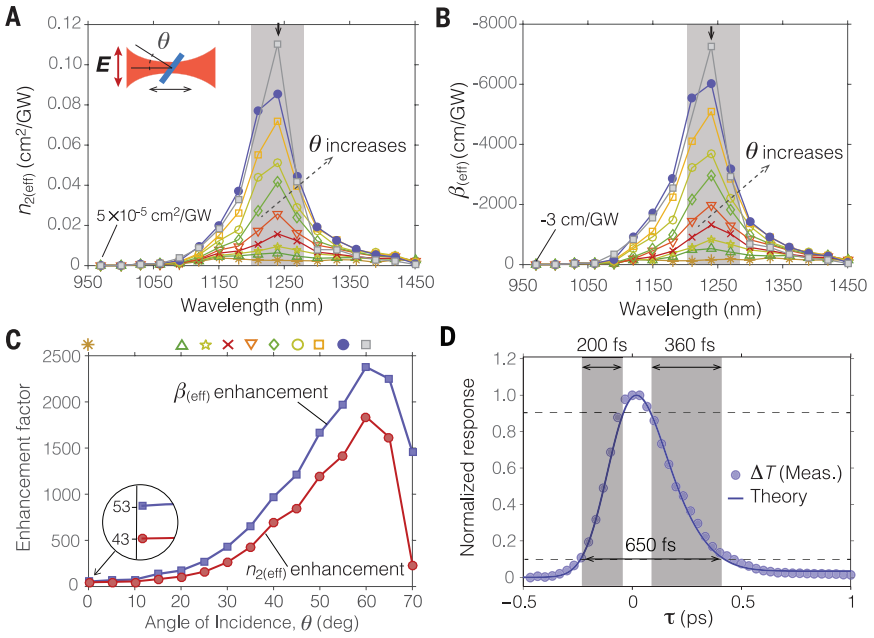

Fig. 2. Nonlinear optical response of the ITO sample. Wavelength dependence of (**A**) the nonlinear effective refractive index, $n_{2(eff)}$, and (**B**) the effective nonlinear attenuation constant, $\beta_{(eff)}$. The nonlinear response is enhanced in the ENZ region of the spectrum (shaded). The vertical arrows indicate the wavelength λ_0 = 1240 nm. (**C**) The corresponding enhancement for $n_{2(eff)}$ and $\beta_{(eff)}$ at λ_0, compared with values at 970 nm, are plotted as functions of θ. The values of θ corresponding to the different symbols in (A) and (B) are indicated at the top. (**D**) Time dependence of the normalized transient change of transmittance (ΔT) obtained via a degenerate pump-probe measurement.

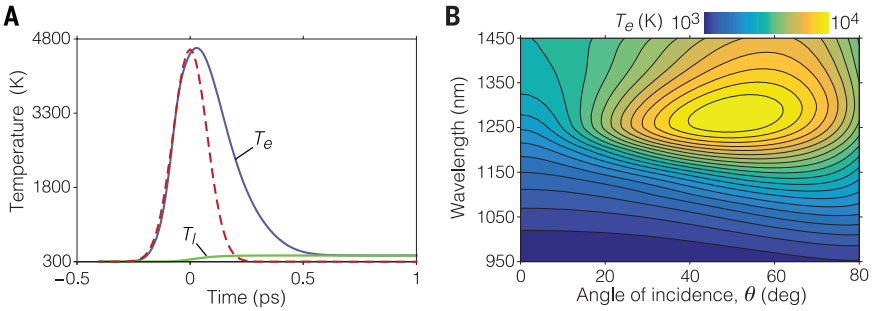

Fig. 3. Numerical modeling of the hot-electron dynamics of ITO. (**A**) Transient response of T_e and T_l obtained using the two-temperature model. The dashed curve denotes the pulse intensity profile (in arbitrary units). (**B**) Map of the peak free-electron temperature in ITO calculated as a function of θ and λ. Both calculations assume a normally incident laser with an intensity of 66 GW/cm^2.

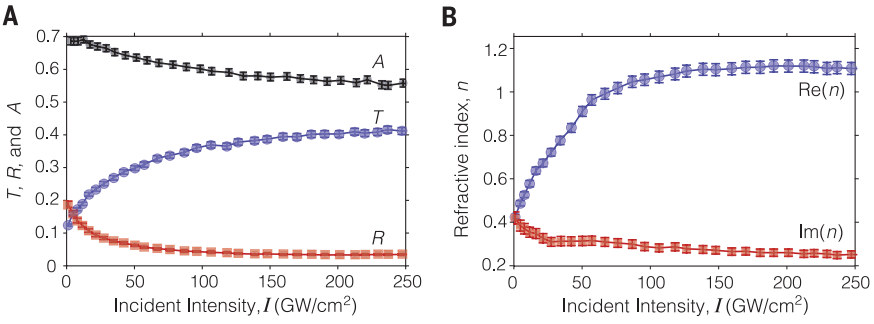

Fig. 4. Nonlinear optical response of ITO for laser fields sufficiently intense to produce saturation. (**A**) Intensity-dependent transmittance (T), reflectance (R), and absorptance (A) of the ITO-glass structure at λ_0 for θ = 30°. (**B**) Complex effective refractive index of ITO extracted from the measured values in (A) using a transfer-matrix method.

The peak values of T_e obtained with our model are plotted in Fig. 3B as functions of the wavelength and the angle of incidence. The temperature profile exhibits the main features present in our experimental results, namely a pronounced enhancement of the response at ENZ wavelengths that reaches a maximum for an angle of incidence close to θ = 60°. The general behavior observed in this result can be understood in terms of two contributions. The increasing values of T_e for longer wavelengths result from the increase in free carrier absorption, and the peak that develops around θ ≈ 60° results from an enhancement of the electric field within the ITO film. This enhancement occurs only for obliquely incident TM polarized light at wavelengths within the ENZ region and follows from the continuity of the normal electric displacement field across an ITO-air interface (*16*, *22*). As discussed in (*16*), Δε results from an effective red shift in the material's plasma frequency caused by an increase in the free-electron temperature (ΔT_e). It is important to note that Δε does not scale linearly with ΔT_e for a large ΔT_e and that Δn is a nonlinear function of Δε at ENZ. Consequently, a modest field intensity enhancement in the ITO film can lead to a large enhancement of $n_{2(eff)}$ at ENZ wavelengths. This is confirmed by our model presented in (*16*), which accounts for such nonlinear relationships between Δn, Δε, and ΔT_e.

The hot-electron–induced optical nonlinearity of ITO at ENZ wavelengths differs from that of noble metals under infrared irradiation in two ways. First, as argued above, for a given change in permittivity, the nonlinear change in refractive index is always larger in the ENZ region than in non-ENZ regions. Second, the free-electron heat capacity of ITO (4.53 Jm^{-3}K^{-1}) is more than an order of magnitude smaller than that of a noble metal such as gold. Thus, the increase in the free-electron temperature compared with the Fermi temperature and the consequent change in refractive index in ITO is much larger.

For sufficiently large optical intensities, the nonlinear response of ITO at ENZ wavelengths can lead to changes in its refractive index that are larger than the linear refractive index. As a result, the Fresnel reflection and transmission coefficients undergo a large change as a function of the incident optical intensity. To demonstrate this phenomenon, we measured the intensity-dependent transmittance (T), reflectance (R), and absorptance (A) of the sample at 1240 nm for θ = 30° (Fig. 4A). At the lowest intensity, these measurements agree well with the predictions of a simple linear Fresnel analysis. As the intensity is increased, we observe a large monotonic increase (reduction) in transmittance (reflectance). The maximum reduction in absorptance is ~30%, which is consistent with the saturable absorption observed in our z-scan measurements. The real part of the refractive index of ITO undergoes a dramatic change from its linear value of 0.42 to a value of 1.14 ± 0.025 for an intensity of 150 GW/cm^2 (Fig. 4B). Similarly, the imaginary part of the index is substantially reduced from

its linear value of 0.42 to a value of 0.27 ± 0.015 at this intensity. Both the real and the imaginary parts of the refractive index saturate for even higher input power. We found that these measurements are highly repeatable and that the material does not exhibit a permanent change of its optical properties.

The magnitude of the optically induced ultrafast change of the real part of the refractive index (Δn = 0.72 ± 0.025) and the relative change of 170% in comparison to the linear value are unprecedented. The change in the refractive index corresponds to a change of the permittivity from $\varepsilon = 0 + 0.352i$ to $\varepsilon = 1.22 + 0.61i$ where i is the square root of −1. This result shows that ITO can exhibit a reversible transition from metallic to a lossy dielectric state with a subpicosecond time response at wavelengths slightly longer than the bulk plasmon wavelength. Moreover, the usual perturbation expansion description of nonlinear optical effects is not applicable for this material at high intensities.

We have shown that a thin ITO film exhibits an extremely large ultrafast third-order nonlinearity at ENZ wavelengths. Moreover, it can acquire an optically induced change in the refractive index that is unprecedentedly large. Our results challenge the notion that the nonlinear optical response is only a perturbation to the linear response. Materials with such a large nonlinear response are expected to enable exotic nonlinear dynamics (*22*) and allow all-optical control of metasurface and active plasmonics devices. Thus, our results introduce a completely new paradigm in nonlinear optics and open new avenues for developing optical nanostructures with large nonlinearity for applications in nanophotonics, plasmonics, and nonlinear nano-optics.

REFERENCES AND NOTES

1. M. Kauranen, A. V. Zayats, *Nat. Photonics* **6**, 737–748 (2012).
2. M. Abb, P. Albella, J. Aizpurua, O. L. Muskens, *Nano Lett.* **11**, 2457–2463 (2011).
3. M. Silveirinha, N. Engheta, *Phys. Rev. Lett.* **97**, 157403 (2006).
4. A. Alù, M. Silveirinha, A. Salandrino, N. Engheta, *Phys. Rev. B* **75**, 155410 (2007).
5. A. R. Davoyan, A. M. Mahmoud, N. Engheta, *Opt. Express* **21**, 3279–3286 (2013).
6. A. D. Neira *et al.*, *Nat. Commun.* **6**, 7757 (2015).
7. H. Suchowski *et al.*, *Science* **342**, 1223–1226 (2013).
8. A. Capretti, Y. Wang, N. Engheta, L. Dal Negro, *Opt. Lett.* **40**, 1500–1503 (2015).
9. T. S. Luk *et al.*, *Appl. Phys. Lett.* **106**, 151103 (2015).
10. N. Kinsey *et al.*, *Optica* **2**, 616 (2015).
11. G. V. Naik, V. M. Shalaev, A. Boltasseva, *Adv. Mater.* **25**, 3264–3294 (2013).
12. E. Feigenbaum, K. Diest, H. A. Atwater, *Nano Lett.* **10**, 2111–2116 (2010).
13. M. Sheik-Bahae, A. A. Said, T.-H. Wei, D. J. Hagan, E. W. Van Stryland, *IEEE J. Quantum Electron.* **26**, 760–769 (1990).
14. B. K. Rhee, J. S. Byun, E. W. Van Stryland, *J. Opt. Soc. Am. B* **13**, 2720 (1996).
15. H. I. Elim, W. Ji, F. Zhu, *Appl. Phys. B* **82**, 439–442 (2006).
16. See supplementary materials on *Science* Online.
17. R. W. Boyd, *Nonlinear Optics* (Elsevier, 2008).
18. C. Sun, F. Vallée, L. Acioli, E. P. Ippen, J. G. Fujimoto, *Phys. Rev. B Condens. Matter* **48**, 12365–12368 (1993).
19. S. D. Brorson, J. G. Fujimoto, E. P. Ippen, *Phys. Rev. Lett.* **59**, 1962–1965 (1987).
20. E. Carpene, *Phys. Rev. B* **74**, 024301 (2006).
21. B. Rethfeld, A. Kaiser, M. Vicanek, G. Simon, *Phys. Rev. B* **65**, 214303 (2002).
22. D. de Ceglia, S. Campione, M. A. Vincenti, F. Capolino, M. Scalora, *Phys. Rev. B* **87**, 155140 (2013).

ACKNOWLEDGMENTS

The authors gratefully acknowledge the support of the Canada Excellence Research Chairs Program. R.W.B. is the cofounder and Chief Technology Officer of KBN Optics, Pittsford, NY.

SUPPLEMENTARY MATERIALS

www.sciencemag.org/content/352/6287/795/suppl/DC1
Materials and Methods
Supplementary Text
Figs. S1 to S4
References (*23*–*32*)

7 December 2015; accepted 12 April 2016
Published online 28 April 2016
10.1126/science.aae0330

CATALYSIS

Photochemical route for synthesizing atomically dispersed palladium catalysts

Pengxin Liu,[1] Yun Zhao,[1] Ruixuan Qin,[1] Shiguang Mo,[1] Guangxu Chen,[1] Lin Gu,[2] Daniel M. Chevrier,[3] Peng Zhang,[3] Qing Guo,[1] Dandan Zang,[1] Binghui Wu,[1] Gang Fu,[1]* Nanfeng Zheng[1]*

Atomically dispersed noble metal catalysts often exhibit high catalytic performances, but the metal loading density must be kept low (usually below 0.5%) to avoid the formation of metal nanoparticles through sintering. We report a photochemical strategy to fabricate a stable atomically dispersed palladium–titanium oxide catalyst (Pd_1/TiO_2) on ethylene glycolate (EG)–stabilized ultrathin TiO_2 nanosheets containing Pd up to 1.5%. The Pd_1/TiO_2 catalyst exhibited high catalytic activity in hydrogenation of C=C bonds, exceeding that of surface Pd atoms on commercial Pd catalysts by a factor of 9. No decay in the activity was observed for 20 cycles. More important, the Pd_1/TiO_2-EG system could activate H_2 in a heterolytic pathway, leading to a catalytic enhancement in hydrogenation of aldehydes by a factor of more than 55.

Atomically dispersed catalysts with mononuclear metal complexes or single metal atoms anchored on supports have recently attracted increasing research attention (*1*–*15*). With 100% metal dispersity, atomically dispersed catalysts offer the maximum atom efficiency, providing the most ideal strategy to create cost-effective catalysts, particularly those based on Earth-scarce metals such as Pt (*1*–*5*), Au (*5*–*8*), Pd (*9*–*12*), and Ir (*13*, *14*). Moreover, the uniform active sites of atomically dispersed catalysts make them a model system to understand heterogeneous catalysis at the molecular level (*4*, *6*, *10*, *12*–*14*, *16*–*21*), bridging the gap between heterogeneous and homogeneous catalysis.

During the past decade, several strategies for atomically dispersing metal sites on catalyst supports have emerged; these include lowering the loading amount of metal components (*1*, *8*–*10*, *12*, *20*), enhancing the metal-support interactions (*4*, *6*, *9*, *19*), and using voids in supports or vacancy defects on supports (*3*, *11*, *14*, *22*). In most cases, the supports for atomically dispersed catalysts are deliberately chosen. Zeolites provide effective voids to anchor individual metal atoms therein and prevent them from sintering during catalysis (*23*, *24*). Defects on reducible oxides (e.g., TiO_2 and CeO_2) (*25*, *26*) and on graphene or C_3N_4 (*9*, *11*, *22*) help to stabilize atomically dispersed metal atoms on supports. Coordinatively unsaturated Al^{3+} ions on γ-Al_2O_3 act as binding centers to maintain the high dispersion of Pt atoms, but Pt rafts form as the loading amount of Pt increases (*3*). Currently, two major challenges remain in the field of atomically dispersed catalysts: (i) to ensure a loading content high enough for practical applications while maintaining the metal centers as individual sites under catalytic conditions (*27*, *28*), and (ii) to address whether atomically dispersed catalysts offer distinct active sites and/or undergo catalytic pathways different from those of conventional metal catalysts (*1*, *4*–*6*, *8*–*10*, *12*, *16*–*21*).

We report a room-temperature photochemical strategy to fabricate a highly stable, atomically dispersed Pd catalyst (Pd_1/TiO_2) on ultrathin TiO_2 nanosheets with Pd loading up to 1.5%.

[1]State Key Laboratory for Physical Chemistry of Solid Surfaces, Collaborative Innovation Center of Chemistry for Energy Materials, Engineering Research Center for Nano-Preparation Technology of Fujian Province, National Engineering Laboratory for Green Chemical Productions of Alcohols, Ethers, and Esters, and Department of Chemistry, College of Chemistry and Chemical Engineering, Xiamen University, Xiamen 361005, China. [2]Institute of Physics, Chinese Academy of Sciences, Beijing 100190, China. [3]Department of Chemistry, Dalhousie University, Halifax, Nova Scotia B3H 4R2, Canada.
*Corresponding author. Email: nfzheng@xmu.edu.cn (N.Z.);

Science

Large optical nonlinearity of indium tin oxide in its epsilon-near-zero region

M. Zahirul Alam, Israel De Leon and Robert W. Boyd

Science **352** (6287), 795-797.
DOI: 10.1126/science.aae0330originally published online April 28, 2016

Nonlinear optics: A surprise in store?

At ultrafast data rates, the ability to use light to control things could speed information processing. However, photons tend not to interact with each other, and so a nonlinear optical material is needed and the response of such materials is typically weak. Alam *et al.* report a surprising finding: that indium tin oxide, a commercially available transparent conducting oxide widely used in microelectronics, exhibits a large nonlinear response. They used a wavelength regime where the permittivity of the material is close to zero and observed a large and fast nonlinear optical response. The finding offers the possibility that other, so far unexplored, materials may be out there for nonlinear optical applications.

Science, this issue p. 795

www.sciencemag.org/cgi/content/full/science.aae0330 /DC1

Supplementary Materials for

Large optical nonlinearity of indium tin oxide in its epsilon-near-zero region

M. Zahirul Alam, Israel De Leon,* Robert W. Boyd

*Corresponding author. Email: ideleon@itesm.mx

Published 28 April 2016 on *Science* First Release
DOI: 10.1126/science.aae0330

This PDF file includes:

Materials and Methods

Linear response of ITO

Our sample is a commercially available ITO film with sheet resistance of $\sim 5\ \Omega/$ square, deposited on a float glass substrate. The thickness of the film is 310±2 nm, and that of the substrate is 1.1 mm (Fig. 1A). The linear relative permittivity of the ITO film, ε, was measured via spectroscopic ellipsometry (Fig. 1B). Note that due to the large doping concentration, the optical properties of ITO at near-infrared wavelengths resemble those of a free electron gas. This is apparent from the excellent agreement between the experimental data (symbols) and the Drude model (solid curves), $\varepsilon = \varepsilon_\infty - \omega_p^2/(\omega^2 + i\gamma\omega)$ using a high-frequency permittivity of ε_∞= 3.8055, a damping rate of γ = 0.0468ω_p, and a free-electron plasma frequency of $\omega_p/2\pi$ = 473 THz. The zero-permittivity condition, Re(ε)=0, occurs at the bulk plasmon wavelength $\lambda_0 = 2\pi c\sqrt{\varepsilon_\infty}/\omega_p$ = 1240 nm. At this wavelength the permittivity also has a large imaginary part, Im(ε) ≈ 0.35, associated with damping losses in the material.

Z-scan procedure

The z-scan technique (*14*) was used to study the intensity-dependent refractive index of the ITO film. In this technique, the sample is exposed to different optical intensities by translating it along the optical axis of the focused laser beam, and changes in the optical phase and attenuation of the transmitted light are measured as functions of the optical intensity. The measurements are taken over a broad spectral range covering the low permittivity region of the material and with a broad range of angles of incidence. The recorded data is then used to extract the effective nonlinear refractive index, $n_{2(\text{eff})}$, and the effective nonlinear attenuation constant, $\beta_{(\text{eff})}$. These parameters are defined as $n_{2(\text{eff})} = \Delta n/I$ and $\beta_{(\text{eff})} = \Delta\alpha/I$, where Δn and $\Delta\alpha$ are, respectively, the change in refractive index and the change in attenuation constant induced by the laser beam, and I is the intensity of the beam at its focus. For all our z-scan measurements, we used a pulsed laser (150 fs pulse duration, repetition rate of 1 kHz) with average incident power of 60 μW across the spectrum. This average power corresponds to a peak intensity of 66 GW/cm^2 at the beam's focus at a wavelength of 1240 nm.

We used a pinhole of 0.3 mm diameter to produce a beam with circularly symmetric trimmed Airy profile in the far-field. A series of lenses was then used to collimate and enlarge the beam. Part of the collimated beam was routed to a reference photodiode to monitor power fluctuations. The rest of the collimated beam was then focused onto the sample using an achromatic doublet lens with anti-reflection coating. The focused spot size was 25μm. The diffracted light after the sample was split using a pellicle beam splitter and routed to a pair of detectors for closed and open aperture measurements. The sample was mounted on a computer-controlled motorized translation stage. For each position of the sample we record the truncated mean values (the lowest 25% and the highest 25% values were discarded before calculating the mean) from the photodiodes averaged over roughly 3000 pulses. The signals from both closed- and open-aperture photodiodes were normalized by the signal obtained from the reference photodiodes to minimize the noise induced by the fluctuation of the laser beam intensity.

We used the Fresnel-Kirchhoff diffraction integral using a fast-Fourier-transform-based beam propagation method to simulate the experimental beam propagation over the entire setup, and the z-dependence of the signal at the closed-aperture and open aperture photodiodes (*23*). We have not made any *a priori* assumptions about the magnitude of the nonlinear phase shift. It is critical to our experiment that we not make such an assumption because the total nonlinear phase shift was quite large, which may invalidate the standard closed-form expressions for the far-field z-scan signals (*14*). We performed numerical simulations of the nonlinear setup to determine the z-dependence of the open- and closed-aperture signals. We verified our calculations by reproducing the results of other authors for both small and large phase shifts (*14*, *24*). The shape of the closed-aperture signal is dependent on the shape of the open-aperture. Hence it is necessary to first extract the imaginary part of the phase shift. In order to extract the value of the phase shifts (real and imaginary) we followed the following steps. First, we generated a wavelength and angle dependent grid containing nonlinear imaginary phase shifts (step size of 0.0002 rad) and the maximum normalized net increase in transmittance at the open aperture photodiode. Then, for each value of the imaginary phase shift we produced corresponding wavelength and angle dependent grid containing nonlinear real phase shifts (step size of 0.0002 rad) and the transmission separation between the peak and the valley. We used the first grid to find the imaginary part of the phase shift from the open aperture data and the later grid to find the acquired real part of the phase shift. The extracted values of the nonlinear phase were used in the standard expression to calculate $n_{2(\mathrm{eff})}$ and $\beta_{(\mathrm{eff})}$ (*17*). Fig. S1 shows representative close- and open-aperture measurements at λ = 1240 nm.

Extraction of refractive index from transmittance and reflectance measurements

We estimated the effective complex refractive index of the ITO film associated with each set of transmittance and reflectance measurements for a given incident intensity. We use a nonlinear constrained optimization technique to find the simultaneous minima of the reflectance and the transmittance functions obtained using a linear transfer-matrix method. In our calculations we assumed that the refractive index of the substrate is independent of the intensity and took the substrate (glass) as an incoherent layer. This assumption is justified because the nonlinear optical response of the substrate is orders of magnitude weaker than that of the ITO film. We solve the minimization problem using the Nelder-Mead method. For each iteration of simultaneous minima finding operation we used the linear complex refractive index as the initial guess.

Pump-probe response

We measured the transmittance of a weak probe as a function of the delay between the probe and a strong pump of the same wavelength. The transient change in the optical properties of ITO is proportional to the transient change in the temperature of the electrons. Hence, the transmittance of the probe for a particular pump-probe delay is proportional to the convolution of the temporal response of the hot electrons with the probe pulse. In a typical pump-probe measurement, it is often necessary to use lock-in detection techniques. However, in our experiment the change in transmittance of the probe is so strong that we did not require any such sensitivity-enhancement techniques. We have observed that the overall response time has a minor frequency dependence: the system relaxes more quickly when pumped with a shorter wavelength. This variation is

due simply to the fact that higher photon energy leads to faster relaxation of electron to the Fermi level because $\tau_{ee} \propto (h\nu)^{-1}$.

Supplementary Text

Two-temperature model

The free-electron dynamics in ITO are metal-like and can be described by the Drude model. Hence, we assume that the third-order self-action nonlinear response of ITO in the ENZ regime is dominated by the response of the free-electrons. To describe this nonlinear mechanism, we use a phenomenological two-temperature model (*18*). This model has been successfully applied by many authors to explain the ultrafast nonlinear response of metals irradiated by femtosecond pulses (*18*, *20*, *21*, *25*). According to the two-temperature model, the laser energy absorbed by the material is transferred to non-thermalized electrons (known as "hot electrons") by promoting some free-electrons lying below the Fermi level to the unoccupied levels above the Fermi level.

The self-action nonlinear process due to the hot-electron dynamics has a finite response time, i.e. the maximum response is delayed with respect to the peak of the laser excitation. In noble metals the total relaxation time of the hot electrons is a few picoseconds and is limited by the electron-phonon interaction time. However the response of the ITO thin film deviates from that of the metal in three important ways: *i*) unlike noble metals, ITO has no interband transition resonance in the visible or infrared range of the optical spectrum; *ii*) the free-electron density in ITO is two orders of magnitude smaller than that of noble metals such as gold, resulting in much smaller electron heat capacity and larger change in the electron temperature if all other parameters are held constant; and *iii*) owing to a relatively smaller free-electron density, the Fermi level is quite low in the conduction band (~1 eV for ITO). Due to the last property, infrared radiation at ENZ wavelengths can excite even the lowest-energy conduction band electrons (in contrast, the Fermi level of gold is ~6.42 eV and IR light only excite only those electrons that sits near the Fermi level).

According to the delayed two-temperature model, after the laser pulse is absorbed the generated hot electrons acquire a non-thermal energy distribution and act as a delayed source of heating. The overall dynamics of the conduction band electrons can be described by the following system of phenomenological coupled differential equations (*25*) :

$$C_e \frac{\partial T_e}{\partial t} = -g_{ep}(T_e - T_l) + \frac{N}{2\tau_{ee}}, \#(S1A)$$

$$C_l \frac{\partial T_l}{\partial t} = g_{ep}(T_e - T_l) + \frac{N}{2\tau_{ep}}, \#(S1B)\#$$

$$\frac{\partial N}{\partial t} = -\frac{N}{2\tau_{ee}} - \frac{N}{2\tau_{ep}} + P, \#(S1C)$$

Here, N is the non-thermal energy density stored in the excited electrons, g_{ep} is the electron-phonon coupling coefficient, T_e (T_l) is the free-electron (lattice) temperature, C_e (C_l) is the heat capacity of the electrons (lattice), τ_{ee} (τ_{ep}) is the electron-electron (electron-phonon) relaxation time, and P is the time dependent absorbed power density (i.e., rate of energy density absorbed in the material). We have ignored thermal diffusion

processes in Eq. (S1). In the transverse dimension the beam size greatly exceeds the electrons thermal diffusion length and hence we also ignore the transverse dependence. We have also ignored the thermal diffusion in the longitudinal direction by assuming constant absorbed energy density.

In general, the thermal diffusivity of the electrons is a function of the electron temperature and the velocity. Since the hot electrons in a noble metal move approximately at the Fermi velocity, the heat transport is ballistic within the momentum relaxation length due to electron-electron interaction. Heat is transported much faster by the electrons than through the lattice, and hence typically the lattice contribution to the thermal diffusion can be ignored (*19*). We also ignored the heat diffusion by hot electrons in transverse dimension. The heat diffusion length is much shorter than the spot size and hence it can be safely ignored.

Next we estimate the different parameters for ITO that appear in Eqs. (S1). The electron-phonon coupling coefficient (g_{ep}) determines the strength of the energy exchange between the excited electrons and the vibrational modes of the lattice. We estimate this parameter as

$$g_{ep} = 0.562 n_e \frac{k_B^2 \Theta_D^2 v_F}{L_f T_l E_F}, \#(S2)$$

where k_B is Boltzmann's constant, L_f is the electron mean free path, v_F and E_F are the Fermi velocity and the Fermi energy respectively, Θ_D is the Debye temperature, and n_e is the free-electron density.

The electron-electron (τ_{ee}) and electron-phonon (τ_{ep}) relaxation times in Eqs. (S1) dictate the rate at which the absorbed energy is redistributed to the electrons and to the lattice respectively. These quantities are given by (*26*, *27*)

$$\tau_{ee} = C \left\{ \frac{\omega^2}{4\pi^2 \omega_p} \left[1 + \left(\frac{2\pi k_B T_e}{\hbar \omega} \right)^2 \right] \right\}^{-1}, \#(S3A)$$

$$\tau_{ep} = 2 \frac{C_e}{g_{ep}}, \#(S3B)$$

where ω_p is the free-electron plasma frequency and ω is the frequency of the laser beam. Here, we use the parameter C in Eq. (S3A) as a scaling factor to make sure that the Drude damping parameter, γ, measured under thermal equilibrium (at a temperature of 300 K) is equal to $1/\tau_{ep} + 1/\tau_{ee}$.

The free-electron heat capacity (C_e) is a function of temperature. For temperatures smaller than the Fermi temperature, this quantity can be approximated as $C_e = 3\pi^2 n_e k_B T_e / \sqrt{36 T_F^2 + 4\pi^4 T_e^2}$. On the other hand, the lattice heat capacity (C_l) depends on Θ_D. The value of Θ_D for ITO nanostructures is reported (*28*) to be ~ 1000 K, which is much larger than that of noble metals such as gold (~ 170 K). The Debye temperature Θ_D is defined as the temperature required for the excitation of the highest-frequency phonon mode - and thus, for the excitation all phonon modes. Hence, for lattice temperatures much lower than Θ_D, the number of the interacting phonon modes and, by extension, the lattice heat capacity (C_l) is a strong function of the lattice temperature. However, the lattice heat capacity asymptotically approaches a constant value as the lattice temperature approaches Θ_D. Therefore, even for $T_l \approx \Theta_D/2$, the temperature dependent variation is

small. Hence, we ignore this variation and find that a constant lattice heat capacity of 2.6×10^6 $Jm^{-3}K^{-1}$ (which is slightly larger than the heat capacity of In_2O_3) can reproduce our experimental results.

Finally, the absorbed power density (P) is given by

$$P(t) = (1 - R - T)I_0\alpha\, exp\left[-2\left(\frac{t}{\tau_p}\right)^2\right], \#(S4)$$

where R, T and α are the wavelength dependent reflectance, transmittance and absorption coefficient, respectively, and $\tau_p$is the laser pulse duration. In general, $P(t)$ is also spatially varying because of absorption within the ITO sample. However, we ignore this variation by assuming an effective intensity, I_0, that is constant over one absorption length.

Field enhancement at oblique incidence

According to Maxwell's equations, the longitudinal component of the displacement field must be continuous across an interface. Thus, the longitudinal component of the electric field inside ITO is inversely proportional to the permittivity of ITO. For instance, for the case of a single ITO-air interface, this continuity condition yields the following relation for the field components normal to the interface: $E_{\perp,\mathrm{ITO}} = E_{\perp,\mathrm{air}}/\varepsilon_{\mathrm{ITO}}$. Thus, for obliquely incident TM polarized light, the field inside the ITO is enhanced when $\varepsilon_{\mathrm{ITO}}$ is small. This enhancement, however, is limited by the non-vanishing imaginary part of the dielectric constant. We calculated the field enhancement factor as a function of wavelength and angle of incidence for TM polarized light using a transfer-matrix method and the measured linear permittivity values of our ITO sample. We show the result in Fig. S2.

Hot-electron-induced change of refractive index

A change in the electron temperature produces a change in complex refractive index of the material. The electron dynamics under non-equilibrium conditions and the associated change in the refractive index are complex many-body problems that require detailed knowledge of the electronic band structure. Since we lack this knowledge, it is difficult to model the non-equilibrium electronic dynamics from an *ab inito* approach. Therefore, we use a phenomenological approach based on the two-temperature model and the Drude model to describe the hot-electron induced change in refractive index.

The two-temperature model predicts a transient but large change in the electronic temperature, which results in a significant modification of the Fermi-Dirac distribution and a corresponding decrease in the free electron polarizability (*29*). Within the framework of the Drude model, this decrease in the polarizability is equivalent to a red-shift of the plasma frequency due to the temperature dependence of the Fermi level (17). This view is consistent with that of other authors who have investigated the nonlinear transient response of metal-ITO hybrid structures (*2*). Because of the complex physical mechanism relating the change in refractive index, Δn, to the change in free-electron temperature, ΔT_e, the relationship between these two quantities is not linear. This conclusion is also supported by the relationship between T_e and the electron-electron scattering rate (τ_{ee}^{-1}). At ENZ frequencies the photon energy ($h\nu$) is approximately equal to the Fermi energy (ε_F) of the conduction band electrons, and thus τ_{ee}^{-1}, the dominant dephasing mechanism, is a quadratic function of the electronic temperature ($\tau_{ee}^{-1} \propto T_e^2$)

(*26*, *30*, *31*). A change in the scattering rate results in the modification of the damping term in the Drude model. Since the change in the real and imaginary parts of the permittivity is related by the Kramers-Kronig relation, the relationship between ΔT_e and Δn is nonlinear.

The electron-electron scattering process distributes the absorbed energy among the electrons, and a short time after the passing of the pulse produces a hot Fermi distribution with electron temperature T_e (assuming that the total internal energy is constant). At this stage, electrons are in equilibrium with each other; however, they are not in equilibrium with the lattice. For a given electron density, the chemical potential (Fermi level) of a metal-like material depends on the temperature of the free electrons. Thus a change in the electron temperature produces a change of the chemical potential. Finally, the hot-electrons comes to the thermal equilibrium with the lattice through electron-phonon interaction. This results in an increase in the lattice temperature. The lattice energy is dissipated to the environment at a much longer time scale. However, low repetition rate of the laser ensures that the lattice is always at the thermal equilibrium with the laboratory before the arrival of an optical pulse.

The electronic temperature-dependent chemical potential (or Fermi level), $\mu(T_e)$, is related to the Fermi energy by (*32*)

$$\mu(T_e) \approx \varepsilon_F \left[1 - \frac{\pi^2}{12}\left(\frac{T_e}{T_F}\right)^2\right], \#(S5)$$

where T_F is the Fermi temperature. This relation allows one to estimate the effective plasma frequency at the elevated electronic temperature (for $T_e \ll T_F$,) and then use the Drude-Sommerfeld model of metals to calculate the change in the refractive index, Δn.

Using this method to calculate Δn, we obtained the enhancement of $n_{2(\text{eff})} = \Delta n/I$ as a function of the wavelength and the angle of incidence. This enhancement, shown in Fig. S3, is defined with respect to the value obtained at normal incidence at a wavelength $\lambda = 970$ nm. Note that for this calculation we have taken into account the wavelength and angle dependent field enhancement factor shown in Fig. S2. Our calculation is correct within the first order approximation, and shows that a modest field enhancement can result in significant enhancement of $n_{2(\text{eff})}$.

Effect of the non-linear change of reflectivity

In their seminal paper proposing the z-scan technique, Sheik-Bahae *et al.* (13) ignored the change in the Fresnel reflectivity due to the nonlinear optical effects. This approximation neglects any change in the internal optical intensity that may result from an optically induced increase or reduction of the Fresnel reflection. This approximation is excellent for most materials, including those exhibiting large nonlinear refractive index coefficients, because the nonlinear change in the refractive index, Δn, is typically much smaller than the linear refractive index, n. However, this is not the case for the experimental situation that we present in the main text, where Δn is similar to or even larger than n. As a concrete example, consider the results in Fig. 3a of the main text, where we show that the reflectance at $\theta = 30^\circ$ can change from a value of $R_L = 0.187$ for the linear case, to a value of $R_{NL} = 0.032$ for the most extreme nonlinear case – i.e., when the nonlinear response saturates. For the z-scan analysis in the main text, we always estimated the intensity within the sample by accounting for the Fresnel reflection using the value of the linear reflectance, i.e., $I = I_0(1-R_L)$, where I_0 is the intensity of the beam

at its focus and I is the intensity within the sample. However, as we explain next, this approximation leads to inaccuracies when extracting the values of $n_{2(\text{eff})}$ and $\beta_{(\text{eff})}$.

The maximum changes in the input laser intensities in the z-scan measurements are related to the maximum changes in the Fresnel reflectivities due to the nonlinear response of ITO. Since $T + A = 1 - R$, a nonlinear change in reflectance (R) necessarily implies changes in nonlinear absorptance (A) and trasmittance (T) due to the increase in input intensities. Thus, a nonlinear change in reflectance affects both open and closed-aperture measurements. However, we ignore the effect of the nonlinear Fresnel reflectivity in our calculation. Hence, there are uncertainties in the extracted values of $n_{2(\text{eff})}$ and $\beta_{(\text{eff})}$. The saturated values of the reflectance determine the maximum possible nonlinear changes in the input intensities. We estimate the upper bound to fractional error in the extracted nonlinear coefficients as

$$\zeta_{(\max)} = 1 - \frac{1-R_L}{1-R_{\text{NL(sat)}}}, \#(S6)$$

where $R_{\text{NL(sat)}}$ is the reflectance of the sample in the high intensity limit in which the change in refractive index reaches its maximum (saturated) value. The subscript L indicates linear value. For the particular case discussed above (θ = 30°), this maximum error is 19%. However, this error is not constant for all θ because the reflectance varies with θ. To estimate the maximum error for all the angles of incidence used in our experiments, we calculated $R_{\text{NL(sat)}}$ as a function of θ taking the saturated refractive index value of the ITO film, i.e., $n_{(\text{sat})} = 1.13 + i0.27$. This is a safe assumption, since we expect the saturated value of Δn to be the same regardless of the incident angle. We use this value in Eq. (S6) to obtain the maximum error expected in the extracted values of the nonlinear coefficients, which occurs when the input intensity is large enough to saturate the nonlinear optical response of the material. These calculated maximum errors are shown in Fig. S4.

Practical uses of the optical nonlinearity of ITO

ITO is a lossy material at ENZ frequencies. The losses in this material are significantly larger than those in other highly nonlinear materials, such as chalcogenide glass. For instance, the linear absorption coefficient of our ITO sample is roughly 4.2 μm^{-1} at $\lambda = 1240$ nm. Given the nature of its optical nonlinearity, ITO is probably not suitable to construct nonlinear devices requiring long propagations lengths. Rather, the large refractive index change accessible with ITO could be used in conjunction with nanoplasmonics and nanophotonics (where propagation lengths are very short) to create efficient nanoscopic nonlinear devices. For instance, the large change of refractive index of ITO can be extremely useful when combined with plasmonic nanostructures, whose optical properties are extremely sensitive to the refractive index around them. Moreover, the ultrafast recovery time and large change in absorption may allow one to use a thin film of ITO at ENZ wavelengths as a saturable absorber in a mode-locked laser.

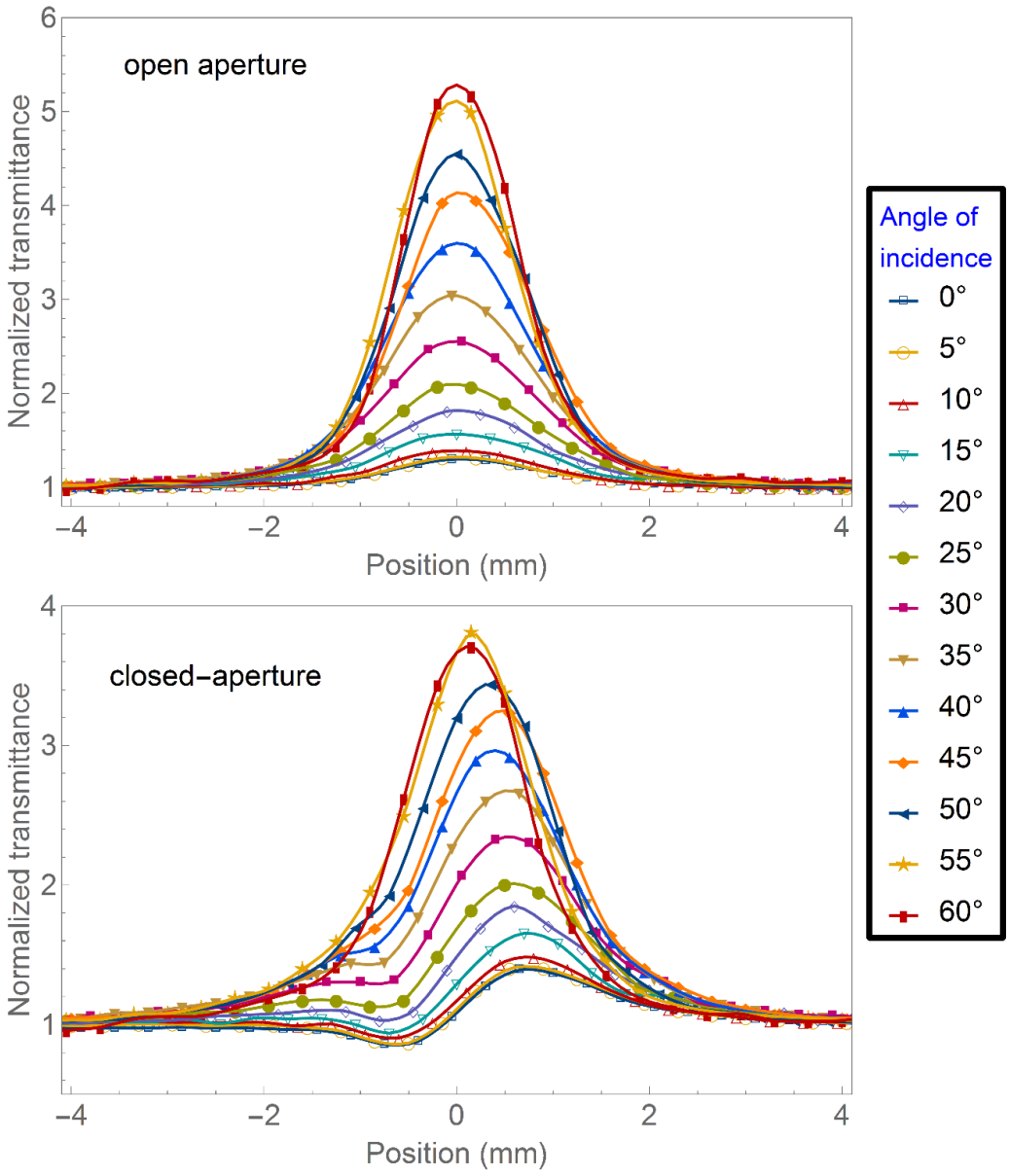

Fig. S1.

Open- and closed-aperture measurements at λ = 1240 nm for various angles of incidence. The asymmetry in the closed-aperture signal increases with increasing angle of incidence due to the large change in the absorption.

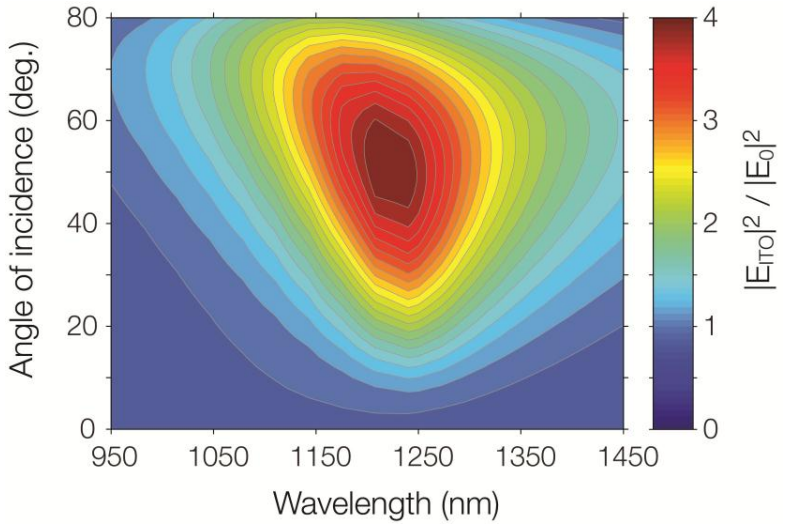

Fig. S2

Field enhancement at the air-ITO interface for obliquely incident TM polarized light. The maximum field enhancement factor is 4, and occurs at wavelengths around λ_0 = 1240 nm.

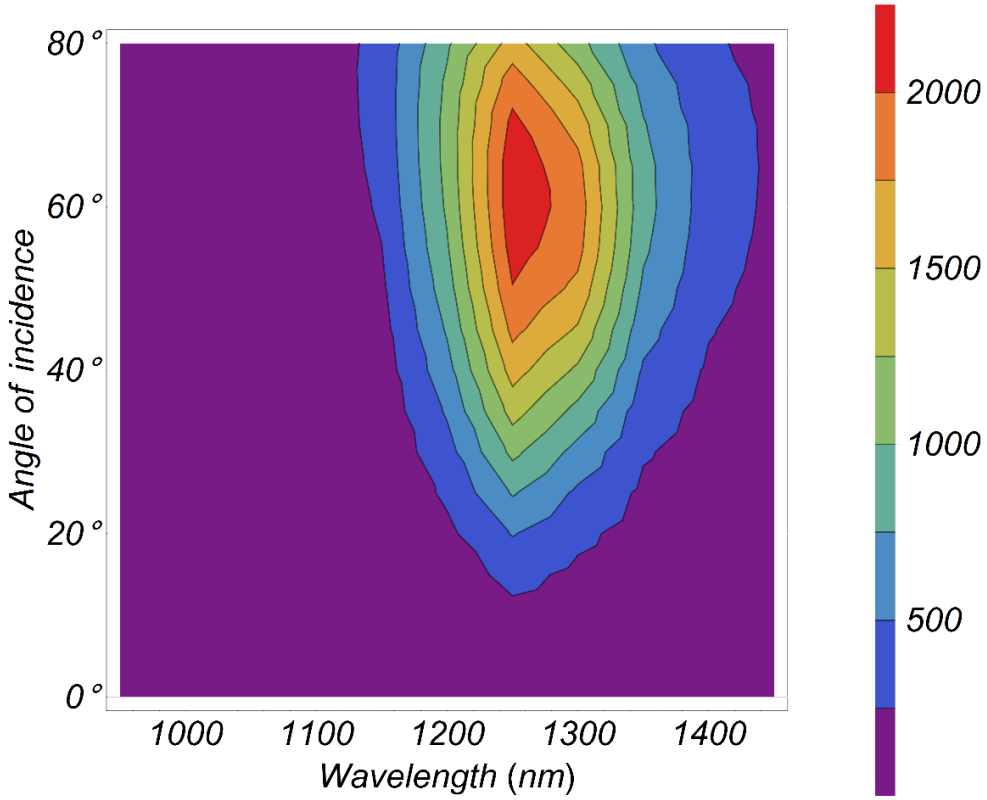

Fig. S3.

Enhancement of $n_{2(\text{eff})}$ calculated using a first-order approximation to the electronic temperature-dependent red-shift of the plasma frequency. We used the $n_{2(\text{eff})}$ value at λ = 970 nm as the normalization factor. For this calculation we have used an incident intensity of 20 GW/cm^2.

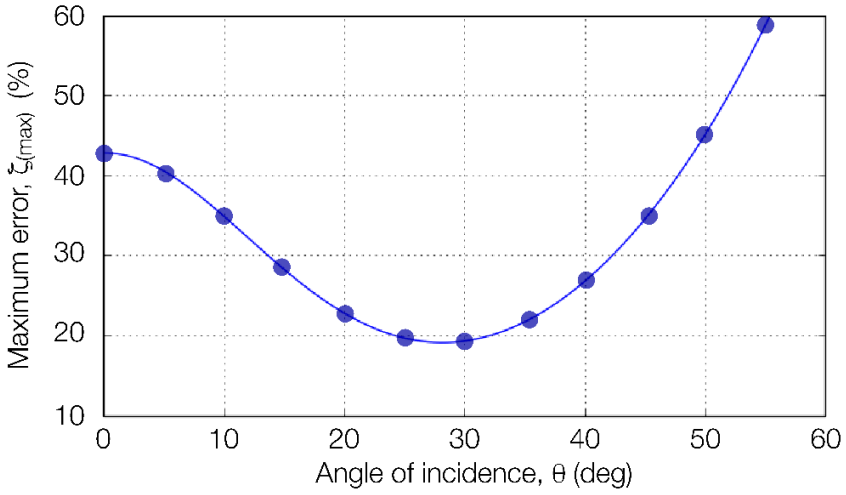

Fig. S4.

Maximum error in the extracted nonlinear coefficients when the input intensity is large enough to saturate the nonlinear optical response of the material. The values plotted here were calculated using Eq.(S6).

References

1. M. Kauranen, A. V. Zayats, Nonlinear plasmonics. *Nat. Photonics* **6**, 737–748 (2012). doi:10.1038/nphoton.2012.244

2. M. Abb, P. Albella, J. Aizpurua, O. L. Muskens, All-optical control of a single plasmonic nanoantenna-ITO hybrid. *Nano Lett.* **11**, 2457–2463 (2011). Medline doi:10.1021/nl200901w

3. A. D. Neira, N. Olivier, M. E. Nasir, W. Dickson, G. A. Wurtz, A. V. Zayats, Eliminating material constraints for nonlinearity with plasmonic metamaterials. *Nat. Commun.* **6**, 7757 (2015). Medline doi:10.1038/ncomms8757

4. M. Silveirinha, N. Engheta, Tunneling of electromagnetic energy through subwavelength channels and bends using ε-near-zero materials. *Phys. Rev. Lett.* **97**, 157403 (2006). Medline doi:10.1103/PhysRevLett.97.157403

5. A. Alù, M. Silveirinha, A. Salandrino, N. Engheta, Epsilon-near-zero metamaterials and electromagnetic sources: Tailoring the radiation phase pattern. *Phys. Rev. B* **75**, 155410 (2007). doi:10.1103/PhysRevB.75.155410

6. A. R. Davoyan, A. M. Mahmoud, N. Engheta, Optical isolation with epsilon-near-zero metamaterials. *Opt. Express* **21**, 3279–3286 (2013). Medline doi:10.1364/OE.21.003279

7. H. Suchowski, K. O'Brien, Z. J. Wong, A. Salandrino, X. Yin, X. Zhang, Phase mismatch-free nonlinear propagation in optical zero-index materials. *Science* **342**, 1223–1226 (2013). Medline doi:10.1126/science.1244303

8. A. Capretti, Y. Wang, N. Engheta, L. Dal Negro, Enhanced third-harmonic generation in Si-compatible epsilon-near-zero indium tin oxide nanolayers. *Opt. Lett.* **40**, 1500–1503 (2015). Medline doi:10.1364/OL.40.001500

9. T. S. Luk, D. de Ceglia, S. Liu, G. A. Keeler, R. P. Prasankumar, M. A. Vincenti, M. Scalora, M. B. Sinclair, S. Campione, Enhanced third harmonic generation from the epsilon-near-zero modes of ultrathin films. *Appl. Phys. Lett.* **106**, 151103 (2015). doi:10.1063/1.4917457

10. N. Kinsey, C. DeVault, J. Kim, M. Ferrera, V. M. Shalaev, A. Boltasseva, Epsilon-near-zero Al-doped ZnO for ultrafast switching at telecom wavelengths. *Optica* **2**, 616 (2015). doi:10.1364/OPTICA.2.000616

11. G. V. Naik, V. M. Shalaev, A. Boltasseva, Alternative plasmonic materials: Beyond gold and silver. *Adv. Mater.* **25**, 3264–3294 (2013). Medline doi:10.1002/adma.201205076

12. E. Feigenbaum, K. Diest, H. A. Atwater, Unity-order index change in transparent conducting oxides at visible frequencies. *Nano Lett.* **10**, 2111–2116 (2010). Medline doi:10.1021/nl1006307

13. M. Sheik-Bahae, A. A. Said, T.-H. Wei, D. J. Hagan, E. W. Van Stryland, Sensitive measurement of optical nonlinearities using a single beam. *IEEE J. Quantum Electron.* **26**, 760–769 (1990). doi:10.1109/3.53394

14. B. K. Rhee, J. S. Byun, E. W. Van Stryland, Z scan using circularly symmetric beams. *J. Opt. Soc. Am. B* **13**, 2720 (1996). doi:10.1364/JOSAB.13.002720

15. H. I. Elim, W. Ji, F. Zhu, Carrier concentration dependence of optical Kerr nonlinearity in indium tin oxide films. *Appl. Phys. B* **82**, 439–442 (2006). doi:10.1007/s00340-005-2079-8

16. See supplementary materials on *Science* Online.

17. R. W. Boyd, *Nonlinear Optics* (Elsevier, 2008).

18. C. Sun, F. Vallée, L. Acioli, E. P. Ippen, J. G. Fujimoto, Femtosecond investigation of electron thermalization in gold. *Phys. Rev. B Condens. Matter* **48**, 12365–12368 (1993). Medline doi:10.1103/PhysRevB.48.12365

19. S. D. Brorson, J. G. Fujimoto, E. P. Ippen, Femtosecond electronic heat-transport dynamics in thin gold films. *Phys. Rev. Lett.* **59**, 1962–1965 (1987). Medline doi:10.1103/PhysRevLett.59.1962

20. E. Carpene, Ultrafast laser irradiation of metals: Beyond the two-temperature model. *Phys. Rev. B* **74**, 024301 (2006). doi:10.1103/PhysRevB.74.024301

21. B. Rethfeld, A. Kaiser, M. Vicanek, G. Simon, Ultrafast dynamics of nonequilibrium electrons in metals under femtosecond laser irradiation. *Phys. Rev. B* **65**, 214303 (2002). doi:10.1103/PhysRevB.65.214303

22. D. de Ceglia, S. Campione, M. A. Vincenti, F. Capolino, M. Scalora, Low-damping epsilon-near-zero slabs: Nonlinear and nonlocal optical properties. *Phys. Rev. B* **87**, 155140 (2013). doi:10.1103/PhysRevB.87.155140

23. B. Yao, L. Ren, X. Hou, Z-scan theory based on a diffraction model. *J. Opt. Soc. Am. B* **20**, 1290 (2003). doi:10.1364/JOSAB.20.001290

24. C. Kwak, Y. Lee, S. Kim, Analysis of asymmetric *Z*-scan measurement for large optical nonlinearities in an amorphous As_2S_3 thin film. *J. Opt. Soc. Am. B* **16**, 600–604 (1999). doi:10.1364/JOSAB.16.000600

25. M. Conforti, G. Della Valle, Derivation of third-order nonlinear susceptibility of thin metal films as a delayed optical response. *Phys. Rev. B* **85**, 245423 (2012). doi:10.1103/PhysRevB.85.245423

26. N. Del Fatti, C. Voisin, M. Achermann, S. Tzortzakis, D. Christofilos, F. Vallée, Nonequilibrium electron dynamics in noble metals. *Phys. Rev. B* **61**, 16956–16966 (2000). doi:10.1103/PhysRevB.61.16956

27. C. Voisin, N. Del Fatti, D. Christofilos, F. Vallée, Ultrafast electron dynamics and optical nonlinearities in metal nanoparticles. *J. Phys. Chem. B* **105**, 2264–2280 (2001). doi:10.1021/jp0038153

28. J. J. Lin, Z. Q. Li, Electronic conduction properties of indium tin oxide: Single-particle and many-body transport. *J. Phys. Condens. Matter* **26**, 343201 (2014). Medline doi:10.1088/0953-8984/26/34/343201

29. D. Pines, *Elementary Excitations in Solids: Lectures on Phonons, Electrons, and Plasmons* (Advanced Book Classics, 1966).

30. F. Ladstädter, U. Hohenester, P. Puschnig, C. Ambrosch-Draxl, First-principles calculation of hot-electron scattering in metals. *Phys. Rev. B* **70**, 235125 (2004). doi:10.1103/PhysRevB.70.235125

31. M. Kaveh, N. Wiser, Electron-electron scattering in conducting materials. *Adv. Phys.* **33**, 257–372 (1984). doi:10.1080/00018738400101671

32. N. W. Ashcroft, N. D. Mermin, *Solid State Physics* (Brooks Cole Publishing, 1976).

3 OPTICAL RESPONSE OF DIPOLE ANTENNAS ON AN EPSILON-NEAR-ZERO SUBSTRATE

CONTRIBUTION STATEMENT:

It is almost fashionable to incorporate plasmonic structures to enhance the local optical field as a way of increasing the efficiency or sensitivity of linear and nonlinear optical effects. We started this project purely out of curiosity. My involvement with the project started with helping A. Tahir to build the experimental setup and collect data. After the initial round of data collection, we were quite surprised by the results exhibiting double dips in the transmission curves that agreed with the simulation. Most nights during the fall of 2015 I slept on a couch in an empty room in the lab (that room later became the laboratory of Professor Ebrahim Karimi). During one such night in late fall of 2015, I was bored in the lab and was randomly browsing the web when I came across a paper from Lukas Novotny[1]. Motivated by that paper I performed a series of numerical simulations to investigate the source of the two dips while taking a break from my laboratory work. By the time everyone else came to the office the next morning, the source of the effect was obvious: a near-field strong coupling between two oscillators with large oscillator strengths. I subsequently helped to perform the numerical analysis and write the manuscript.

1 Novotny, L. (2010). Strong coupling, energy splitting, and level crossings: A classical perspective. American Journal of Physics, 78(11), 1199-1202.

PHYSICAL REVIEW A **93**, 063846 (2016)

Optical response of dipole antennas on an epsilon-near-zero substrate

Sebastian A. Schulz,[1] Asad A. Tahir,[1] M. Zahirul Alam,[1] Jeremy Upham,[1] Israel De Leon,[1,2,*] and Robert W. Boyd[1,3]

[1]*Department of Physics and Max Planck Centre for Extreme and Quantum Photonics, University of Ottawa, 25 Templeton Street, Ottawa, K1N 6N5, Canada*

[2]*School of Engineering and Sciences, Tecnológico de Monterrey, Monterrey, Nuevo León 64849, Mexico*

[3]*Institute of Optics and Department of Physics and Astronomy, University of Rochester, 275 Hutchison Road, Rochester, New York 14627, USA*

(Received 11 March 2016; published 27 June 2016)

Materials with vanishing permittivity (epsilon-near-zero or ENZ materials) show unconventional optical behavior. Here we show that plasmonic dipole antennas on an ultrathin ENZ substrate have properties significantly different from antennas on a traditional substrate. Specifically, the presence of a 23-nm-thick ENZ material strongly modifies the linear response of plasmonic antennas and, as a result, the resonant wavelength is independent of the linear dimensions of the dipole antenna.

DOI: 10.1103/PhysRevA.93.063846

I. INTRODUCTION

The epsilon-near-zero (ENZ) property of materials, both naturally occurring or artificial metamaterials, promises new avenues for optics [1,2]. In the ENZ range of the spectrum the real part of the permittivity, ϵ, approaches or crosses zero while the imaginary part usually remains finite. The near-zero response can be obtained in various material systems, including highly doped semiconductors [3], metal-dielectric composite structures [4], or in integrated optical platforms [5,6]. Materials that posses an ENZ spectral region exhibit many unusual optical properties, including nearly arbitrary control of light propagation [7–11] and the wielding of diverse nonlinear phenomena [12–14]. One particular area of interest is the effect of this vanishing permittivity on nearby optical structures [8,9,15–17].

Recently there has been a tremendous interest in designing metasurfaces with tailored electromagnetic properties [18–20]. In this letter we discuss the impact of an ultrathin ENZ substrate on the optical behavior of plasmonic antenna arrays that are designed for operation near the ENZ spectral region. We choose the array dimensions such that there is no near-field coupling between the dipole antennas. We find that in such a hybrid plasmonic-ENZ system strong coupling occurs between the antenna resonance and modes within the ENZ layer. Consequently, the resonance is split, with the resonance wavelength independent of variations in the antenna dimensions. We further investigate the field distribution within the hybrid ENZ-antenna system.

II. CONSTITUENT COMPONENTS

The ENZ material employed for our study is a thin layer of indium tin oxide (ITO), a degenerate semiconductor that exhibits a vanishing real part of the permittivity in the near-infrared spectral region. The ITO was obtained from a commercial supplier and consists of a 23-nm-thick ITO film on a 1.1-mm-thick float glass substrate. We determined the permittivity of the ITO layer over a broad wavelength range through spectroscopic ellipsometry, with the results shown in Fig. 1. We observe that the real part of the permittivity, ϵ, is zero at $\lambda_0 = 1417$ nm and remains between 1 and –1 for the spectral region spanning from 1200 nm to 1600 nm.

Thin ENZ material layers, such as the one employed here, support optical modes with a large local density of states [21]. We obtain the dispersion curve of our bare ITO-glass substrate by computing the local minima of the substrate's reflectance spectrum using the Nelder-Mead method. The generated dispersion diagram is shown in Fig. 1(b), where two modes can be identified: the Brewster mode and the Ferrell-Berreman mode [21–23]. The Ferrell-Berreman mode has a high density of states [21], as demonstrated by its shallow slope. Since this mode is formed in a film that is thinner than the skin depth in ITO, the transverse field is expected to be constant throughout the film when it is excited [24]. The portion of the Ferrell-Berreman mode below the light line is sometimes also referred to as the ENZ mode. We note that the modes in the ITO layer are not excited under normal incidence illumination. Such illumination results in a monotonically decreasing transmission with increasing wavelength (the transmission drops from 94% to 78%), due to the increased absorption in the ITO layer, see green curve in Fig. 1(a).

Due to its large density of states, the Ferrell-Berreman mode can significantly alter the properties of nearby optical scatterers. To study this phenomenon, we fabricated multiple arrays of gold antennas on the ITO substrate [see Fig. 2(a)]. The antennas were designed to have their fundamental resonance near the ENZ spectral region of the ITO film, in the absence of the ITO layer, as shown in Fig. 2(b). Each array has a square lattice with a fixed period of 600 nm. All antennas have a length of 404 ± 8 nm and their width varies across the arrays, from 37 nm to 77 nm. These dimensions were confirmed through scanning electron microscopy (SEM) measurements. Fabrication was performed according to the recipe in Ref. [20], using a Raith Pioneer electron-beam lithography system, followed by gold evaporation and liftoff.

It is well known that a dipole antenna has a single optical resonance, for light polarized parallel to the antenna length. This resonance is strongly dependent on the dimensions, both length and width, of the antenna [25,26]. Figure 2(b) shows how the resonance wavelength, obtained from finite-difference-time-domain (FDTD) simulations, shifts for dipole antennas of the various dimensions used in our experiment, but

*ideleon@itesm.mx

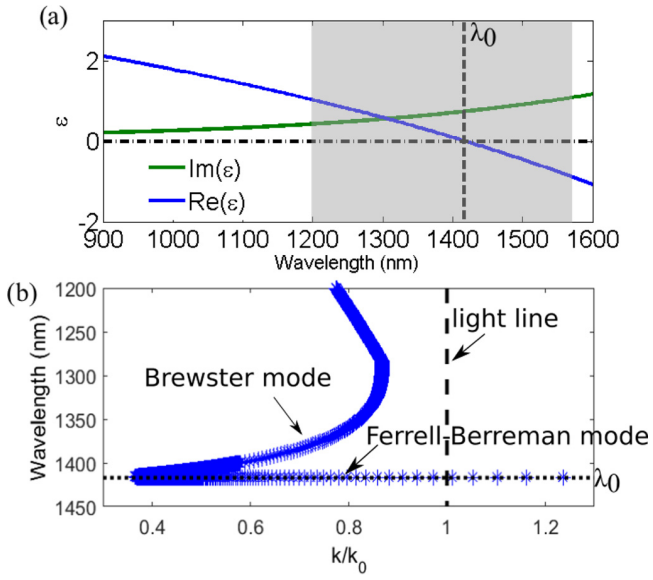

FIG. 1. (a) Experimentally obtained permittivity for the 23-nm-thick ITO layer. The real part of ϵ crosses zero at 1417 nm. The gray shading indicates the region of the spectrum where $-1 \leqslant \epsilon \leqslant 1$. (b) Dispersion relation for the modes supported by the 23-nm-thick ITO layer on a glass substrate. The black dotted and dashed lines represent the wavelength at which $\mathrm{Re}(\epsilon) = 0$ (λ_0) and the air (top cladding) light line, respectively. k_0 is the free space wave vector. The plot shows that the Ferrell-Berreman mode has a high density of states, indicated by the shallow slope in this plot, near λ_0.

on a simple glass substrate without the ENZ layer. It is clearly visible that the resonance wavelength is strongly dependent on the geometric parameters; in this case, reducing the width from 77 nm to 37 nm results in a redshift of over 200 nm.

III. CHARACTERIZATION

For our experimental study, we measured the transmission of light (normalized to transmission through the bare ITO film on glass) from a tungsten halogen source through the sample and detected the transmitted light using an optical spectrum analyzer. A polarizer was used to select only the polarization of light parallel to the antenna. Our measurements, shown in Fig. 2(c), reveal that there is a strong resonance in the region of $1320\,\mathrm{nm} \leqslant \lambda \leqslant 1380\,\mathrm{nm}$ for all arrays. However, we observe that the resonance of the dipole antennas on ITO is almost independent of the antenna dimensions. This is in contrast to the behavior of an identical set of antenna arrays on glass (without ITO) simulated earlier, which exhibit a redshift of the resonance wavelength that exceeds 200 nm. In the combined system, the main impact of changing the antenna dimension is a change of the extinction ratio, from a 30% to a 45% dip in the on-resonance transmission. Furthermore, while the antennas on glass have a symmetric resonance, the combined system has a strongly asymmetric spectral behavior, with suppressed transmission on the long-wavelength edge of the resonance. A similar behavior can be observed in FDTD simulations of the dipole antennas on our ENZ substrate [dashed lines in Fig. 2(c)]. The observation of an asymmetric resonance, with the resonant wavelength being independent of

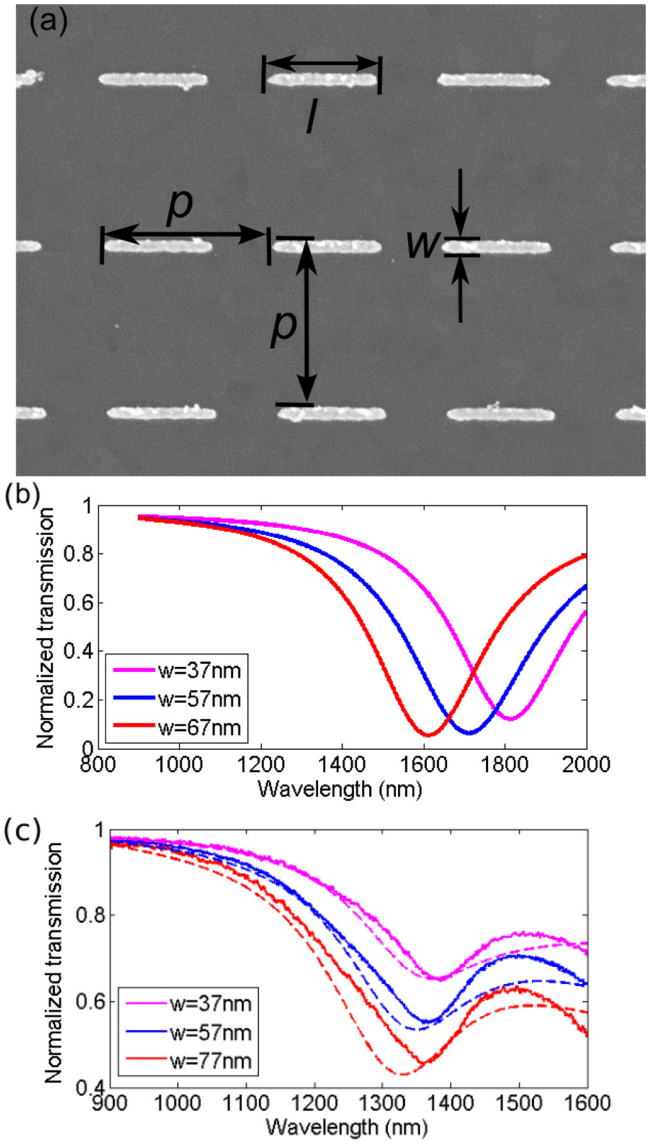

FIG. 2. (a) Scanning electron microscope image of an antenna array outlining the design parameters length l, width w, and period p. The period corresponds to 600 nm. (b) Simulated transmission spectra of three arrays of dipole antennas on glass, without the ENZ substrate. The resonance wavelength is redshifted as w is decreased at constant l. The simulated antennas have a periodicity of 600 nm, a length of 404 ± 8 nm, and a width of 37 nm (magenta/light gray), 57 nm (blue/dark gray), and 77 nm (red/medium gray), respectively, matching the dimensions of the antennas fabricated on the ENZ substrate. (c) Experimental (solid lines) and simulated (dashed lines) transmission curves for three antenna arrays, with the same dimensions as panel (b). All transmission curves are normalized to the transmission through a bare ITO film on glass.

the antenna dimensions, is a remarkable consequence of the strong interaction between the optical modes of the plasmonic antenna and those of the thin ENZ layer.

IV. DISCUSSION

We now discuss the physics underlying the observed optical behavior. From Fig. 2(c) we note that the resonance spectra

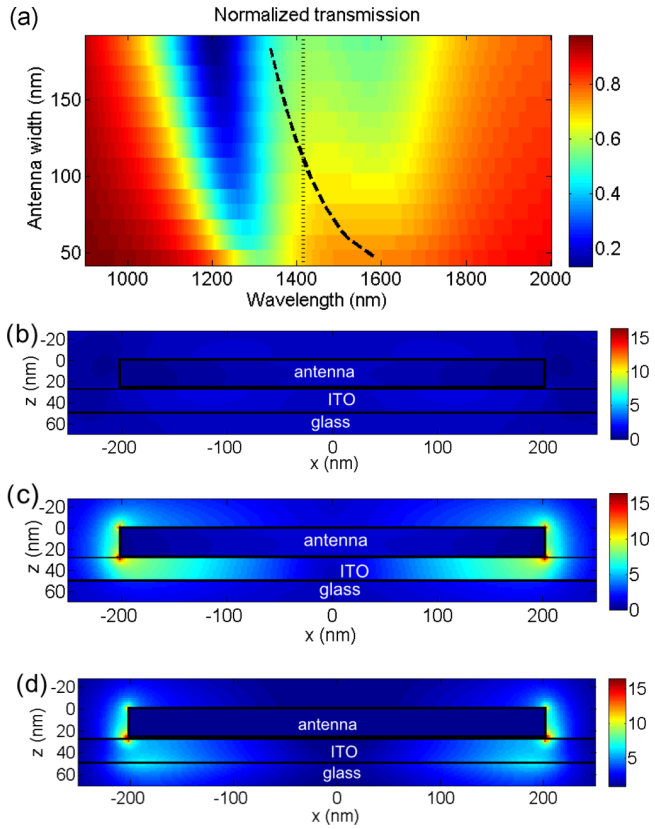

FIG. 3. (a) Evolution of the combined dipole antenna-ENZ substrate resonance with varying antenna width. The color indicates the simulated transmission through the system. The dotted and dashed lines indicate the Ferrell-Berreman mode, at λ_0, and the resonance wavelength of the same dipole antennas on a glass substrate, respectively. (b–d) Electric field strength plots, along the antenna cross section, for an antenna with a length of 400 nm and a width of 57 nm. The color indicates the field strength, normalized to the incident light. (b) At $\lambda = 1.0\,\mu$m, away from the antenna resonance and outside the ENZ region. (c) At $\lambda = 1.35\,\mu$m, in the ENZ region and at the observed resonance. (d) At $\lambda = 1.67\,\mu$m, centered on the second resonance dip, close to the resonance wavelength of the antenna in the absence of the ENZ layer.

are characterized by two transmission dips, one occurring for wavelength slightly shorter than λ_0 and the second occurring for wavelengths above 1550 nm; for the most part these wavelengths were inaccessible in our experiment, due to limitations on the detection bandwidth. These spectra exhibit a strong splitting of the antenna's dipole resonance, occurring near λ_0, where the ITO film supports the Ferrell-Berreman mode. To investigate this behavior further, we performed FDTD simulations of a larger range of antenna dimensions and over a larger wavelength range, mapping the evolution of the combined ENZ-dipole antenna system. We also calculate the field distribution of the excited modes. Figure 3(a) shows the evolution of the resonance as the antenna width is increased. Note that the antenna length was reduced to 350 nm for these simulations to achieve a better spectral overlap of the antenna resonance and the ENZ spectral region. We see that the system has two resonances, with both an increasing extinction and increasing separation between the resonances as the antenna width increases. Increasing the antenna width results in stronger coupling between the ENZ layer and the antenna resonance, as an increased width leads to a blueshift of the antenna resonance wavelength. Therefore we attribute the observed behavior to a strong coupling between the Ferrell-Berreman mode of the ITO film and the antenna resonance, consistent with recent observations by Campione *et al.* [17], where a dependence of the splitting on the ITO film thickness was demonstrated. A similar splitting is not observed for the case of thick ITO films [27], which do not support the Ferrel-Berreman mode.

We now further investigate the nature of the observed resonances. We can separate the transmission spectra into three distinct regions: short wavelengths, below both resonances; near the shorter wavelength resonance; and near the longer wavelength resonance. The first spectral region is away from either resonance and outside of the ENZ region. Here, the light only weakly interacts with the dipole antenna and the ENZ layer, and consequently, strong transmission is observed. This is confirmed by the lack of field enhancement observed in the cross section shown in Fig. 3(b). As the wavelength is increased we enter the second and third spectral regions, where the two resonances are located. Figures 3(c) and 3(d) show the field distributions for the two resonances. At the shorter wavelength resonance, the field is enhanced on the antenna and in the ENZ layer. Except at the termination of the antenna, the field distribution within the ITO layer shows the main hallmarks of the Ferrell-Berreman mode, i.e., a weak z dependence within this layer and an abrupt termination at the ITO-glass interface [24]. Since the ENZ wavelength is independent of the antenna dimensions, the resonance wavelength associated with this mode is constant for all arrays. However, antennas in different arrays have different scattering cross sections and a different resonance wavelengths. Therefore, they have varying interaction strengths with the incident light in this wavelength region and different coupling strengths with the Ferrell-Berreman mode, resulting in the different transmission values observed in Figs. 2(c) and 3(a). We note that in this wavelength range the electric field in the ENZ medium is significantly enhanced [see Fig. 3(c)]. For example, ignoring the hot spots formed at the sharp edges of the antenna, we obtain a six- to eightfold field enhancement in the ENZ medium, corresponding to an enhancement of the field intensity of approximately 50. From Fig. 3(d) we observe that the field distribution associated with this second, longer wavelength resonance has two separate regions with field enhancement, near the antenna and at the ITO-glass interface. In this wavelength region the ITO layer does not support the Ferrell-Berreman mode anymore but supports a leaky surface mode confined to the ITO-air interface. This mode is heavily damped by radiative and material losses. Therefore the field is confined tightly to the dipole antenna, has a z-dependent field distribution within the ITO layer, and shows a modest field enhancement at the ITO-glass boundary, associated with a weak coupling to the surface plasmon modes.

V. CONCLUSION

We have shown that the presence of a thin ENZ substrate strongly affects the optical response of antenna arrays

operating in the ENZ spectral region through a strong coupling between the Ferrell-Berreman mode in the ENZ substrate and the antenna resonance. Far away from the antenna resonance and outside of the ENZ region, light is only weakly affected by the system, while closer to the wavelength where $\mathrm{Re}(\epsilon) = 0$ the Ferrell-Berreman mode and the fundamental resonance of the dipole antenna strongly couple, leading to a splitting of the antenna resonance into two new resonances. In addition, our optical field analysis shows that these two resonances have very different optical behavior. On one resonance the field is enhanced both on the antenna and within the ITO layer, where the Ferrell-Berreman mode is exited. On the other resonance, the field enhancement is limited to regions near the dipole antenna, with weak coupling to lossy surface plasmon modes at the ITO-glass boundary. Our work provides a simple model describing the optical behavior of dipole antenna arrays on thin ENZ substrates and paves the way toward uses of such structures, for example, for further enhancement of the already strong nonlinear response of ENZ systems [3,10].

ACKNOWLEDGMENTS

We gratefully acknowledge the support of the Canada Excellence Research Chair (CERC) program and from NSERC.

[1] N. Engheta, Science **340**, 286 (2013).
[2] A. Alù, M. G. Silveirinha, A. Salandrino, and N. Engheta, Phys. Rev. B **75**, 155410 (2007).
[3] M. Z. Alam, I. D. Leon, and R. W. Boyd, Science **352**, 795 (2016).
[4] S. Molesky, C. Dewalt, and Z. Jacob, Opt. Express **21**, A96 (2013).
[5] R. Maas, J. Parsons, N. Engheta, and A. Polman, Nat. Photonics **7**, 907 (2013).
[6] Y. Li, S. Kita, P. Muñoz, O. Reshef, D. I. Vulis, M. Yin, M. Lončar, and E. Mazur, Nat. Photonics **9**, 738 (2015).
[7] M. A. Vincenti, D. de Ceglia, A. Ciattoni, and M. Scalora, Phys. Rev. A **84**, 063826 (2011).
[8] C. Argyropoulos, P.-Y. Chen, G. D'Aguanno, N. Engheta, and A. Alù, Phys. Rev. B **85**, 045129 (2012).
[9] H. Aouani, M. Rahmani, M. Navarro-Cía, and S. a. Maier, Nat. Nanotechnol. **9**, 290 (2014).
[10] A. Capretti, Y. Wang, N. Engheta, and L. D. Negro, Opt. Lett. **40**, 1500 (2015).
[11] T. S. Luk, D. de Ceglia, S. Liu, G. A. Keeler, R. P. Prasankumar, M. A. Vincenti, M. Scalora, M. B. Sinclair, and S. Campione, Appl. Phys. Lett. **106**, 151103 (2015).
[12] R. Liu, Q. Cheng, T. Hand, J. J. Mock, T. J. Cui, S. A. Cummer, and D. R. Smith, Phys. Rev. Lett. **100**, 023903 (2008).
[13] D. C. Adams, S. Inampudi, T. Ribaudo, D. Slocum, S. Vangala, N. A. Kuhta, W. D. Goodhue, V. A. Podolskiy, and D. Wasserman, Phys. Rev. Lett. **107**, 133901 (2011).
[14] S. Savoia, G. Castaldi, V. Galdi, A. Alù, and N. Engheta, Phys. Rev. B **91**, 115114 (2015).
[15] Y. C. Jun, J. Reno, T. Ribaudo, E. Shaner, J.-J. Greffet, S. Vassant, F. Marquier, M. Sinclair, and I. Brener, Nano Lett. **13**, 5391 (2013).
[16] T. Galfsky, Z. Sun, Z. Jacob, and V. M. Menon, Opt. Mater. Express **5**, 2878 (2015).
[17] S. Campione, J. R. Wendt, G. A. Keeler, and T. S. Luk, ACS Photonics **3**, 293 (2016).
[18] N. Yu and F. Capasso, Nat. Mater. **13**, 139 (2014).
[19] D. Lin, P. Fan, E. Hasman, and M. L. Brongersma, Science **345**, 298 (2014).
[20] S. A. Schulz, J. Upham, F. Bouchard, I. D. Leon, E. Karimi, and R. W. Boyd, Opt. Mater. Express **5**, 2798 (2015).
[21] S. Vassant, J.-P. Hugonin, F. Marquier, and J.-J. Greffet, Opt. Express **20**, 23971 (2012).
[22] T. Taliercio, V. N. Guilengui, L. Cerutti, E. Tourine, and J.-J. Greffet, Opt. Express **22**, 24294 (2014).
[23] W. D. Newman, C. L. Cortes, J. Atkinson, S. Pramanik, R. G. D. Corby, and Z. Jacob, ACS Photonics **2**, 2 (2015).
[24] S. Campione, I. Brener, and F. Marquier, Phys. Rev. B **91**, 121408 (2015).
[25] L. Novotny, Phys. Rev. Lett. **98**, 266802 (2007).
[26] G. W. Bryant, F. J. Garcia de Abajo, and J. Azipurua, Nano Lett. **8**, 631 (2008).
[27] J. Kim, A. Dutta, G. V. Naik, A. J. Giles, F. J. Bezares, C. T. Ellis, J. G. Tischler, A. M. Mahmoud, H. Caglayan, O. J. Glembocki, A. V. Kildishev, J. D. Caldwell, A. Boltasseva, and N. Engheta, Optica **3**, 339 (2016).

4 LARGE OPTICAL NONLINEARITY OF NANOANTENNAS COUPLED TO AN EPSILON-NEAR-ZERO MATERIAL

CONTRIBUTION STATEMENT:

For this project, I performed the laboratory measurements and data analysis. Subsequently, I developed the numerical model and wrote the first draft. At first, we were expecting only a larger n_2 values due to field enhancement—but in the experiment, we observed very large Δn and the sign of n_2 also seemed to vary as a function of wavelength. Both of these were in total contradiction to our measurements of ITO film only. These results befuddled us for a while. The eureka moment came while I was biking along the Ottawa river—the sign and magnitude of Δn in this system are determined by the plasmonic antennas due to the time-varying resonance. A detailed account of contributions can be found in the section titled "Author contributions".

nature photonics

LETTERS

https://doi.org/10.1038/s41566-017-0089-9

Large optical nonlinearity of nanoantennas coupled to an epsilon-near-zero material

M. Zahirul Alam[1], Sebastian A. Schulz[1,2,3], Jeremy Upham[1], Israel De Leon[4*] and Robert W. Boyd[1,5]

The size and operating energy of a nonlinear optical device are fundamentally constrained by the weakness of the nonlinear optical response of common materials[1]. Here, we report that a 50-nm-thick optical metasurface made of optical dipole antennas coupled to an epsilon-near-zero material exhibits a broadband (~400 nm bandwidth) and ultrafast (recovery time less than 1 ps) intensity-dependent refractive index n_2 as large as -3.73 ± 0.56 cm^2 GW^{-1}. Furthermore, the metasurface exhibits a maximum optically induced refractive index change of ±2.5 over a spectral range of ~200 nm. The inclusion of low-Q nanoantennas on an epsilon-near-zero thin film not only allows the design of a metasurface with an unprecedentedly large nonlinear optical response, but also offers the flexibility to tailor the sign of the response. Our technique removes a longstanding obstacle in nonlinear optics: the lack of materials with an ultrafast nonlinear contribution to refractive index on the order of unity. It consequently offers the possibility to design low-power nonlinear nano-optical devices with orders-of-magnitude smaller footprints.

All-optical signal processing and computation are often hailed as breakthrough technologies for the next generation of computation and communication devices. Two important parameters of such devices—energy consumption and size—critically depend on the strength of the nonlinear optical response of the materials from which they are made. However, materials typically exhibit an extremely weak nonlinear optical response. This property makes designing subwavelength all-optical active devices extremely difficult. Therefore, all-optical active devices tend to have large footprints, which limits the integration density to many orders of magnitude smaller than what can be achieved in state-of-the-art electronic integrated circuits[2,3]. Thus, materials with much stronger nonlinear optical responses are needed to enable integrated high-density on-chip nonlinear optical devices.

Over the years, several approaches have been explored to enhance the intrinsic nonlinear optical response of materials, including local field enhancement using composite structures[4–6], plasmonic structures[7,8] and metamaterials[9–12]. However, these techniques offer only limited control over the magnitude (and sign when applicable) of the wavelength-dependent nonlinear response, and typically involve a trade-off between the strength of the nonlinearity and the spectral position of the peak nonlinear response. It has been reported recently that materials with vanishingly small permittivity—commonly known as epsilon-near-zero or ENZ materials—exhibit intriguing linear[13–17] and large nonlinear responses[1,18–21]. However, an ENZ material has a large nonlinear response over only a relatively narrow spectral range. Furthermore, the zero-permittivity wavelength, strength of the nonlinear response, and losses depend on the optical properties of the ENZ material. In comparison to previous works[1,18] where strong nonlinear responses were reported in ENZ materials, here we show that many of these constraints can be overcome by incorporating engineered nanostructures on an ENZ host material. Specifically, we report a new approach to engineer an optical medium with an unprecedentedly large intensity-dependent refractive index using nanoantennas coupled to a thin ENZ material. The simple design concepts presented here provide exquisite control over engineering the sign and magnitude of the nonlinear refractive index, and can be used in an all-dielectric CMOS-compatible fabrication process to miniaturize nonlinear optical devices by orders of magnitude. We experimentally demonstrate that a metasurface geometry is uniquely suited to engineer a broadband and ultrafast nonlinear response orders of magnitude larger than those of any previously reported solid-state materials at optical frequencies.

The rationale for using a coupled ENZ–nanoantenna system as the building block for nonlinear optical devices is straightforward. Let us consider an optical antenna placed on a material exhibiting an intensity-dependent refractive index. A laser beam that is nearly resonant with such a system experiences a large effective linear refractive index. However, the resonance wavelength of a nanoantenna depends on its geometrical parameters and the refractive index of the surrounding medium. Thus, a small change in the refractive index of the substrate material leads to a spectral shift of the system's linear resonance as a consequence of the dynamic variation of the resonance wavelength of the nanoantenna. As a result, a high-intensity beam at a nearly resonant wavelength experiences a significantly different refractive index than that experienced by a low-intensity beam, as illustrated in Fig. 1, resulting in a large effective nonlinear refractive index change of the ENZ–nanoantenna system, Δn. Moreover, the field enhancement provided by the nanoantennas decreases the energy requirements for the nonlinear response. As a result, such a system can exhibit a broadband and large intensity-dependent refractive index.

We note that Δn can be either positive or negative, depending on the spectral position of the optical signal relative to that of the resonance at low intensity. Therefore, the sign, magnitude, wavelength position and bandwidth of Δn are no longer constrained by the ENZ substrate, but instead can be tailored by plasmonic or dielectric nanoresonators. These features make the system flexible enough to engineer both the magnitude and sign of the nonlinear response simply by engineering the linear dispersion, by appropriately choosing the antenna parameters and by choosing an ENZ host that exhibits the required nonlinear response[1,18].

We demonstrate the principle of operation using a metasurface[22–28] consisting of a two-dimensional array of gold optical

[1]Department of Physics, University of Ottawa, Ottawa, ON, Canada. [2]Centre for Advanced Photonics and Process Analysis, Cork Institute of Technology, Cork, Ireland. [3]Tyndall National Institute, Cork, Ireland. [4]School of Engineering and Sciences, Tecnologico de Monterrey, Monterrey, NL, Mexico. [5]Institute of Optics and Department of Physics and Astronomy, University of Rochester, Rochester, NY, USA. *e-mail: ideleon@itesm.mx

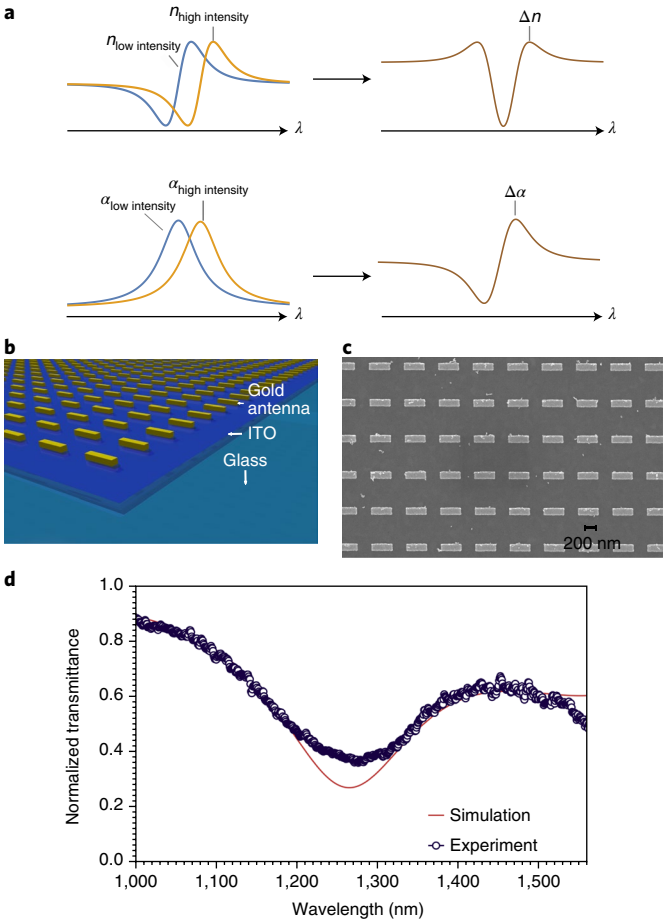

Fig. 1 | Design concept and linear response of the coupled structure. **a**, A small nonlinear change in the substrate material's refractive index results in a significant spectral shift of the resonance wavelength of an antenna. As a result, light of high intensity experiences a dramatically different refractive index (Δn) and a different absorption ($\Delta\alpha$) compared with those experienced by low-intensity light. **b**, The structure is composed of a gold dipole antenna array of 27 nm thickness on a glass substrate. A 23-nm-thick indium tin oxide (ITO) layer is sandwiched between the antenna array and the glass substrate. **c**, Scanning electron microscopy micrograph of the fabricated antenna array. **d**, The thin ENZ medium supports a bulk plasma mode near the zero-permittivity wavelength[30,43–45]. When a dipole antenna array with resonance at ~1,420 nm (due only to the presence of the glass substrate) is placed on an ITO–glass substrate, the transmission curve shows a splitting of the transmission resonance due to strong coupling between the fundamental mode of each antenna and the ENZ mode[31,32]. The variation between the experimental result and the FDTD simulation—with antennas of dimension 362 nm × 108 nm × 27 nm—can be attributed to inhomogeneous broadening of the linewidth of the antennas due to fabrication imperfections.

antennas on a thin ENZ layer, which in turn is deposited on a glass substrate (Fig. 1b). In this structure, an antenna plays three crucial roles: (1) it dictates the linear dispersion of the overall system, being responsible for a large effective refractive index at frequencies near-resonance; (2) it efficiently couples light at normal incidence to the ENZ layer; and (3) it provides a moderate optical field enhancement. We find that the interaction of the antennas with the ENZ layer simulatenously increases the refractive index change Δn for a constant incident intensity compared to the bare ENZ, and lowers the intensity threshold for the onset of the nonlinear response due to the moderate field enhancement inside the ENZ layer.

We used a 23-nm-thick film of indium tin oxide (ITO) as the ENZ layer. The real part of the permittivity of ITO crosses zero at $\lambda \approx 1{,}420$ nm. We chose the geometric parameters of the antenna such that its fundamental dipole resonance occurs at this wavelength. The thin ITO layer supports a lossy bulk-plasma mode at the zero-permittivity wavelength[29–31]. The linear optical transmission measurement of the metasurface (Fig. 1d) shows two distinct dips that result from the strong coupling-induced splitting between the fundamental mode of the antenna and the bulk-plasma mode of the ENZ layer. The coupled system exhibits two resonances, a main resonance centred at $\lambda = 1{,}280$ nm and a weaker resonance centred at $\lambda \approx 1{,}640$ nm. The wavelength separation between the resonances (~330 nm) is larger than the 3 dB linewidth of the antenna resonance on glass substrate alone (~30 nm)[31,32]. This strong coupling plays a significant role in the nonlinear response of the system.

We performed a series of Z-scan measurements[33] for various laser wavelengths to characterize the nonlinear response of the metasurface at normal incidence. We kept the incident intensity at the focus nearly constant at $I \approx 0.150$ GW cm^{-2} for all wavelengths. The polarization of the incident optical field was always along the long axis of the antenna. The metasurface exhibits both an intensity-dependent refractive index and an intensity-dependent absorption. The former is characterized by the effective nonlinear refractive index, $n_2 = \Delta n/I$, and the latter by the effective nonlinear absorption coefficient, $\beta = \Delta\alpha/I$, where Δn and $\Delta\alpha$ are, respectively, the changes in the effective refractive index and in the effective absorption resulting from illuminating the medium with an incident intensity of I. The results are shown in Fig. 2a,b. We find that the nonlinear response is strongly enhanced across the entire spectral range of interest, $1{,}180\ \text{nm} \le \lambda \le 1{,}560$ nm. The sign and magnitude of the nonlinear parameters depend on which side of the linear resonance is under investigation, and can be reproduced using a semi-quantitative numerical model describing the redshift of the linear dispersion of the coupled structure caused by the positive-valued intensity-dependent refractive index of ITO (see Supplementary Section 'Two-temperature model').

The metasurface displays a feature-rich and wavelength-dependent nonlinear response that can be used to control both the magnitude and the sign of the nonlinear parameters. The measured n_2 (Fig. 2a) show extremely large values at the negative ($\lambda = 1{,}240$ nm) and positive ($\lambda = 1{,}300$ nm) peaks, associated with the main resonance of the system. The absolute maximum response $|n_2| = 3.73 \pm 0.56$ cm^2 GW^{-1} is almost 2,000 times larger than the maximum n_2 of the bare 23-nm-thick ITO at $\lambda = 1{,}400$ nm (see Supplementary Section 'Nonlinear response of ITO') and is three orders of magnitude larger than that of a recently reported highly nonlinear metamaterial[19]. The magnitude of n_2 decreases steadily as a function of increasing wavelength ($\lambda > 1{,}300$ nm). Nevertheless, even at a red-detuned wavelength ($\lambda = 1{,}480$ nm), the nonlinear index, $n^2 = 0.589 \pm 0.088$ cm^2 GW^{-1}, is six orders of magnitude larger than that of silica glass and over two orders of magnitude larger than the nonlinearity of a high-conductivity ITO film at the ENZ region at normal incidence[1]. Similarly, the measured values of β (Fig. 2b) have a positive or negative sign depending on the optical wavelength. The values of β for $\lambda < 1{,}250$ nm and $\lambda > 1{,}440$ nm are negative, indicating saturable absorption, whereas the values for $1{,}250\ \text{nm} < \lambda < 1{,}440$ nm are positive, indicating reverse saturable absorption. The absolute maximum value of β is a factor of three smaller than that of a highly nonlinear metamaterial made of structured plasmonic metamolecules[11]. Alternatively, one could design the antenna array in a way to exhibit a much larger β range[34] to realize an ultralow-power saturable or reverse saturable absorber for applications in ultrafast lasing, optical limiters and on–off all-optical switching.

The nonlinear dynamics of the overall system are primarily dictated by the nonlinear response of the ITO film[1]. A positive change

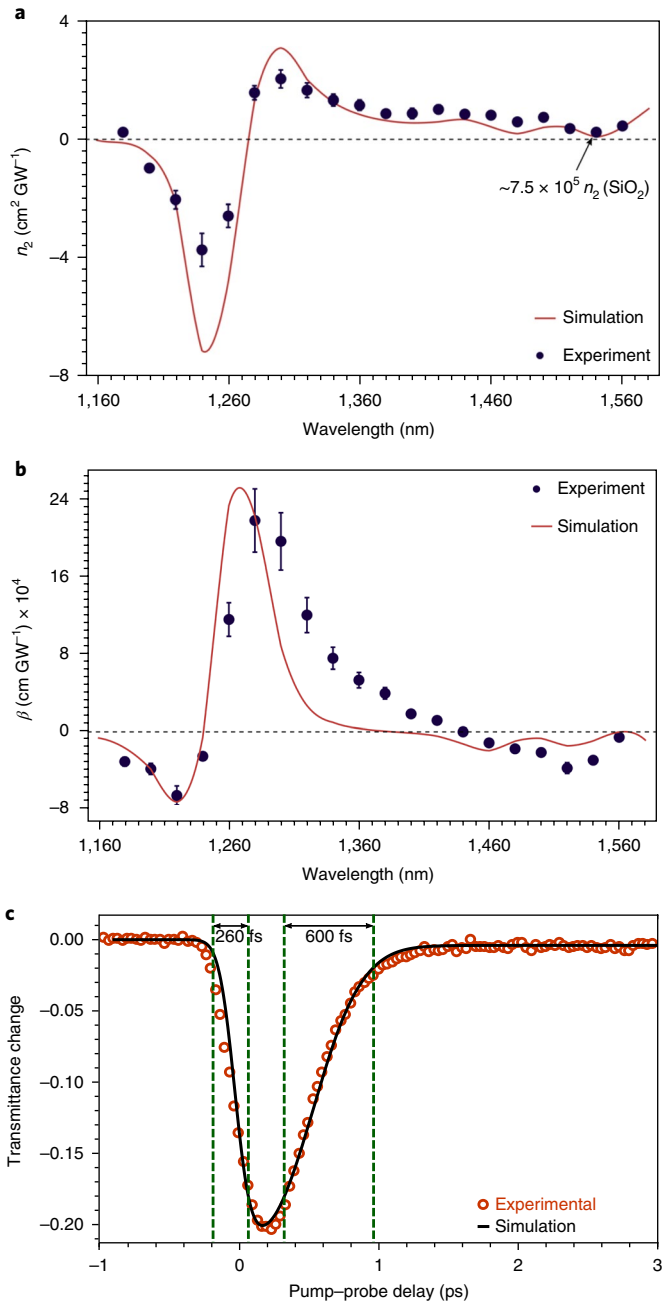

Fig. 2 | Nonlinear response of the coupled system. a, Effective nonlinear refractive index n_2, measured using a *Z*-scan technique. The metasurface exhibits a large nonlinear response. The intensity-dependent refractive index of the metasurface is almost six orders of magnitude larger than that of SiO_2, even for a highly red-detuned wavelength ($\lambda = 1{,}540$ nm). **b**, Nonlinear absorption β. Solid lines show the simulated n_2 and β values, calculated using a two-temperature model while taking the non-parabolic conduction band structure of the ITO into consideration (see Supplementary Section 'Electronic dispersion relation in ITO'). The semi-quantitative numerical simulation predicts the main features of the wavelength-dependent nonlinear response. Error bars correspond to the uncertainity in measured values due to distortion of the *Z*-scan traces. **c**, Pump-induced change in the transmittance of the probe at 1,280 nm. Dashed vertical lines represent the 10–90% transient time. The slow recovery time is dictated by the electron–phonon coupling strength and the quality factor of the resonance of the coupled system.

in the refractive index of ITO—resulting from an ultrafast redshift of the plasma frequency—leads to a redshift of the main resonance of the coupled system due to the change in the coupling conditions between the antenna and the bulk plasmon mode of the ITO. A laser pulse at a red-detuned (blue-detuned) wavelength thus experiences an increase (decrease) in effective refractive index, that is, a positive (negative) value of the intensity-dependent refractive index. Thus, by choosing appropriate geometric parameters of the antenna array and the zero-permittivity wavelength of the ENZ film, one can control the sign of the nonlinearity.

We studied the temporal dynamics of the resonant nonlinear response using a degenerate pump–probe transmittance measurement at $\lambda = 1{,}280$ nm. The measurement (Fig. 2c) revealed a rise time of ~260 fs and recovery time of ~600 fs. The rise-time measurement was constrained by the temporal width of the pump pulse, suggesting an onset of nonlinearity with sub-100 fs dynamics. The total response time (the rise time plus the recovery time) at the resonant wavelength is only 53% larger than that of the bare ITO film (see Supplementary Information Fig. 10). The relatively slower response time can be attributed to the resonance effect of the coupled structure. The nonlinear response of the coupled structure can be further improved by using nanoantennas with higher quality factor *Q*, but possibly at the expense of a slower response time[35].

Finally, we investigated the nonlinear contribution to the refractive index at higher intensities by measuring the nonlinear phase shift $\Delta\phi$ as a function of intensity at four different wavelengths (Fig. 3), two tuned to the main resonance ($\lambda = 1{,}250$ nm and $\lambda = 1{,}265$ nm) and two red-detuned from the main resonance ($\lambda = 1{,}360$ nm and $\lambda = 1{,}440$ nm). The maximum resonant nonlinear phase shift was $\Delta\phi = 0.677$ rad, which can occur due to a refractive index change of approximately −2.74 for propagation through a 50-nm-thick material. Even at $\lambda = 1{,}440$ nm (a highly red-detuned wavelength), the change to the refractive index is ~2.6, while the change in the transmittance is less than 6%. Such a broadband, large and ultrafast optically induced change in the refractive index is unprecedented. In most cases, saturation effects become evident for an incident energy density larger than ~2 pJ μm^{-2}, which is lower than the damage threshold of the gold antennas. The saturation of Δn can be attributed to various causes, including large damping of the low-conductivity ITO, which limits the maximum achievable temperature of the free electrons. Furthermore, the increased electron temperature spectrally widens the resonance of the coupled structure, limiting the maximum phase shift achievable. Thus, ENZ materials with lower intrinsic damping could increase the saturation threshold. The nonlinear response could be further enhanced by maximizing the overlap between the near-field of the antennas and the ITO layer, by choosing antennas (dielectric or metallic) with higher quality factors, and by choosing an ENZ material with lower intrinsic damping[18,36].

We note that when the ENZ medium is sufficiently thick, the antenna resonance becomes locked to the zero permittivity wavelength of the ENZ material[37]. Nevertheless, a metasurface that incorporates a thick ENZ material will also exhibit an enhanced nonlinear response because a dynamic change in the substrate's refractive index necessarily modifies the resonance wavelength of the antenna. The strategy introduced in this Letter can be considered as a temporal analogue of the typical space-gradient metasurface[22–25,27]. Thus, by combining both strategies one could design an all-optical space–time gradient metasurface to break the geometrical and temporal symmetry on-chip[38,39], design ultrafast temporal holograms and control the directivity of emission using an optical gate signal[40,41].

In summary, we have demonstrated that a metasurface geometry is uniquely suited to achieving large nonlinear refraction. We have shown that a metasurface may exhibit an extremely large intensity-dependent refractive index if an ENZ medium is incorporated into the design. The technique introduced in this Letter offers flexibility in customizing both the wavelength-dependent

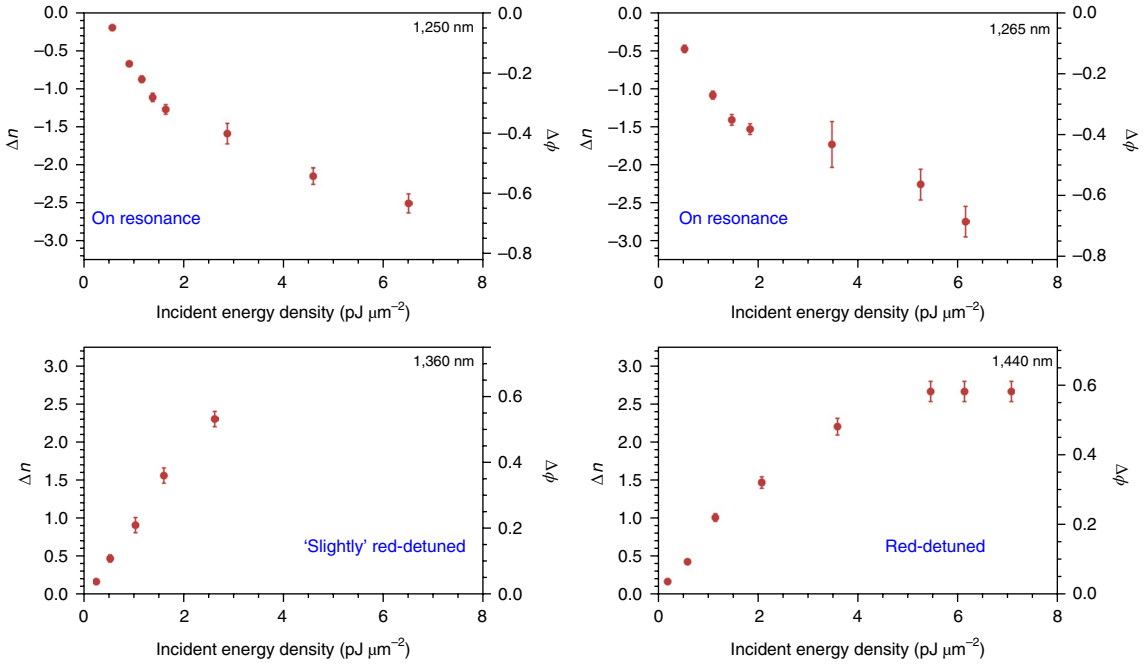

Fig. 3 | Maximum nonlinear contribution to the refractive index as a function of incident energy density. We determined the maximum nonlinear contribution to the refractive index by measuring the phase shifts at four different wavelengths for a series of different incident energy densities. Even at a highly red-detuned wavelength of 1,440 nm, the maximum nonlinear contribution to the refractive index is larger than 2.5. These results show that the metasurface exhibits a large refractive index change across a wide bandwidth. We note that the saturation effects present in the plots can be modelled to extract the effective fifth-order nonlinear coefficients. The error bars correspond to the uncertainty in measured values due to the distortion of the *Z*-scan traces.

magnitude and the signs of the nonlinear refractive index and the nonlinear absorption coefficient in any optical frequency of interest. The 50-nm-thick proof-of-concept metasurface exhibits a large broadband nonlinear response with sub-picosecond recovery time. The maximum absolute value of the nonlinear refractive index of the metasurface is three orders of magnitude larger than the bare, planar ITO at normal incidence[1]. As a benchmark comparison, it is also seven orders of magnitude larger than that of glass and four orders of magnitude larger than those of GaAs and As_2S_3 (ref. [42]). However, the large absorption in the coupled structure is a constraint. From the operational point of view, perhaps a more important criterion is the maximum achievable nonlinear phase shift over one absorption length. The maximum theoretical absorption in the structure (including the ohmic loss in metal) over the entire spectral range of interest is less than 40% (see Supplementary Section 'Field enhancement and absorption'). Further improvements to the design and material selection, such as dielectric nanoantennas and an ENZ material with less damping, may reduce the overall absorption while increasing the efficiency. More interestingly, the magnitude of the maximum nonlinear contribution to the refractive index (>2.5) is comparable to or larger than the linear refractive index of typical optical materials. Our findings introduce a new paradigm for developing efficient nonlinear media for applications involving low-power, high-integration-density nonlinear nanophotonic devices, and also demonstrate a subwavelength nonlinear metasurface for ultrafast all-optical control of the phase, amplitude and polarization of light.

Methods

Methods, including statements of data availability and any associated accession codes and references, are available at https://doi.org/10.1038/s41566-017-0089-9.

Received: 22 May 2017; Accepted: 20 December 2017;
Published online: 26 January 2018

References

1. Alam, M. Z., De Leon, I. & Boyd, R. W. Large optical nonlinearity of indium tin oxide in its epsilon-near-zero region. *Science* **352**, 795–797 (2016).
2. Miller, D. A. B. Are optical transistors the logical next step? *Nat. Photon.* **4**, 3–5 (2010).
3. Sherwood-Droz, N. et al. Optical 4×4 hitless silicon router for optical networks-on-chip (NoC). *Opt. Express* **16**, 15915–15922 (2008).
4. Boyd, R. W., Gehr, R. J., Fischer, G. L. & SipeJ. Nonlinear optical properties of nanocomposite materials. *J. Eur. Opt. Soc. A* **5**, 505–512 (1996).
5. Boyd, R. W. & Sipe, J. E. Nonlinear optical susceptibilities of layered composite materials. *J. Opt. Soc. Am. B* **11**, 297–303 (1994).
6. Sarychev, A. K. & Shalaev, V. M. Electromagnetic field fluctuations and optical nonlinearities in metal-dielectric composites. *Phys. Rep.* **335**, 275–371 (2000).
7. Abb, M., Albella, P., Aizpurua, J. & Muskens, O. L. All-optical control of a single plasmonic nanoantenna–ITO hybrid. *Nano Lett.* **11**, 2457–2463 (2011).
8. Abb, M., Wang, Y., de Groot, C. H. & Muskens, O. L. Hotspot-mediated ultrafast nonlinear control of multifrequency plasmonic nanoantennas. *Nat. Commun.* **5**, 4869 (2014).
9. Lee, J. et al. Giant nonlinear response from plasmonic metasurfaces coupled to intersubband transitions. *Nature* **511**, 65–69 (2014).
10. Yang, Y. et al. Nonlinear Fano-resonant dielectric metasurfaces. *Nano Lett.* **15**, 7388–7393 (2015).
11. Minovich, A. E. et al. Functional and nonlinear optical metasurfaces. *Laser Photon-. Rev.* **9**, 195–213 (2015).
12. Ren, M. et al. Nanostructured plasmonic medium for terahertz bandwidth all-optical switching. *Adv. Mater.* **23**, 5540–5544 (2011).
13. Liberal, I., Mahmoud, A. M., Li, Y., Edwards, B. & Engheta, N. Photonic doping of epsilon-near-zero media. *Science* **355**, 1058–1062 (2017).
14. Engheta, N. Pursuing near-zero response. *Science* **340**, 286–287 (2013).
15. Edwards, B., Alù, A., Young, M. E., Silveirinha, M. & Engheta, N. Experimental verification of epsilon-near-zero metamaterial coupling and energy squeezing using a microwave waveguide. *Phys. Rev. Lett.* **100**, 033903 (2008).
16. Alù, A., Silveirinha, M. G., Salandrino, A. & Engheta, N. Epsilon-near-zero metamaterials and electromagnetic sources: tailoring the radiation phase pattern. *Phys. Rev. B* **75**, 155410 (2007).
17. Silveirinha, M. & Engheta, N. Tunneling of electromagnetic energy through subwavelength channels and bends using ε-near-zero materials. *Phys. Rev. Lett.* **97**, 157403 (2006).

18. Caspani, L. et al. Enhanced nonlinear refractive index in ϵ-near-zero materials. *Phys. Rev. Lett.* **116**, 233901 (2016).
19. Neira, A. D. et al. Eliminating material constraints for nonlinearity with plasmonic metamaterials. *Nat. Commun.* **6**, 7757 (2015).
20. Capretti, A., Wang, Y., Engheta, N. & Dal Negro, L. Enhanced third-harmonic generation in Si-compatible epsilon-near-zero indium tin oxide nanolayers. *Opt. Lett.* **40**, 1500–1503 (2015).
21. Luk, T. S. et al. Enhanced third harmonic generation from the epsilon-near-zero modes of ultrathin films. *Appl. Phys. Lett.* **106**, 151103 (2015).
22. Yu, N. et al. Light propagation with phase discontinuities: generalized laws of reflection and refraction. *Science* **334**, 333–337 (2011).
23. Ni, X., Emani, N. K. Kildishev, A. V., Boltasseva, A. & Shalaev, V. M. Broadband light bending with plasmonic nanoantennas. *Science* **335**, 1214686 (2012).
24. Kildishev, A. V., Boltasseva, A. & Shalaev, V. M. Planar photonics with metasurfaces. *Science* **339**, 1232009 (2013).
25. Yu, N. & Capasso, F. Flat optics with designer metasurfaces. *Nat. Mater.* **13**, 139–150 (2014).
26. High, A. A. et al. Visible-frequency hyperbolic metasurface. *Nature* **522**, 192–196 (2015).
27. Lin, D., Fan, P., Hasman, E. & Brongersma, M. L. Dielectric gradient metasurface optical elements. *Science* **345**, 298–302 (2014).
28. Chong, K. E. et al. Polarization-independent silicon metadevices for efficient optical wavefront control. *Nano Lett.* **15**, 5369–5374 (2015).
29. Vassant, S. et al. Epsilon-near-zero mode for active optoelectronic devices. *Phys. Rev. Lett.* **109**, 237401 (2012).
30. Campione, S., Brener, I. & Marquier, F. Theory of epsilon-near-zero modes in ultrathin films. *Phys. Rev. B* **91**, 121408 (2015).
31. Campione, S., Wendt, J. R., Keeler, G. A. & Luk, T. S. Near-infrared strong coupling between metamaterials and epsilon-near-zero modes in degenerately doped semiconductor nanolayers. *ACS Photon-.* **3**, 293–297 (2016).
32. Schulz, S. A. et al. Optical response of dipole antennas on an epsilon-near-zero substrate. *Phys. Rev. A* **93**, 063846 (2016).
33. Sheik-Bahae, M., Said, A. A., Wei, T.-H., Hagan, D. J. & Van Stryland, E. W. Sensitive measurement of optical nonlinearities using a single beam. *IEEE J. Quantum Electron.* **26**, 760–769 (1990).
34. Luk, T. S. et al. Directional perfect absorption using deep subwavelength low-permittivity films. *Phys. Rev. B* **90**, 085411 (2014).
35. Khurgin, J. B., Sun, G., Chen, W. T., Tsai, W.-Y. & Tsai, D. P. Ultrafast thermal nonlinearity. *Sci. Rep.* **5**, 17899, https://doi.org/10.1038/srep17899 (2015).
36. Sachet, E. et al. Dysprosium-doped cadmium oxide as a gateway material for mid-infrared plasmonics. *Nat. Mater.* **14**, 414–420 (2015).
37. Kim, J. et al. Role of epsilon-near-zero substrates in the optical response of plasmonic antennas. *Optica* **3**, 339–346 (2016).
38. Hadad, Y., Sounas, D. & Alu, A. Space–time gradient metasurfaces. *Phys. Rev. B* **92**, 100304 (2015).
39. Yu, Z. & Fan, S. Complete optical isolation created by indirect interband photonic transitions. *Nat. Photon-.* **3**, 91–94 (2009).
40. Staude, I. et al. Tailoring directional scattering through magnetic and electric resonances in subwavelength silicon nanodisks. *ACS Nano* **7**, 7824–7832 (2013).
41. Kuznetsov, A. I., Miroshnichenko, A. E., Brongersma, M. L., Kivshar, Y. S. & Luk'yanchuk, B. Optically resonant dielectric nanostructures. *Science* **354**, aag2472 (2016).
42. Boyd, R. W. *Nonlinear Optics* (Academic Press, Cambridge, MA, 2003).
43. Campione, S., Kim, I., de Ceglia, D., Keeler, G. A. & Luk, T. S. Experimental verification of epsilon-near-zero plasmon polariton modes in degenerately doped semiconductor nanolayers. *Opt. Express* **24**, 18782–18789 (2016).
44. Liu, X. et al. Quantification and impact of nonparabolicity of the conduction band of indium tin oxide on its plasmonic properties. *Appl. Phys. Lett.* **105**, 181117 (2014).
45. Kane, E. O. Band structure of indium antimonide. *J. Phys. Chem. Solids* **1**, 249–261 (1957).

Acknowledgements

The authors acknowledge support from the Canada Excellence Research Chairs Program, the Natural Sciences and Engineering Research Council of Canada (NSERC), and the Canada Foundation for Innovation (CFI). I.D.L. acknowledges financial support from CONACyT (Ciencia Básica) grant no. 286150. M.Z.A. thanks S. Choudhary for discussions on the linewidth broadening mechanisms in a plasmonic system.

Author contributions

I.D.L. conceived the idea and initiated the study. I.D.L., S.A.S., M.Z.A. and J.U. designed the sample. S.A.S. performed the FDTD simulations. S.A.S. and J.U. fabricated the sample. M.Z.A. performed all experiments and the corresponding data analysis, developed the numerical model to describe the nonlinear response, and wrote the first draft. All authors contributed to finalizing the manuscript. I.D.L. and R.W.B. supervised the project.

Competing interests

R.W.B. is the co-founder and Chief Technology Officer of KBN Optics, Pittsford NY.

Additional information

Supplementary information is available for this paper at https://doi.org/10.1038/s41566-017-0089-9.

Reprints and permissions information is available at www.nature.com/reprints.

Correspondence and requests for materials should be addressed to I.D.

Publisher's note: Springer Nature remains neutral with regard to jurisdictional claims in published maps and institutional affiliations.

Methods

Design. We used a commercial finite-difference time-domain (FDTD) software (Lumerical FDTD solutions) to design the metasurface. The material dispersion was taken into account by using experimental values for the permittivity of ITO. The permittivity of the ITO film was measured using a spectroscopic ellipsometer. The antenna was designed by choosing the length-to-width ratio in such a way so that the fundamental dipole resonance of the antenna in the absence of the ITO film (that is, assuming only the glass substrate) lies near the zero crossing wavelength of the permittivity of the ITO film. The fabricated antennas had average dimensions of ~370 nm × 110 nm × 27 nm (the designed dimension was ~355 nm × 110 nm × 27 nm) and the unit cell dimension was 600 nm × 600 nm. The ITO film was 23 nm thick with a surface resistivity of ~80 Ω □$^{-1}$.

Fabrication. The 500 μm × 500 μm antenna array was fabricated on commercially available ITO on glass substrates (PGO GmbH). The antenna patterns were defined in a bilayer poly(methylmethacrylate) resist using electron beam lithography (Raith Pioneer 30 kV), followed by Au deposition and a liftoff step. Intraparticle proximity error correction was used to ensure sharp corners and a good rectangular shape of the antennas[46].

Measurements. The linear response of the metasurface was measured using a thermal light source and a custom-built transmittance measurement system. We used a single-beam *Z*-scan technique to measure the nonlinear response of the system using a regeneratively amplified femtosecond laser pumped optical parametric amplifier as the source laser. The pulse width was ~140 fs. A pair of apertures was used to produce a beam with a circularly symmetric trimmed Airy profile (that is, only the central lobe of an Airy pattern) in the far-field. A pair of achromatic doublet lenses was then used to collimate and enlarge the beam. Part of the collimated beam was routed to a reference photodiode to monitor power fluctuations. The rest of the collimated beam was focused onto the sample using an achromatic doublet lens with antireflection coating. The diffracted light after the sample was split using a pellicle beamsplitter, and routed to a pair of detectors for closed- and open-aperture measurements. The sample was mounted on a computer-controlled motorized translation stage. For each position of the sample we recorded truncated mean values (the lowest 25% and highest 25% values were discarded before calculating the mean) from the photodiodes averaged over ~3,000 pulses. Due to the diffractive propagation required to produce a collimated beam with an Airy profile, the beam diameter at the *Z*-scan lens varied as a function of wavelength. Specifically, the input beam diameter varied from 10.2 ± 0.15 mm to 14.65 ± 0.15 mm for $\lambda = 1{,}160$ nm to $\lambda = 1{,}560$ nm. The beam was focused onto the sample using an antireflection-coated achromatic doublet lens of ~100 mm focal length. The closed-aperture detector was placed 285 mm away from the *Z*-scan lens. We did not use any aperture before the closed-aperture detector because the active area (5 mm diameter) of the detector was much smaller than the beam diameter. The use of an even smaller aperture adversely affected the measurement by reducing the signal-to-noise ratio.

We used the Fresnel–Kirchhoff diffraction integral with a fast-Fourier-transform-based beam propagation method to simulate the experimental beam propagation over the entire set-up. We were thus able to calculate the *z*-dependence of the light falling onto the closed- and open-aperture photodiodes. We wrote the numerical beam propagation program using Julia language[47], which allows arbitrary order nonlinear refraction and absorption to be taken into account. We have observed that at high intensity fifth-order nonlinear absorption becomes significant, and at non-resonant wavelengths it can almost completely cancel the third-order nonlinear absorption.

Numerical model of the nonlinear refractive index. To calculate the nonlinear refractive index, we carried out a series of linear FDTD simulations of the antenna–ITO structure by varying the plasma frequency of the ITO. We then calculated the homogenized refractive index from each set of *s*-parameters, resulting in a plasma frequency-dependent effective index distribution of the coupled system. We then calculated the time-dependent electronic temperature using a semiclassical two-temperature model. The plasma frequency of the ITO layer was calculated based on the electronic temperature (see Supplementary Section 'Two-temperature model'). Based on the calculated plasma frequency and the set of homogenized refractive indices, we calculated the time-dependent change in the refractive index. The effective nonlinear coefficients n_2 and β were determined by dividing the time-averaged homogenized refractive index (normalized by the pulse shape) by the incident intensity. In this model, we ignore the intrinsic nonlinearity of the metal and the change in absorption of the coupled system due to the temperature-dependent change in the damping coefficient (imaginary part of the permittivity) of the ITO layer. This leads to an overestimation of β obtained from the numerical model for all wavelengths far from the saturation intensity. Hence, we scaled down the β values by a factor of 3.0 to fit the numerical result to that obtained in the experiment.

Code availability. All relevant code used in this paper are available from the corresponding author upon reasonable request.

Data availability. All relevant data used in this paper are available from the corresponding author upon reasonable request.

References

46. Schulz, S. A. et al. Quantifying the impact of proximity error correction on plasmonic metasurfaces [invited]. *Opt. Mater. Express* **5**, 2798–2803 (2015).
47. Bezanson, J., Edelman, A., Karpinski, S. & Shah, V. B. Julia: a fresh approach to numerical computing. *SIAM Rev.* **59**, 65–98 (2017).

nature photonics

SUPPLEMENTARY INFORMATION

https://doi.org/10.1038/s41566-017-0089-9

In the format provided by the authors and unedited.

Large optical nonlinearity of nanoantennas coupled to an epsilon-near-zero material

M. Zahirul Alam[1], Sebastian A. Schulz[1,2,3], Jeremy Upham[1], Israel De Leon[4*] and Robert W. Boyd[1,5]

[1]Department of Physics, University of Ottawa, Ottawa, ON, Canada. [2]Centre for Advanced Photonics and Process Analysis, Cork Institute of Technology, Cork, Ireland. [3]Tyndall National Institute, Cork, Ireland. [4]School of Engineering and Sciences, Tecnologico de Monterrey, Monterrey, NL, Mexico. [5]Institute of Optics and Department of Physics and Astronomy, University of Rochester, Rochester, NY, USA. *e-mail: ideleon@itesm.mx

Linear response of ITO

We measured the permittivity of the 23 nm ITO using ellipsometry (Fig.S1). For the entire spectral range the following Drude-Loretz model can quantify the permittivity:

$$\varepsilon = \varepsilon_\infty + \frac{(\varepsilon_s - \varepsilon_\infty)\omega_t^2}{\omega_t^2 - \omega^2 - i\Gamma_0\omega} - \frac{\omega_p^2}{\omega^2 + i\Gamma_d\omega}. \tag{1}$$

We use the following values for the parameters. $\varepsilon_\infty = 3.1178$, $\varepsilon_s = 3.8466980$, $\omega_t = 7.42969 \times 10^{15}$ rad/sec, $\omega_p = 2.6594 \times 10^{15}$ rad/sec, $\Gamma_0 = 0.534217 \times 10^{15}$ rad/sec, $\Gamma_d = 0.231806 \times 10^{15}$ rad/sec.

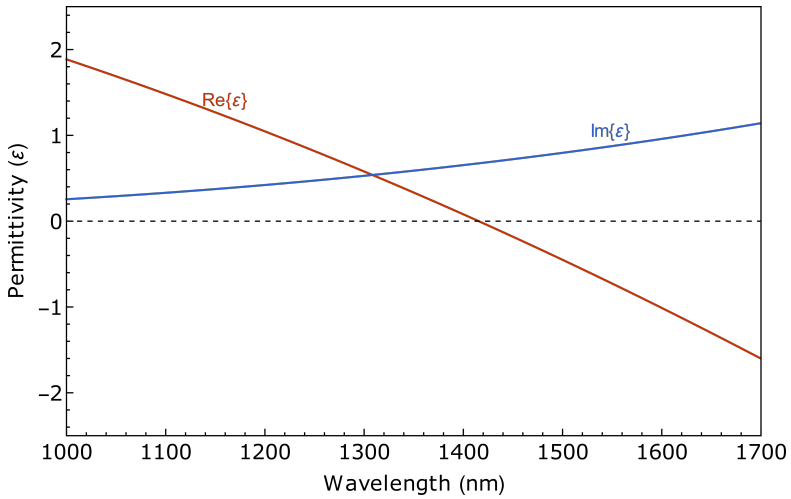

Figure S1. Permittivity of ITO: The real part of permittivity of the low conductivity ITO crosses zero at 1420 nm.

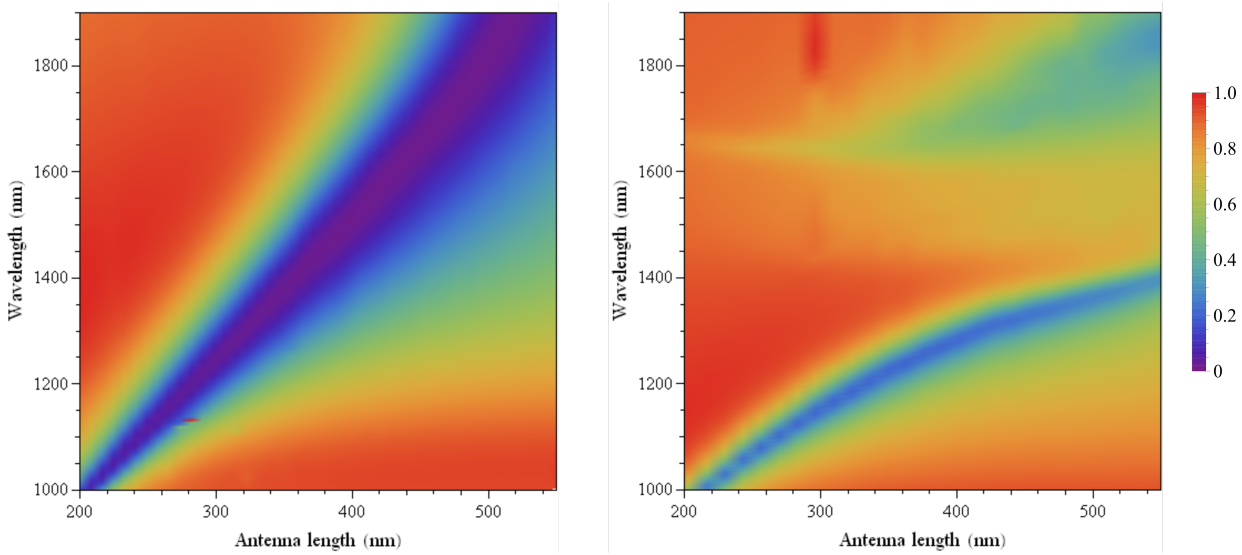

Figure S2. Strong coupling: Length dependent variation in the transmittance of gold dipole antenna on glass in the absence of an ITO layer (left panel) and with an ITO layer between the antenna and the substrate (right panel).

Linear response of the coupled system

A thin ENZ layer supports a bulk plasma mode with wavevector-dependent radiative and nonradiative properties at the zero permittivity wavelength. This mode has been theoratically and experimentally investigated in a number of papers.[1,2] When a

dipole antenna with resonance near the bulk plasma mode is placed on the ITO layer, the antenna mode and the bulk plasma mode interacts. This interaction results in strong coupling induced splitting of the antenna resonance. Fig. S2 shows an anti-crossing in the coupled structure which is a signature that antenna-ITO is in strong coupling regime. This artificial polariton splitting ($\sim \lambda/4$) is one of the largest observed in metamaterials.[3–5] The shape and the magnitude of the resonance dips of the ITO-antenna coupled structure depend on the coupling strength and the material parameters. The spectral width of the resonance of the coupled system at the shorter wavelength is narrower than that of antenna only.

Electronic dispersion relation in ITO

ITO has a non-parabolic conduction band.[6] Following Kane's model[7,8] of semiconductor we can write the energy-wavevector (E, k) dispersion relation for a conduction band electron of ITO as

$$\frac{\hbar^2 k^2}{2m} = E + CE^2, \tag{2}$$

where $C = 0.4191\ \text{eV}^{-1}$ is the non-parabolicity parameter and we have used the value reported by Liu et. al.[6] $m = 0.4m_e$ is the effective mass of the electrons. From the above relation we find

$$k = \sqrt{2mE(1+CE)/\hbar^2}, \tag{3}$$

$$dk = \sqrt{\frac{2m}{\hbar^2}}\frac{1+2CE}{2\sqrt{E+CE^2}}dE. \tag{4}$$

The number of states available for a given magnitude of wavevector $|k|$ can be found by constructing a spherical shell of radius $|k|$ and thickness dk. The volume of this spherical shell in the momentum space is $4\pi k^2 dk$. The number of k states within the spherical shell, $g(k)dk$, is

$$g(k)dk = \frac{1}{2^3} \times 2 \times 4\pi k^2 \frac{V}{\pi^3} dk. \tag{5}$$

The factor 2 is the spin degeneracy factor of electrons. The factor $1/2^3$ is to avoid counting indistinguishable wavefunctions differing in signs only. Now by using Eqns. (3) and (4) and by dividing by the volume V, we can find the density of states $g(E)$, defined as the number of electron states in the conduction band per unit volume over an energy range dE,

$$g(E) = \frac{\sqrt{2}}{\pi^2}\left(\frac{m}{\hbar^2}\right)^{\frac{3}{2}} [(1+CE)]^{\frac{1}{2}} (1+2CE) \tag{6}$$

The total number of electrons n can be found by integrating the product of the Fermi-Dirac distribution function (f_{FD}) and the density of states over all energy range

$$n = \int_0^\infty f_{FD}(E, \mu(T_e), T_e) g(E) dE, \tag{7}$$

where $\mu(T_e)$ is the electro-chemical potential which depends on the electron temperature T_e due to the conservation of total electron number in the conduction band. Thus, the electron number conservation requirement results in decreasing value of the chemical potential with increasing electron temperature.

We can write the plasma frequency as[9,10]

$$\omega_p^2(T_e) = \frac{e^2}{3m\varepsilon_0\pi^2} \int_0^\infty dE(1+2CE)^{-1} \left(\frac{2m}{\hbar^2}(E+CE^2)\right)^{\frac{3}{2}} \left(-\frac{\partial f_{FD}(E, \mu(T_e), T_e)}{\partial E}\right). \tag{8}$$

The expression $\left(-\frac{\partial f_{FD}}{\partial E}\right)$ is a measure of the strength of the thermal broadening of the electronic distribution around the Fermi level. For electrons in a room temperature solid the thermal broadening function is narrow and is zero beyond a few $k_B T$ from the Fermi level. However, an elevated electron temperature leads to the broadening of this function due to a strong modification of the Fermi-Dirac distribution. The modification of the Fermi-Dirac distribution is much stronger in ITO than a noble metal due to the lower heat capacity constant of the free electrons of ITO. This results in an electron-temperature-dependent plasma frequency of ITO due to the temperature dependence of the electro-chemical potential (the effective mass of the electrons) as required by Eq.(7). For a given electronic temperature we find the chemical potential from Eqn. (7), and use Eqn. (8) to find the plasma frequency of ITO which we insert into the Drude-Lorentz model of ITO to calculate the permittivity of ITO at an elevated electron temperature. For a parabolic band ($C = 0$) the above expression reduces to the well known expression of the plasma frequency.[10]

Two-temperature model

The free-electron dynamics in ITO are metal-like and can be described by the Drude model. The third-order self-focusing nonlinearity of ITO in the ENZ regime is dominated by the response of the free-electrons. To describe this nonlinear mechanism, we use a phenomenological two-temperature model.[11–13] The nonlinear process due to the hot-electron dynamics has a finite response time and the maximum response is delayed with respect to the peak of the laser excitation. In noble metals the total relaxation time of the hot electrons is a few picoseconds and is limited by the electron-phonon interaction time. However the response of the ITO thin film deviates from that of the metal in three important ways: i) unlike noble metals, ITO has no interband transition resonance in the visible or infrared range of the optical spectrum; ii) the free-electron density in ITO is almost two orders of magnitude smaller than that of noble metals such as gold, resulting in much smaller electron heat capacity and larger change in the electron temperature if all other parameters are held constant; and iii) owing to a relatively smaller free-electron density, the Fermi level is quite low in the conduction band (~ 1 eV for ITO). Due to the last property, infrared radiation at ENZ wavelengths can excite even the lowest-energy conduction band electrons (in contrast, the Fermi level of gold is ~ 6.42 eV and IR light only excite only those electrons that sit near the Fermi level).

According to the delayed two-temperature model, after the laser pulse is absorbed, the generated hot electrons acquire a non-thermal energy distribution and act as a delayed source of energy. The overall dynamics of the conduction band electrons can be described by the following system of phenomenological coupled differential equations:[13]

$$\begin{aligned} C_e\frac{\partial T_e(t)}{\partial t} &= -g_{ep}(T_e(t)-T_l(t))+\frac{N_{th}(t)}{2\tau_{ee}(t)}, \\ C_l\frac{\partial T_l}{\partial t} &= g_{ep}(T_e(t)-T_l(t))+\frac{N_{th}}{\tau_{ep}(t)}, \\ \frac{\partial N(t)}{\partial t} &= -\frac{N(t)}{2\tau_{ee}(t)}-\frac{N(t)}{\tau_{ep}(t)}+P, \end{aligned} \tag{9}$$

Here, N is the non-thermal energy density stored in the excited electrons, g_{ep} is the electron-phonon coupling coefficient, T_e (T_l) is the free-electron (lattice) temperature, C_e (C_l) is the heat capacity of the electrons (lattice), τ_{ee} (τ_{ep}) is the electron-electron (electron-phonon) relaxation time, and P is the time dependent absorbed power density (i.e., rate of energy density absorbed in the material). We have ignored thermal diffusion processes in Eq. (9). In the transverse dimension the beam size greatly exceeds the electrons thermal diffusion length and hence we also ignore the transverse dependence. We have also ignored the thermal diffusion in the longitudinal direction by assuming constant absorbed energy density due to small thickness of the ITO film.

Next we estimate the different parameters for ITO that appear in Eq. (9). We calculate the electron heat capacity C_e by using[14]

$$C_e(T_e)=\int Eg(E)\frac{\partial f_{FD}(\mu(T_e),T_e)}{\partial T_e}dE \tag{10}$$

We take the lattice heat capacity $C_l = 2.54\times10^6$ Jm^{-3}K to be a constant due to relatively small change in the lattice temperature.[15]

The electron-electron scattering rate ($\Gamma_{ee}=1/\tau_{ee}$) determines the time duration electrons require to reach to thermal equilibrium with each other. We use the following relation to estimate the temperature dependent electron-electron scattering rate[16]

$$\Gamma_{ee}=\frac{\omega^2}{4\pi^2\omega_p(T_e)}\left[1+\left(\frac{2\pi k_B T_e}{\hbar\omega}\right)^2\right] \tag{11}$$

The electron-phonon scattering rate (Γ_{eph}) depends on the lattice temperature and the Debye temperature of the lattice ($\Theta_D = 900K$)

$$\Gamma_{eph}=\Gamma_0\left[\frac{2}{5}+\frac{4T_L^5}{\Theta_D^5}\int_0^{\theta_D/T_l}\frac{z^4}{e^z-1}dz\right]. \tag{12}$$

The electron-phonon coupling coefficient (g_{ep}) determines the rate of the energy exchange between the excited hot electrons and the vibrational modes of the lattice. Due to the strong modification of the conduction band electron distribution, even the electrons with initial energy much below the Fermi level take part in this energy exchange process. Hence we estimate the electron-phonon coupling coefficient using a relation which includes the density of states of the conduction band[14]

$$g_{ep}=\frac{\pi k_B}{\hbar g(E_F)}\lambda_{ep}<(\hbar\omega_{ph})^2>\int g^2(E)\frac{-\partial f_{FD}}{\partial E}dE, \tag{13}$$

where λ_{ep} is the electron-phonon mass enhancement parameter and the second moment of phonon spectrum $< (\hbar\omega_{ph})^2 >$ is an empirical parameter. We take $\lambda_{ep} < (\hbar\omega_{ph})^2 >= 0.0042\ eV^2$ are a few times smaller than nobel metals such as gold.[14]

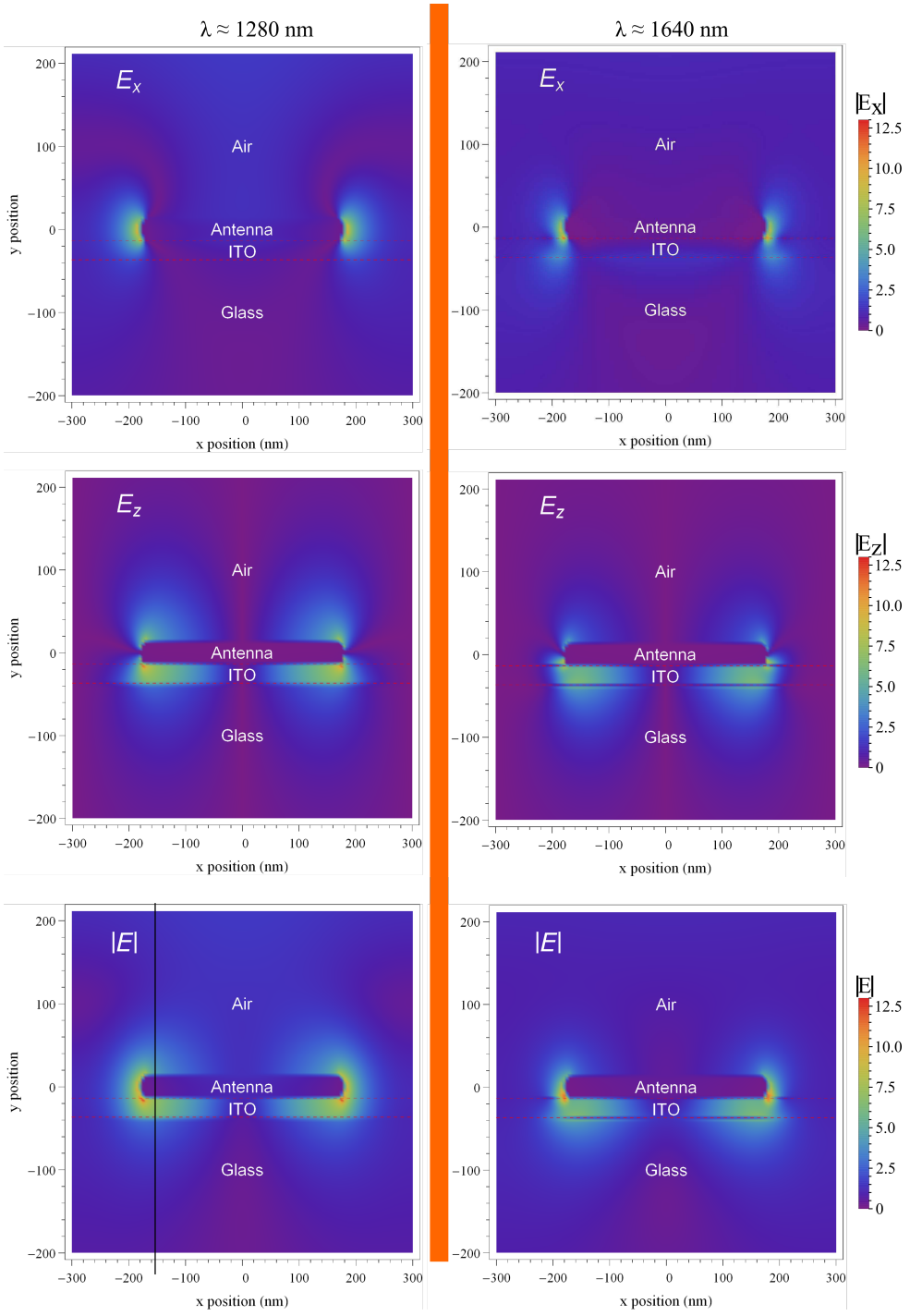

Figure S3. Field distribution: The plots show the field distribution at two resonances ($\lambda \approx 1280$ nm and $\lambda \approx 1640$ nm). The left panel shows the field distribution of the resonance at the short wavelength (the resonace of interest for this report). The right panel shows the field distribution at the resonance located at the long wavelength (we have not investigated the response at this wavelength). The z-components of the electric field profile shows the main difference between the two modes of the coupled structure. The edges of the antennas are rounded with a rounding radius of 7 nm. We plot the wavelength-dependent intensity enhancement along the vertical black line in the next figure.

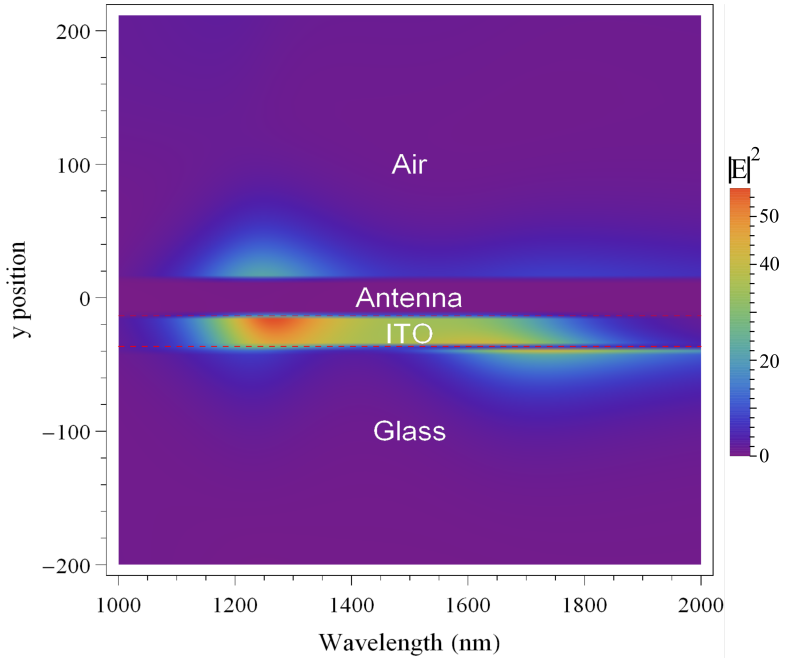

Figure S4. Wavelength-dependent intensity enhancement: Shown inside the ITO layer of the coupled structure, for a fixed x-position – along the vertical black line in Fig. S3 – when excited from air.

Field enhancement and absorption

The antennas placed on the ITO film allow electric field to be concentrated inside the ITO structure resulting in enhancement of the field intensity. Figure S4 shows the calculated intensity enhancement factor, as a function of position and wavelength, sufficiently far from the antenna edge to avoid hotspots. The fabricated dipole antennas differ from the simulated ones due to the fabrication imperfection which results in antenna edges being rounded off. We took this into account in the simulation by rounding the edges (7 nm rounding radius) of the antennas. Furthermore, in our calculation of the two-temperature model we take the calculated intensity enhancement (averaged over the ITO thickness) by considering the electric field enhancement sufficiently far away from the antenna edge (along the vertical black line in the lower left panel of Fig. S3).

The absorption spectrum of the coupled system also differs significantly from the absorption coefficient of the bare ITO (Fig. S5). Due to the stronger interaction of light with the ITO and the loss introduced by the plasmonic antennas, the absorption coefficient is higher close to the resonances of the coupled system (maximum absorption is $\sim 30\%$ within the spectral range of interest in this paper). Thus the antenna array increases the absorbed power density in the ITO film which results in the enhancement of the nonlinear response of the overall system. However, a significant fraction of the power is absorbed by the antennas which can be reduced by using dielectric antennas.

Nonlinear response of ITO

We measured the nonlinear response of the 23-nm-thick ITO sample use a Z-scan technique at normal incidence. The 23-nm-thick ITO film exhibits wavelength dependent positive nonlinear refraction and saturable absorption. The maximum value of n_2 is $\sim 1.5 \times 10^{-3}$ at $\lambda = 1400$ nm with ~ 200 GW/cm^2 incident intensity. Thus ~ 200 GW/cm^2 of incident intensity induces a change of 0.15. It can be explained, to first approximation, due to a 5% red-shift in the plasma frequency. In order to find the nonlinear response of the ITO film, we measured the nonlinear response of the ITO coated substrate (float glass) and the nonlinear response of a similar substrate seperately while keeping the incident intensity constant. We then used the relation $n_{2,\mathrm{ITO}} = (n_{2,\mathrm{ITO-with-substrate}} L_{\mathrm{ITO-with-substrate}} - n_{2,\mathrm{substrate}} L_{\mathrm{substrate}})/L_{\mathrm{ITO}}$ to find the n_2 of the ITO layer. Here, L denotes the thickness.

Refractive index homogenization

The effective linear refractive index of the medium depends on the Q-factor of the resonator and the coupling dynamics between the antennas and the ENZ film. We used the metamaterial homogenization procedure introduced by Smith et al.[17] to calculate the effective refractive index of the hybrid structure. We use the following set of equations to find both the real and the imaginary

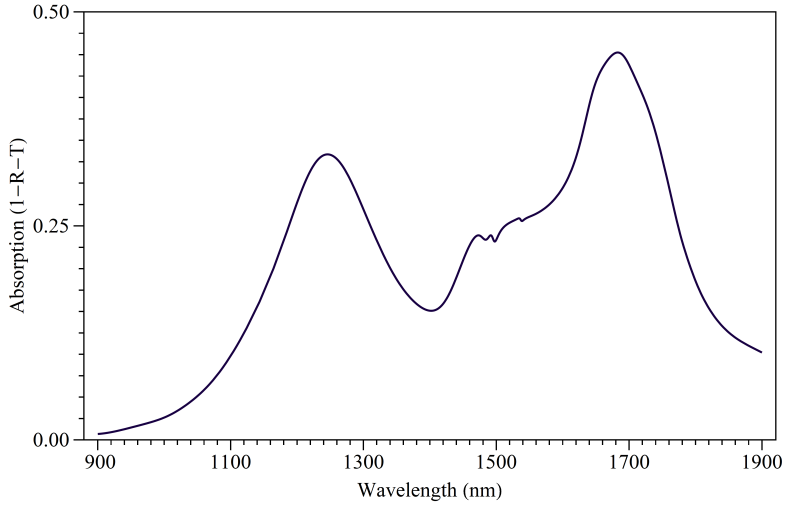

Figure S5. Absorption: Calculated absorption profile by the ITO-antenna coupled structure. The two peaks in the profile - one at a shorter wavelength than the zero-crossing wavelength and one at a larger wavelength - further confirms the strong coupling dynamics between ENZ mode and the antenna mode. Within the spectral range of interest the the theoratical maximum absorption is $\sim 34\%$.

part of the homogenized effective linear refractive index (Figure S7)

$$
\begin{aligned}
s_{av} &= \sqrt{s_{11}s_{22}} \\
z &= \sqrt{\frac{(1+s_{av}^2-s_{21}^2)}{(1-s_{av})^2-s_{21}^2}} \\
n_{eff} &= \frac{\imath}{2\pi d_{ITO}/\lambda}\log\left[\frac{s_{21}}{1-s_{av}\frac{z-1}{z+1}}\right]
\end{aligned}
\tag{14}
$$

We calculated the plasma-frequency-dependent homogenized refractive index by calculating the s-parameters using a series of FDTD simulations while manually varrying the zero permittivity wavelength of the ITO film. The two-temperature model and the plasma-frequency-dependent homogenized refractive index of the overall system allows us to calculate the nonlinear refractive index of the antenna-ITO coupled system.

Change in plasma frequency and nonlinear index

To first approximation the change in the refractive index of ITO and that of the coupled system can be attributed to the red-shift of the plasma frequency as a function of incident intensity.[9,10,18,19] For example, a 5% change in the plasma frequency ($\Delta\omega_p = 5\%$) leads to a change in the refractive index of the bare ITO layer by ~ 0.16 at $\lambda = 1400$ nm which can be achieved with incident intensity of 100 GW/cm^2. Whereas, for the coupled system a red-shift of the plasma frequency leads to a much larger change in the refractive index. Depending on which spectral side of the resonance is under investigation, the change in the refractive index, Δn, can be either positive or negative. For example, in the coupled system $\Delta\omega_p = 5\%$ leads $\Delta n = -5$ and $\Delta n = 1.16$ at $\lambda = 1280$ nm and $\lambda = 1440$ nm respectively (Fig. S8). However, experimentally we measure $\Delta n_{\max} \approx -2.5$ at 1280 nm and $\Delta n_{\max} \approx 2.5$ at $\lambda = 1440$ nm. Thus, this simple analysis based on the red-shift of the plasma frequency overestimates the $\Delta n_{\max}$ on- and near- resonance but underestimates the changes far from the resonance. The change in the electronic temperature not only red-shifts the plasma frequency of the ITO but also increases the damping coefficent, i.e. the imaginary part of the permittivity. As a result, the resonance width of the coupled system broadens in addition to the red-shift of the resoance due to the change in ω_p as a function of the incident intensity. A broadened resonace of the coupled system reduces $\Delta n_{\max}$ at on- or near-resonance wavelengths and enhances $\Delta n_{\max}$ at far from resonance. The presence of the antennas thus amplify the change in the refractive index by upto a factor of 20. Moreover, the presence of the antenna introduces an intensity enhancement of at least a factor of ~ 50 at normal incidence (Fig. S4). Thus, even at the saturation intensities these two effects combined can explain a factor of 1000 enhancement of the value of n_2 of the coupled structure compared to that of the the bare ITO at $\lambda = 1400$ nm.

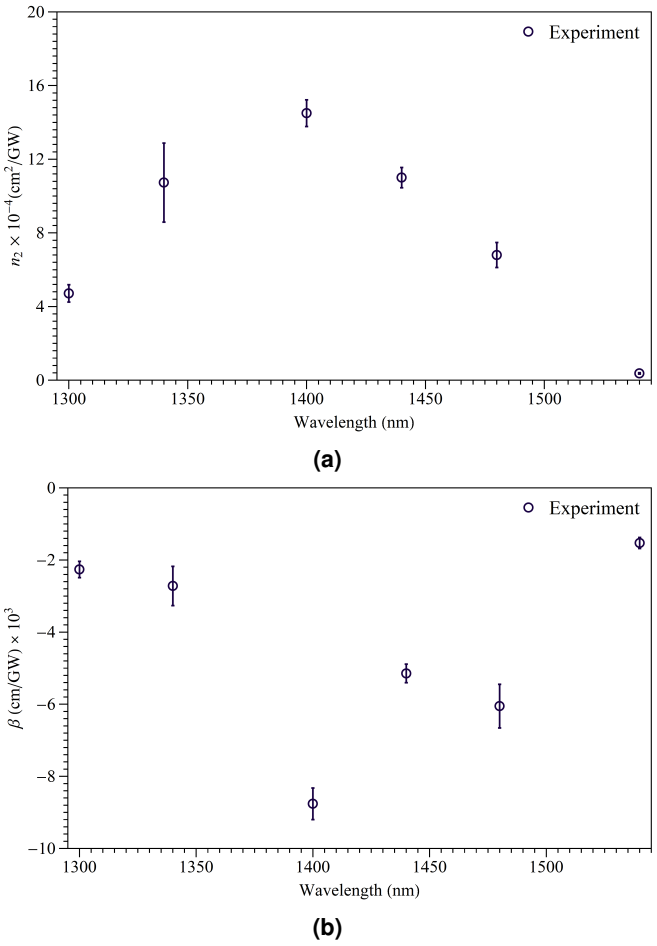

Figure S6. Measured nonlinear response of low conductivity ITO: (a) The effective nonlinear refractive index n_2 as measured using Z-scan. We use a 23-nm-thick ITO, which is used as the ENZ layer in the coupled structure, for this measurement. (b) The nonlinear absorption coefficient β.

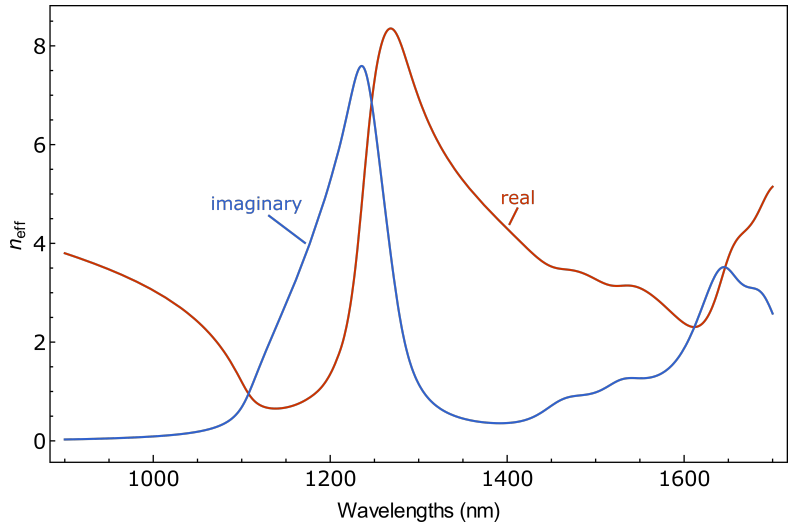

Figure S7. Homogenized refractive index: We used a refractive index homogenization technique to obtain the effective index of the antenna-ITO coupled system. The large effective nonlinear response can understood as the light induced time-dependent shift and reshaping of the homogenized linear dispersion of the coupled system.

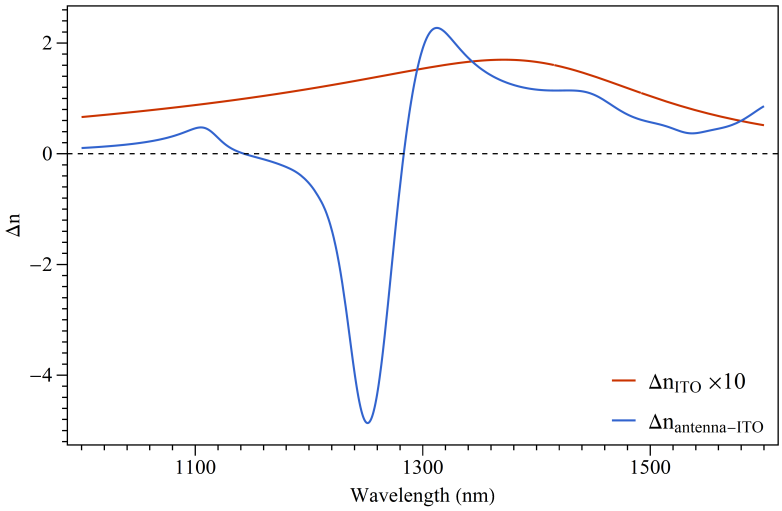

Figure S8. Change in the refractive index due to a red-shift of the plasma frequency: The plot shows that due to the presence of the antenna, a 5% change in the plasma frequency can lead to a much larger change in the refractive index in the coupled structure compared to the bare ITO. Moreover, the required incident intensity to induce a constant amount of red-shift in the plasma frequency is much smaller in the coupled structure than the bare ITO due to the field enhancement. Here, we calculate the change in the refractive index Δn simply by subtracting $\sqrt{\varepsilon(\omega_p)}$ from $\sqrt{\varepsilon(0.95\omega_p)}$. In order to calculate the refractive index for a particular plasma frequency, we use the Lorentz-Drude model and the homogenized refractive index for the bare ITO and the coupled system respectively.

Z-scan traces

We show representative Z-scan traces in the presence of large nonlinear absorption in Fig. S9a ($\lambda = 1340$nm). To obtain the nonlinear measurements, we use a pellicle beam splitter placed right after the sample to divide the beam in order to simulatenously measure closed- and open-aperture signals. We also use a reference photodiode to monitor the power fluctuation. We do two sets of measurements for each wavelength in order to calculate n_2 and β values: one set of measurements with the incident intensity low enough so that nonlinear response is absent; and the other set with an incident intensity large enough ($\sim 150\text{MW}/\text{cm}^2$) to induce a nonlinear response. We normalize the open-aperture signal by dividing the high intensity signal (normalized by the reference signal to account for the power fluctuation) by the low intensity signal (normalized by the reference signal to account for the power fluctuation). In order to find the value of the imaginary part of the phase shift we fit the normalized data to curves generated numerically, as described in the method section. For the closed-aperture signal we find the best fit after dividing the closed-aperture data by the open-aperture data. Finally, we calculate the n_2 and β values from the phase shifts using the standard equations.[20]

We perform a series of measurements with varying intensity to find the maximum possible phase shift – and the change in the refractive index – as shown in Fig. 3. We observed that for a sufficiently large incident intensities the fifth-order nonlinear effects can become important (Fig. S9b). This is the case for some of the data points in Fig. 3. In such cases, we do not divide the closed-aperture signal with the open-aperture signal in order to decouple the nonlinear refraction from the nonlinear absorption. Instead, we find the real part of the nonlinear phase shift by finding the best fit lines while taking the third- and fifth-order nonlinear absorptions into account (Fig. S9b). The phase shifts obtained with such large intensities were used to find the maximum intensity-dependent change in the refractive index (Δn) shown in Fig. 3 of the main text. The values of n_2 and β were obtained using a much lower input intensity, as mentioned above.

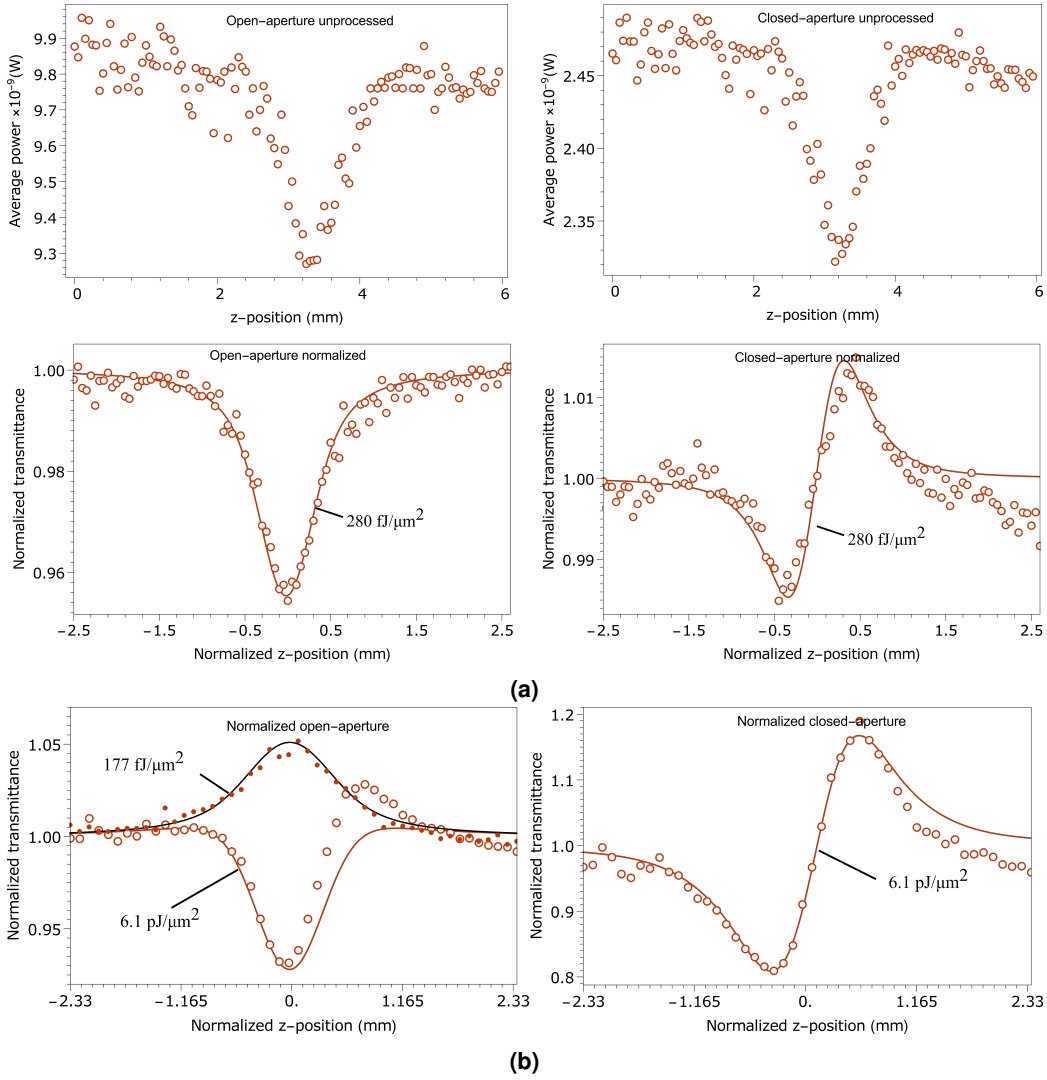

Figure S9. Z-scan traces: (a) Unprocessed (top panel) and processed data (bottom panel) for Z-scan signals at $\lambda = 1340$ nm for incident intensity of ~ 158 MW/cm^2. We obtained the normalized closed-aperture signal after dividing the closed-aperture signal with the open-aperture signal. We obtain the nonlinear phase shifts values - real phase shift = 0.055 rad and imaginary phase shift = 0.043 rad - by fitting the data with the numerically obtained curves (solid lines). (b) Normalized open- and closed-aperture signal at $\lambda = 1440$ nm for real phase shift of ~ 0.57 rad which is equivalent to $\Delta n = 2.61$. In this case, both third- and fifth-order nonlinear absorptions are important. In order to extract the phase shift from the z-scan traces, it is necessary to normalize the signal in such a way so that the transmittance far from focus approaches 1.0.

Reference	$\lvert n_2 \rvert$(cm^2/GW)	λ(nm)
ITO ($R_s = 70-100$ Ω/sq.)[18]	4.0×10^{-5}	1000
ITO ($R_s = 8-12$ Ω/sq.)[18]	1.6×10^{-3}	1000
Dimer antenna-ITO[18]	5.9×10^{-2}	1000
ITO ($R_s = 4.5$ Ω/sq.)[19]	2.6×10^{-3}	1240
ITO ($R_s = 80$ Ω/sq.) (this work)	1.5×10^{-3}	1400
Dipole antenna-ITO (this work)	3.73	1240

Supplementary Table 1. Comparison of nonlinear response of ITO and hybrid ITO-antenna system at normal incidence.

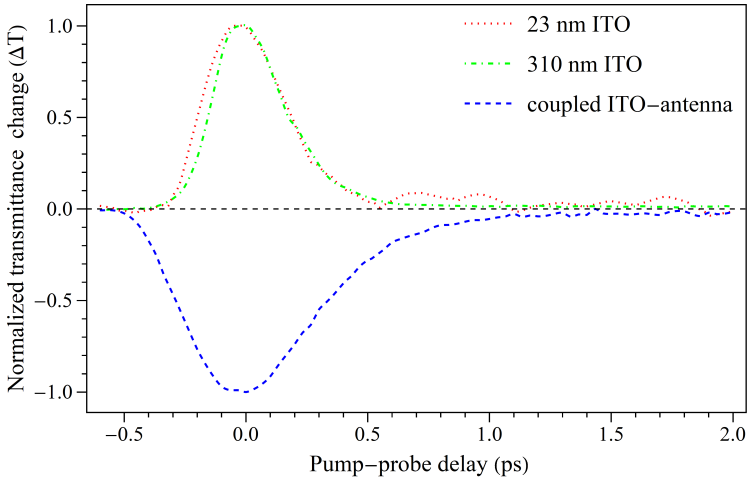

Figure S10. Response time: Normalized pump-probe transmittance of 23 nm thin ITO, 310 nm thick ITO and ITO-antenna coupled system at 1300 nm wavelength. The Pump-probe response time for the coupled system is longer than that of the thin (low conductivity) or thick (high conductivity) ITO films. We normalized the x-axis such that the zero pump-probe delay time corresponds to the maximum transmittance for visual aid.

References

1. Campione, S., Kim, I., de Ceglia, D., Keeler, G. A. & Luk, T. S. Experimental verification of epsilon-near-zero plasmon polariton modes in degenerately doped semiconductor nanolayers. *Optics Express* **24**, 18782–18789 (2016).
2. Campione, S., Brener, I. & Marquier, F. Theory of epsilon-near-zero modes in ultrathin films. *Phys. Rev. B* **91**, 121408 (2015).
3. Schulz, S. A. *et al.* Optical response of dipole antennas on an epsilon-near-zero substrate. *Physical Review A* **93**, 063846 (2016).
4. Campione, S., Wendt, J. R., Keeler, G. A. & Luk, T. S. Near-infrared strong coupling between metamaterials and epsilon-near-zero modes in degenerately doped semiconductor nanolayers. *ACS Photonics* **3**, 293–297 (2016).
5. Vassant, S. *et al.* Epsilon-near-zero mode for active optoelectronic devices. *Physical review letters* **109**, 237401 (2012).
6. Liu, X. *et al.* Quantification and impact of nonparabolicity of the conduction band of indium tin oxide on its plasmonic properties. *Applied Physics Letters* **105**, 181117 (2014).
7. Kane, E. O. Band structure of indium antimonide. *Journal of Physics and Chemistry of Solids* **1**, 249–261 (1957).
8. Chakravarti, A. & Nag, B. Generalized einstein relation for degenerate semiconductors having non-parabolic energy bands. *International Journal of Electronics Theoretical and Experimental* **37**, 281–284 (1974).
9. Guo, P., Schaller, R. D., Ketterson, J. B. & Chang, R. P. H. Ultrafast switching of tunable infrared plasmons in indium tin oxide nanorod arrays with large absolute amplitude. *Nature Photonics* **10**, 267–273 (2016).
10. Guo, P. *et al.* Large optical nonlinearity of ito nanorods for sub-picosecond all-optical modulation of the full-visible spectrum. *Nature Communications* **7**, 12892 (2016).
11. Brorson, S., Fujimoto, J. & Ippen, E. Femtosecond electronic heat-transport dynamics in thin gold films. *Physical Review Letters* **59**, 1962 (1987).
12. Sun, C.-K., Vallee, F., Acioli, L., Ippen, E. & Fujimoto, J. Femtosecond investigation of electron thermalization in gold. *Physical Review B* **48**, 12365 (1993).
13. Carpene, E. Ultrafast laser irradiation of metals: Beyond the two-temperature model. *Physical Review B* **74**, 024301 (2006).
14. Lin, Z., Zhigilei, L. V. & Celli, V. Electron-phonon coupling and electron heat capacity of metals under conditions of strong electron-phonon nonequilibrium. *Physical Review B* **77**, 075133 (2008).
15. Yagi, T. *et al.* Analysis on thermal properties of tin doped indium oxide films by picosecond thermoreflectance measurement. *Journal of Vacuum Science & Technology A* **23**, 1180–1186 (2005).

16. Voisin, C., Fatti, N. D., Christofilos, D. & Vallée, F. Ultrafast electron dynamics and optical nonlinearities in metal nanoparticles. *The Journal of Physical Chemistry B* **105**, 2264–2280 (2001).

17. Smith, D. R., Schultz, S., Markoš, P. & Soukoulis, C. Determination of effective permittivity and permeability of metamaterials from reflection and transmission coefficients. *Physical Review B* **65**, 195104 (2002).

18. Abb, M., Albella, P., Aizpurua, J. & Muskens, O. L. All-optical control of a single plasmonic nanoantenna–ito hybrid. *Nano letters* **11**, 2457–2463 (2011).

19. Alam, M. Z., De Leon, I. & Boyd, R. W. Large optical nonlinearity of indium tin oxide in its epsilon-near-zero region. *Science* **352**, 795–797 (2016).

20. Sheik-Bahae, M., Said, A. A., Wei, T.-H., Hagan, D. J. & Van Stryland, E. W. Sensitive measurement of optical nonlinearities using a single beam. *IEEE Journal of Quantum Electronics* **26**, 760–769 (1990).

5 BEYOND THE PERTURBATIVE DESCRIPTION OF THE NONLINEAR OPTICAL RESPONSE OF LOW-INDEX MATERIALS

CONTRIBUTION STATEMENT:

I performed the laboratory measurements for this project, helped in developing the theory and writing the paper.

Letter Vol. 42, No. 16 / August 15 2017 / Optics Letters 3225

Optics Letters

Beyond the perturbative description of the nonlinear optical response of low-index materials

Orad Reshef,[1,*] Enno Giese,[1] M. Zahirul Alam,[1] Israel De Leon,[2] Jeremy Upham,[1] and Robert W. Boyd[1,3]

[1]Department of Physics, University of Ottawa, 25 Templeton Street, Ottawa, Ontario K1N 6N5, Canada
[2]School of Engineering and Sciences, Tecnológico de Monterrey, Monterrey, Nuevo León 64849, Mexico
[3]Institute of Optics and Department of Physics and Astronomy, University of Rochester, Rochester, New York 14627, USA
*Corresponding author: orad@reshef.ca

Received 30 May 2017; accepted 11 July 2017; posted 14 July 2017 (Doc. ID 295952); published 14 August 2017

We show that standard approximations in nonlinear optics are violated for situations involving a small value of the linear refractive index. Consequently, the conventional equation for the intensity-dependent refractive index, $n(I) = n_0 + n_2 I$, becomes inapplicable in epsilon-near-zero and low-index media, even in the presence of only third-order effects. For the particular case of indium tin oxide, we find that the $\chi^{(3)}$, $\chi^{(5)}$, and $\chi^{(7)}$ contributions to refraction eclipse the linear term; thus, the nonlinear response can no longer be interpreted as a perturbation in these materials. Although the response is non-perturbative, we find no evidence that the power series expansion of the material polarization diverges. © 2017 Optical Society of America

OCIS codes: (190.0190) Nonlinear optics; (190.3270) Kerr effect.

https://doi.org/10.1364/OL.42.003225

Nonlinear optical effects are crucial to many applications in photonics, performing essential functions in lasing, frequency conversion, and entangled-photon generation, among others [1–4]. Due to the small intrinsic nonlinearities of common photonic materials, there has long been the desire to increase optical nonlinearities in order to increase conversion efficiencies, miniaturize device footprints, and reduce power requirements in optical devices. Much of the recent work has been towards enhancing nonlinearities by structuring materials, for example, using high-Q micro-cavities [5–7] or photonic crystals with slow light propagation [7,8].

Recently, a class of low-index materials called epsilon-near-zero (ENZ) materials, whose real part of the electric permittivity ϵ' vanishes at a certain wavelength, has emerged as a promising platform to achieve unprecedented large nonlinear responses [9–11]. For example, in indium tin oxide (ITO), the nonlinear contribution to the index of refraction Δn has achieved a value of 0.72 [9]. This value is considerably larger than what has been achieved in highly nonlinear chalcogenide glasses ($\Delta n \approx 10^{-6}$) [12–14], and could enable all-optical switching in a propagation length smaller than a single wavelength. With recent developments in the integration of zero-index metamaterials, whose zero-refractive-index wavelength can be arbitrarily selected to suit the application [15–19], it has become critical to conduct an in-depth investigation of the nonlinear optical response of low-index media.

The recently demonstrated magnitude of nonlinear responses of ENZ materials is paradigm-shifting, and questions certain established fundamental assumptions in the field of nonlinear optics. For example, in a recent publication on the nonlinearity of aluminum-doped zinc oxide (AZO), the authors claim that "the ENZ nonlinearity in AZO [is] in a regime where the approximation of expanding the material polarization in a power series breaks down" [10]. Here, we theoretically and experimentally explore the consequences of a vanishingly small permittivity on the nonlinear optical response.

We begin by deriving an expression for the intensity-dependent index of refraction caused solely by the third-order nonlinear susceptibility $\chi^{(3)}$. For simplicity, we assume a centrosymmetric material and neglect the tensor nature of the susceptibility, as well as material magnetic responses. This set of assumptions is reasonable for most nonlinear optical materials [4].

To the lowest nonlinear order, the polarization of a material illuminated by a monochromatic laser field is described as

$$P^{\mathrm{TOT}} = P + P^{\mathrm{NL}} = \epsilon_0 E[\chi^{(1)} + 3\chi^{(3)}|E|^2]. \tag{1}$$

Here, E is the complex amplitude of the applied electric field and $\chi^{(1)} \equiv \epsilon^{(1)} - 1$ corresponds to the linear response of the material, with $\epsilon^{(1)}$ being the linear relative permittivity. Thus, the relative permittivity, including only the $\chi^{(3)}$ nonlinearity, is

$$\epsilon = \epsilon^{(1)} + 3\chi^{(3)}|E|^2. \tag{2}$$

Since all of these quantities may be complex, we define the complex relative permittivity as $\epsilon = \epsilon' + i\epsilon''$ and the complex refractive index as $n = n' + in''$, where a single prime denotes the real part, and the double prime denotes the imaginary part, respectively. These two quantities are related by [20]

$$n = \sqrt{\epsilon} = \sqrt{\epsilon^{(1)} + 3\chi^{(3)}|E|^2}. \tag{3}$$

Together, these equations can be used to obtain the complex, intensity-dependent index of refraction n due to third-order contributions. We find that

3226 Vol. 42, No. 16 / August 15 2017 / Optics Letters Letter

$$n = \sqrt{n_0^2 + 2n_0 n_2 I}, \tag{4}$$

where we take $n_0 = \sqrt{\epsilon^{(1)}}$ to be the linear refractive index, I to be the optical field intensity

$$I = 2\mathrm{Re}(n_0)\epsilon_0 c|E|^2, \tag{5}$$

and we introduce the standard definition for the nonlinear index of refraction [4,20]

$$n_2 = \frac{3\chi^{(3)}}{4n_0\mathrm{Re}(n_0)\epsilon_0 c}. \tag{6}$$

In order to obtain a simpler relation for n, Eq. (4) is usually expanded in a power series under the assumption that $|2n_2 I/n_0| \ll 1$ [4], yielding

$$n = n_0\sqrt{1 + 2\frac{n_2 I}{n_0}} \approx n_0\left[1 + \frac{1}{2}\left(2\frac{n_2 I}{n_0}\right) + \ldots\right]. \tag{7}$$

In most materials, $|2n_2 I/n_0|$ is very small so that only the lowest order correction term is kept, resulting in the intensity-dependent refractive index being widely defined as

$$n = n_0 + n_2 I. \tag{8}$$

Hence, the change of the refractive index due to the nonlinearity is $\Delta n = n - n_0 \approx n_2 I$.

At this point, we pause to address a few concerns with this derivation when considering a vanishingly small index. First, in an ENZ material, $\Delta n/n_0$ can be larger than unity (e.g., in Al-doped ZnO, this ratio has been shown to equal 4.4 [10]). In this case, the assumption that permits the power series expansion of Eq. (7) and leads to Eq. (8) is violated. Therefore, this power series strictly *does not converge*, and Eq. (8) is not a valid approximation of the intensity-dependent index of refraction.

Second, Eq. (4) reveals an issue that is not immediately apparent from Eq. (8). As $|n_0| \to 0$, n approaches zero as well, appearing to eliminate all refraction, including any nonlinearities. This conflict in fact also exists within Eq. (8)—as $|n_0| \to 0$, the optical field intensity vanishes while, simultaneously, $n_2 \to \infty$, leaving their product $(n_2 I)$ in Eq. (8) seemingly undefined. Note that n_0 is only introduced in the nonlinear contribution to Eq. (4) in order to obtain Eq. (8) in the appropriate limit, and it is this factor of n_0 that leads to the ostensible divergence of n_2 for low-index materials. No artificial effects of this kind appear when we phrase the nonlinear optical response purely in terms of the susceptibility and the electric field. $\chi^{(3)}|E|^2$ remains a robust measure of the nonlinear response, even when n_2 and I take on exceptional values.

Thirdly, it is confounding to accurately interpret what it means to have an intensity that is identically zero when $\mathrm{Re}(n_0)$ vanishes in Eq. (5). When employing the optical field intensity instead of the complex field amplitude, we also need to address whether n_0 or n should be used in its definition, which is typically not an important consideration when $\Delta n \ll 1$.

We must conclude that it does not seem beneficial to introduce n_2 or the nonlinear index of refraction, as defined in Eq. (8), in the context of low-index materials. In order to avoid these issues, we posit that it is preferable to use the intensity-dependent index of refraction, as defined in Eq. (3), with the square root, the nonlinear susceptibility, and the electric field amplitude directly. Though this equation is present in standard textbooks on nonlinear optics [4], it appears only as a step in the derivation for Eq. (8). Here, we have identified, to the best of our knowledge, the first case where its use becomes necessary to model the optical response.

We demonstrate the significance of these insights by considering experimental results. Except where explicitly stated, we focus our discussion on the single wavelength where the linear permittivity $\mathrm{Re}(\epsilon^{(1)}) = 0$, which typically corresponds to the wavelength where the index is at its lowest, and Δn has been shown to attain its peak value [9]. In the experiment, originally reported in Ref. [9], the transmission and reflection are measured through a thin film as a function of intensity. Since the index change is so large, the Fresnel coefficients at the boundaries of the film change dramatically, which allows for the detection of measurable changes in these quantities as a function of intensity. We then extract both the real and imaginary parts of the refractive index from the measured transmission and reflection using a transfer-matrix method [21]. The measurements are performed on a 310 nm thick film of ITO using 150 fs pulses at an oblique angle of 30°. The linear permittivity of ITO has a zero-crossing at $\lambda = 1240$ nm and a correspondingly large nonlinearity at this wavelength [9]. However, it does not exhibit a true instantaneous Kerr nonlinearity, as the material exhibits a finite optical recovery time [22,23]. Additionally, extracting nonlinear coefficients using this method will be highly dependent on external factors other than the microscopic properties of the material. For these reasons, we denote the nonlinear orders of the susceptibility as *effective* susceptibilities and restrict our discussion to a fixed pulse width, wavelength, and angle of incidence.

We begin by examining input intensities up to 50 GW/cm^2, above which higher-order nonlinearities begin to make significant contributions to refraction. We present the outcome of this measurement in Fig. 1 as a function of the free-space incident pulse intensity I_0. We also plot Eq. (8) for comparison, using values extracted from independent ellipsometry and Z-scan measurements ($\mathrm{Re}(n_0) = 0.44$ and $\mathrm{Re}(n_2) = 0.016$ cm^2/GW) [9,24]. This equation provides an adequate estimate of the index at low intensities, but quickly fails to describe the refractive index as the intensity increases.

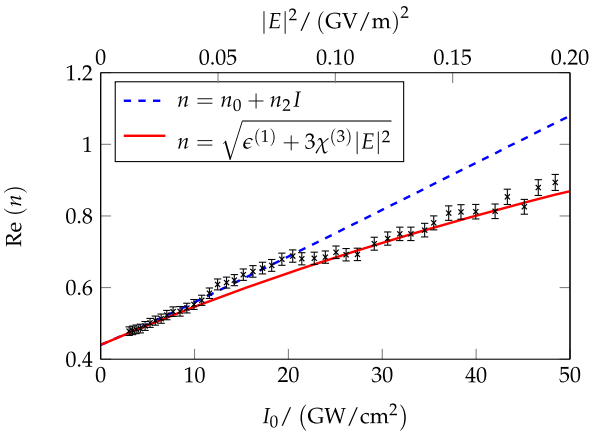

Fig. 1. Intensity-dependent index of the refraction of ITO at $\lambda = 1240$ nm, where the real part of the linear permittivity $\epsilon^{(1)}$ vanishes. Equation (8) performs poorly at describing the refractive index at most intensities (dashed blue line). Using Eq. (3), we obtain much-improved agreement with the measurement without additional fit parameters (red line). I_0 and E refer to the free-space intensity and the corresponding field magnitude for a plane wave inside the material, respectively.

Letter Vol. 42, No. 16 / August 15 2017 / Optics Letters 3227

In comparison, we plot Eq. (3) using these same material values. The resulting curve follows the measured refractive index much more accurately. We stress that the form of this curve is due solely to the square-root nature of Eq. (3); it is not caused by any absorption-based saturation effects or higher-order contributions to the nonlinear susceptibility. Recall that this form of the equation has been derived assuming only third-order contributions to the nonlinear polarization. Our treatment is different from a polynomial fit to the refractive index, since it preserves the original definition of n_2 and describes some of the nonlinear behavior, even in lowest order. At higher input intensities, the curve begins to deviate significantly from the measured values, due to the emergence of higher-order nonlinear effects. We discuss the contribution of these nonlinearities to refraction in the following.

The nonlinear polarization $P^{\mathrm{NL}}(E)$ can be defined to be a complex function of the electric field amplitude. Its explicit form may depend highly on the experimental realization and the microscopic model that describes the material. Therefore, its analytical form might not be accessible at all. In the present context, we are content with expanding the nonlinear polarization in a power series and describing the interaction by its macroscopic properties. Thus, our method can be applied even if there exists no good microscopic model for the material response.

For a single-beam input, we represent the material polarization with the following power series:

$$P^{\mathrm{TOT}}(E) = \epsilon_0 E \sum_{j\,\mathrm{odd}}^{\infty} c_j \chi^{(j)} |E|^{j-1}, \tag{9}$$

where c_j is a degeneracy factor [4]. We have included only odd orders of $\chi^{(j)}$ because only those contribute to refraction.

We extract ϵ from Eq. (9) and fit to the real and imaginary parts of the intensity-dependent refractive index of ITO for intensities up 275 GW/cm^2. The resulting curve correctly describes both n' and n'' at all intensities (Fig. 2). The extracted $\chi^{(j)}$ values are listed in Table 1. The real part of n_2 calculated using $\chi^{(3)}$ extracted in this process is $\mathrm{Re}(n_2) = 0.016$ cm^2/GW, in agreement with the previous measurement.

We use Pearson's statistical chi-squared value to determine the most appropriate fit for this dataset [25]. Fits with fewer nonlinear orders than $\chi^{(7)}$ yield a significantly larger statistical error (i.e., larger chi-squared). Including orders beyond $\chi^{(7)}$ only improves the statistical error marginally, indicative of overfitting. We thus attribute the nonlinear refraction of ITO to $\chi^{(3)}$, $\chi^{(5)}$, and $\chi^{(7)}$ nonlinearities at the investigated intensities.

Table 1. Values Extracted from the Fit to Eq. (9) with a Third-, Fifth-, and Seventh-Order Nonlinearity

j	$\mathrm{Re}(\chi)^{(j)}/(10^{-9}\mathrm{m/V})^{j-1}$	$\mathrm{Im}(\chi)^{(j)}/(10^{-9}\mathrm{m/V})^{j-1}$
1	-0.980 ± 0.008	0.36 ± 0.01
3	1.60 ± 0.03	0.50 ± 0.05
5	-0.63 ± 0.02	-0.25 ± 0.04
7	$(7.7 \pm 0.3) \times 10^{-2}$	$(3.5 \pm 0.8) \times 10^{-2}$

To examine the contributions of different orders to the refractive index, we plot them as functions of intensity in Fig. 3. At the highest input intensities, the linear refractive index makes only the fourth largest contribution to the total refractive index, providing further evidence that nonlinear optical effects cannot be treated solely as perturbations to linear optics. In fact, for an accessible range of operating intensities, nonlinear effects dominate the optical response of this material.

At the maximum utilized pump intensity, $I_{\mathrm{max}} = 275$ GW/cm^2, the $\chi^{(5)}$ term makes the largest contribution to the total refractive index; this term contributes more than the $\chi^{(3)}$ term, which is typically considered to be the dominant mechanism for n_2 and Δn. Additionally, the $\chi^{(7)}$ term is also significant, accounting for 20% of the total susceptibility.

Next, we use these extracted values to directly address whether the large nonlinearities that have been observed in ENZ materials violate traditional formulations of nonlinear optics that are based on the power series expansion of the nonlinear polarization.

The convergence of the power series in Eq. (9) can be determined using the ratio test

$$\lim_{j\to\infty} \left| \frac{c_{j+2}\chi^{(j+2)}|E|^{j+1}}{c_j \chi^{(j)}|E|^{j-1}} \right| < 1. \tag{10}$$

When this inequality is satisfied, the series converges. Thus, we see that $\Delta n/n$ and n_2 are not the relevant quantities for a discussion on convergence of the nonlinear polarization, even

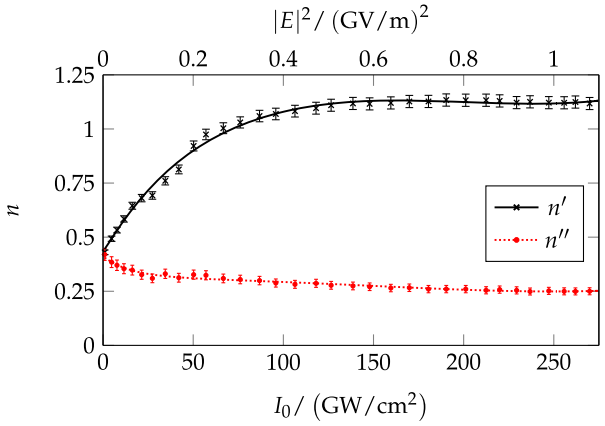

Fig. 2. Despite the saturation behavior at high intensities, we can correctly fit both the real and imaginary parts of the index of refraction of ITO for intensities up to 275 GW/cm^2 with the addition of appropriate $\chi^{(5)}$ and $\chi^{(7)}$ terms.

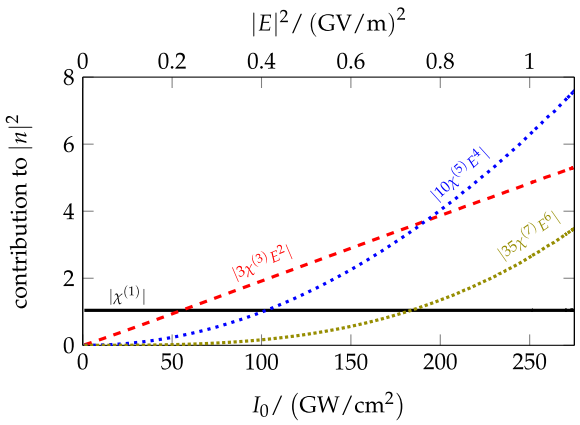

Fig. 3. Absolute contribution of the various orders of the nonlinear susceptibility to the refractive index of ITO at the wavelength where $\mathrm{Re}(\epsilon^{(1)}) = 0$. These contributions are estimated using the values for $\chi^{(j)}$ in Table 1.

3228 Vol. 42, No. 16 / August 15 2017 / *Optics Letters* **Letter**

though their magnitude is critical to the convergence of Eq. (7). Instead, the various nonlinear orders of the susceptibility $\chi^{(j)}$ determine its convergence. We note from Fig. 3 that the first few terms in the series violate the inequality since, at the maximum intensity investigated, the fifth-order contribution to refraction (7.6 ± 0.3) is larger than the third order-contribution (5.30 ± 0.09) which, in turn, is larger than the linear contribution (1.043 ± 0.004). However, the corresponding ratio between the $\chi^{(7)}$ and $\chi^{(5)}$ terms obeys the criterion in Eq. (10).

Though we have no access to the coefficients in the limit of $j \to \infty$, we remark that they must be negligible at the investigated intensities, since we can accurately fit to the refraction without them. For example, $\chi^{(9)}$ was not found to be statistically different from zero; therefore, its contribution to the refractive index is insignificant, even at the maximum intensity investigated and, in particular, must be smaller than the seventh-order term, obeying the convergence criterion. Thus, we conclude that the large nonlinear index of refraction that is observed in ENZ materials is nonetheless consistent with a power series description of the nonlinear polarization.

The above treatment and discussion prominently demonstrate that there is indeed a need to reinterpret established quantities related to the optical response in materials with small indices of refraction. We conclude that, in this unique scenario, it is no longer appropriate to use the approximation of the intensity-dependent index of refraction that only depends linearly on the intensity, even when only accounting for $\chi^{(3)}$ nonlinearities. Instead, we have introduced a more general equation with a square-root dependence. The linear slope with which the community is familiar is merely a special case of Eq. (3) for when the linear index is large. Because it is based on so few assumptions, our method will continue to work in cases that are not explicitly considered in this Letter, such as if $|n_0| \gg 0$ or $|\Delta n/n| \sim 1$. The generalized equation developed here has the benefit of preserving the standard historical definition of n_2 as a function of $\chi^{(3)}$ [Eq. (6)], as well as the physical definition of n_2 as the *initial* slope for the refractive index with respect to the applied optical intensity, i.e., $n_2 \equiv \lim_{I\to 0} \partial n/\partial I$. However, since the definition of n_2 is problematic in the context of low-index materials, $\chi^{(3)}$ or Δn should be used to characterize materials, instead.

We have demonstrated how to extend our generalized equation to incorporate higher-order nonlinear terms and absorption. Besides the assumption that the nonlinear susceptibility can be expanded in a power series, this treatment tracks the measured refraction for intensities up 275 GW/cm^2 without the need for a detailed microscopic model or empirical saturation equations [26,27]. Though our treatment cannot make predictions for even higher intensities, it enables quantitative statements regarding the convergence of the material polarization. It may also be used to systematically estimate the magnitude of higher-order contributions. Incidentally, we have shown that the nonlinear properties of ITO are even more striking than previously realized. At the highest probed intensities, the index of refraction is dominated by a fifth-order nonlinearity whose contribution grows roughly with I^2. We have also detected significant contributions to refraction caused by seventh-order nonlinearities. The nonlinear contributions from $\chi^{(3)}$, $\chi^{(5)}$, and $\chi^{(7)}$ terms each exceed the linear refraction term, making ENZ materials, to the best of our knowledge, the first solid-state platform to possess this property.

Finally, we have quantitatively shown that there is no evidence that the power series expansion for the nonlinear polarization in ENZ materials diverges at the wavelength where the linear permittivity vanishes. However, the dominant higher-order nonlinear contributions that have been observed reveal that ENZ materials operate in a regime where nonlinear optical effects can no longer be treated as a perturbation to linear optics.

Funding. Natural Sciences and Engineering Research Council of Canada (NSERC)—Banting Postdoctoral Fellowship; Canada Excellence Research Chairs, Government of Canada (CERC); Eugen Lommel stipend; Friedrich-Alexander-Universität Erlangen-Nürnberg (FAU).

REFERENCES

1. A. E. Siegman, *Lasers*, revised ed. (University Science Books, 1986).
2. P. G. Kwiat, K. Mattle, H. Weinfurter, A. Zeilinger, A. V. Sergienko, and Y. Shih, Phys. Rev. Lett. **75**, 4337 (1995).
3. T. J. Kippenberg, R. Holzwarth, and S. A. Diddams, Science **332**, 555 (2011).
4. R. W. Boyd, *Nonlinear Optics*, 3rd ed. (Academic, 2008).
5. J. E. Heebner and R. W. Boyd, Opt. Lett. **24**, 847 (1999).
6. J. Bravo-Abad, A. Rodriguez, P. Bermel, S. G. Johnson, J. D. Joannopoulos, and M. Soljacic, Opt. Express **15**, 16161 (2007).
7. M. Soljačić and J. D. Joannopoulos, Nat. Mater. **3**, 211 (2004).
8. Y. Hamachi, S. Kubo, and T. Baba, Opt. Lett. **34**, 1072 (2009).
9. M. Z. Alam, I. De Leon, and R. W. Boyd, Science **352**, 795 (2016).
10. L. Caspani, R. P. M. Kaipurath, M. Clerici, M. Ferrera, T. Roger, J. Kim, N. Kinsey, M. Pietrzyk, A. Di Falco, V. M. Shalaev, A. Boltasseva, and D. Faccio, Phys. Rev. Lett. **116**, 233901 (2016).
11. A. Capretti, Y. Wang, N. Engheta, and L. Dal Negro, Opt. Lett. **40**, 1500 (2015).
12. J. M. Harbold, F. Ö. Ilday, F. W. Wise, J. S. Sanghera, V. Q. Nguyen, L. B. Shaw, and I. D. Aggarwal, Opt. Lett. **27**, 119 (2002).
13. R. E. Slusher, G. Lenz, J. Hodelin, J. Sanghera, L. B. Shaw, and I. D. Aggarwal, J. Opt. Soc. Am. B **21**, 1146 (2004).
14. B. J. Eggleton, B. Luther-Davies, and K. Richardson, Nat. Photonics **5**, 141 (2011).
15. X. Huang, Y. Lai, Z. H. Hang, H. Zheng, and C. T. Chan, Nat. Mater. **10**, 582 (2011).
16. P. Moitra, Y. Yang, Z. Anderson, I. I. Kravchenko, D. P. Briggs, and J. Valentine, Nat. Photonics **7**, 791 (2013).
17. Y. Li, S. Kita, P. Muñoz, O. Reshef, D. I. Vulis, M. Yin, M. Lončar, and E. Mazur, Nat. Photonics **9**, 738 (2015).
18. S. Kita, Y. Li, P. Camayd-Muñoz, O. Reshef, D. I. Vulis, M. Yin, M. Lončar, and E. Mazur, Opt. Express **25**, 8326 (2017).
19. D. I. Vulis, Y. Li, O. Reshef, P. Camayd-Muñoz, M. Yin, S. Kita, M. Lončar, and E. Mazur, Opt. Express **25**, 12381 (2017).
20. R. del Coso and J. Solis, J. Opt. Soc. Am. B **21**, 640 (2004).
21. A. Yariv and P. Yeh, *Photonics: Optical Electronics in Modern Communications*, 6th ed. (Oxford University, 2007).
22. N. Rotenberg, A. D. Bristow, M. Pfeiffer, M. Betz, and H. M. van Driel, Phys. Rev. B **75**, 155426 (2007).
23. M. Conforti and G. Della Valle, Phys. Rev. B **85**, 245423 (2012).
24. M. Sheik-Bahae, D. J. Hagan, and E. W. Van Stryland, Phys. Rev. Lett. **65**, 96 (1990).
25. P. Young, "Everything you wanted to know about Data Analysis and Fitting but were afraid to ask," arXiv:1210.3781 (2014).
26. F. Smektala, C. Quemard, V. Couderc, and A. Barthélémy, J. Non-Cryst. Solids **274**, 232 (2000).
27. Y.-F. Chen, K. Beckwitt, F. W. Wise, B. G. Aitken, J. S. Sanghera, and I. D. Aggarwal, J. Opt. Soc. Am. B **23**, 347 (2006).

6 BROADBAND FREQUENCY TRANSLATION THROUGH TIME REFRACTION IN AN EPSILON-NEAR-ZERO MATERIAL

CONTRIBUTION STATEMENT:

Professor Boyd and I conceived this work after we saw the effect while performing the measurements presented in Chapter 2. We subsequently refined this idea with Jeremy Upham who worked on adiabatic wavelength conversion during his Ph.D. in Japan. I performed the first set of laboratory tests investigating the magnitude of the effect. A detailed account of contributions can be found in the section titled "Author contributions".

nature COMMUNICATIONS

ARTICLE

https://doi.org/10.1038/s41467-020-15682-2 OPEN

Broadband frequency translation through time refraction in an epsilon-near-zero material

Yiyu Zhou [1,4✉], M. Zahirul Alam[2,4], Mohammad Karimi[2], Jeremy Upham[2], Orad Reshef [2], Cong Liu [3], Alan E. Willner[3] & Robert W. Boyd [1,2]

Space-time duality in paraxial optical wave propagation implies the existence of intriguing effects when light interacts with a material exhibiting two refractive indexes separated by a boundary in time. The direct consequence of such time-refraction effect is a change in the frequency of light while leaving the wavevector unchanged. Here, we experimentally show that the effect of time refraction is significantly enhanced in an epsilon-near-zero (ENZ) medium as a consequence of the optically induced unity-order refractive index change in a sub-picosecond time scale. Specifically, we demonstrate broadband and controllable shift (up to 14.9 THz) in the frequency of a light beam using a time-varying subwavelength-thick indium tin oxide (ITO) film in its ENZ spectral range. Our findings hint at the possibility of designing (3 + 1)D metamaterials by incorporating time-varying bulk ENZ materials, and they present a unique playground to investigate various novel effects in the time domain.

[1] The Institute of Optics, University of Rochester, Rochester, NY 14627, USA. [2] Department of Physics, University of Ottawa, Ottawa, ON K1N 6N5, Canada. [3] Department of Electrical Engineering, University of Southern California, Los Angeles, CA 90089, USA. [4] These authors contributed equally: Yiyu Zhou, M. Zahirul Alam. ✉email: yzhou62@ur.rochester.edu

Maxwell's equations describe how an electromagnetic wave is modified by a material. The spatial boundary condition associated with Maxwell's equations can be used to derive the well-known Fresnel equations and Snell's law. A spatial variation in refractive index leads to reflection and refraction of a light beam incident on the boundary. As a consequence, the wavevector of the transmitted light changes, whereas the frequency is conserved. The spatial boundary can be abrupt (nonadiabatic) in refractive index variation such as at a glass-air interface. Or, the boundary can be smoothly varying, i.e., adiabatic in space, such as in a gradient-index lens. In both cases, the refracted beam of light must have a different k-vector (Fig. 1a), where $|k| = 2\pi n/\lambda$, n is the refractive index of the medium, and λ is vacuum wavelength of light. As the equations describing the paraxial wave propagation are unchanged upon the interchange of time and a spatial coordinate, one can define a boundary of refractive index in the time coordinate in a dual fashion to that in the spatial coordinates[1–5]. This effect is known as time refraction.

The concept of time refraction is presented in Fig. 1a. Let us assume that an optical pulse of frequency f_1 is traveling in a dispersionless medium with a refractive index of n_1. At $t = t_1$ the refractive index changes from n_1 to n_2. As a consequence of the broken time translation symmetry, the frequency of light has to change because of the change in the refractive index while leaving the wavevector unchanged[6]. The change in frequency, according to the dispersion relation $c/f = n\lambda$[7], can be expressed as $n_1 f_1 = n_2 f_2 = (n_1 + \Delta n)(f_1 + \Delta f)$, where $\Delta f = f_2 - f_1$ is the change in the frequency of light after it encounters the temporal boundary; $\Delta n = n_2 - n_1$ is the change in the refractive index; and c is the speed of light in vacuum. Consequently, we can express the change in frequency as $\Delta f = -\Delta n \cdot f_1/(n_1 + \Delta n)$. Thus, the frequency shift may be red (blue) if the change in index Δn is positive (negative). This effect is strongest when $\Delta n/(n_1 + \Delta n)$ is large. In a regular dielectric medium such as silicon[8], $\Delta n/(n_1 + \Delta n)$ can only be on the order of 10^{-3}. In contrast, in a highly nonlinear low-index medium, $\Delta n/(n_1 + \Delta n)$ can approach unity due to the near-zero linear refractive index n_1 and the large nonlinear index change Δn[9–11]. Thus, a highly nonlinear low-index medium is a natural platform with which to generate a large frequency translation using time refraction. In addition to frequency conversion, a time-varying medium with a large index change can also be used to investigate many novel effects in the time domain such as all-optical nonreciprocity[12,13], negative refraction[14], photonic topological insulators[15], photonic time crystals[16], achromatic optical switches[17], and the dynamic Casimir effect[18].

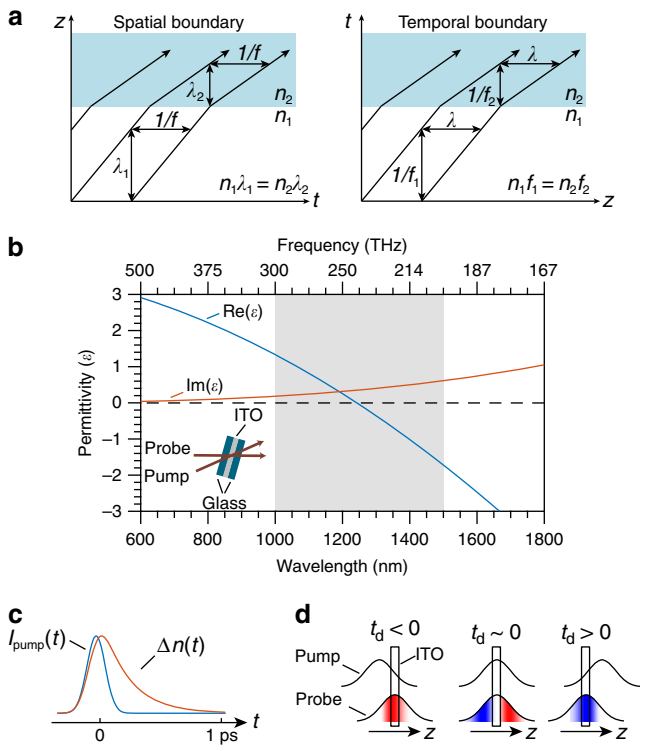

Fig. 1 Concept of time refraction. a A spatial boundary defined by a refractive index change from n_1 to n_2 leads to a change in the wavevector of a light beam as it passes through the boundary and is described by $n_1\lambda_1 = n_2\lambda_2$ (left panel). A refractive index boundary defined in time leads to time-refraction effect of a light beam as it passes through the boundary and is described by $n_1 f_1 = n_2 f_2$ (right panel). Here f is the frequency of light waves in the medium. **b** The permittivity of an ITO film used in the experiment. The inset shows the simplified experimental setup and the shaded region shows the spectral range of interest in this work. **c** Simplified illustration of the temporal index change $\Delta n(t)$ of ITO excited by a pump pulse. **d** The frequency of the probe redshifts (blueshifts) if the pump beam lags (leads) the probe. At near-zero delay both redshift and blueshift can occur.

Here, we show that we can simultaneously overcome all of the above-mentioned shortcomings by using a homogeneous and isotropic epsilon-near-zero (ENZ) medium of subwavelength thickness. Using a series of pump-probe measurements, we demonstrate optically controlled total frequency translations of a near-infrared beam of up to 14.9 THz (redshift of 11.1 THz and blueshift of 3.8 THz)—that is, over 6% of the bandwidth of the carrier frequency—using a 620-nm-thick ITO film. The effect of frequency translation is broadband in nature, i.e., the central wavelength of the degenerate input pump and probe pulses can be tuned over a 500 nm range. We also find that the effect is maximum near the zero-permittivity wavelength of ITO.

Results

Nonlinear optical response of the ENZ material. An ENZ material is defined as a medium that has a near-zero linear permittivity, and consequently low linear refractive index. The near-zero permittivity in such a medium leads to highly non-intuitive linear effects[41–43] and strong nonlinear light-matter interactions[9,44–47]. In order to implement a temporal boundary

with a large index change, we make use of the large and ultrafast optically induced change in refractive index of a 620 nm thick ITO film in its near-zero-permittivity spectral range. ITO is a degenerately doped semiconductor and near its zero-permittivity wavelength (1240 nm), the linear permittivity of the ITO sample can be well described by the Drude model (Fig. 1b). The temporal nonlinear optical response of ITO can be described by the two-temperature model when excited by an optical pulse with a central wavelength close to the ENZ region[9,44]. The optical excitation of ITO near the ENZ region leads to a strong modification of the Fermi-Dirac distribution of the conduction band electrons. The highly nonequilibrium distribution of electrons, within the formalism of the Drude model, leads to an effective redshift of the plasma frequency owing to the momentum-dependent effective mass of the electrons. According to the two-temperature model, the rise time of the change in the refractive index is limited by the thermalization time of the conduction band electrons owing to electron-electron scattering. The rise time also depends on the energy deposition rate in the ITO film and thus has a strong dependence on the temporal envelope of the pump pulse. Once the pump pulse peak leaves the ITO film, the index returns to the initial value within a sub-picosecond time scale through electron–phonon coupling (Fig. 1c). Owing to the time-dependent nature of the index change induced by the intensity of the pump pulse, the frequency of probe pulse can be redshifted or blueshifted depending on the pump-probe delay time (see Fig. 1d).

Measurements at the near-zero-permittivity wavelength. In order to measure the magnitude of the frequency translation using ITO, we performed a set of degenerate pump-probe experiments with ~120 fs pulses and recorded the spectra of the probe beam as a function of the delay between the pump and the probe for varying pump intensities. The ITO film has two 1.1-mm-thick glass slabs on both sides. Both pump and probe beams are *p*-polarized, and the intensity of the probe beam is kept low to avoid nonlinear effects (See Methods and Supplementary Note 1 for more details). The results for $\lambda_0 = \lambda_{pump} = \lambda_{probe} = 1235$ nm at the pump-probe delay time of ±60 fs is shown in Fig. 2. The pump induces a nonlinear change in the refractive index of ITO with a rate that depends on the pump intensity, the temporal envelope of the pump, and the intrinsic nonlinear dynamics of the ITO. When the pump pulse is delayed with respect to the probe, i.e., pump-probe delay time $t_d < 0$, the probe experiences a rising refractive index and thus its spectrum redshifts (Fig. 2a). If the probe reaches the ITO after the peak of the pump pulse is passed ($t_d > 0$), it experiences a falling refractive index change and the spectrum of the probe blueshifts (Fig. 2b). We also note that for $t_d \approx 0$ both blueshift and redshift can occur (Fig. 1d). As the thickness of the ITO film is only 620 nm, 120 fs pump, and the probe pulses never reside entirely within the ITO thin film (Fig. 1d). Thus, the magnitude of the frequency shift of the probe pulse becomes dependent on the index change rate $\Delta n/\Delta t$ it experiences while transiting through the ITO film. We extract the effective values of the index change rate based on the experimental data through numerical simulations (see Supplementary Note 2). In numerical simulation we use the slowly varying envelope approximation and, as a result, the predictions of our model are only dependent on the envelope-averaged dynamics of the ITO.

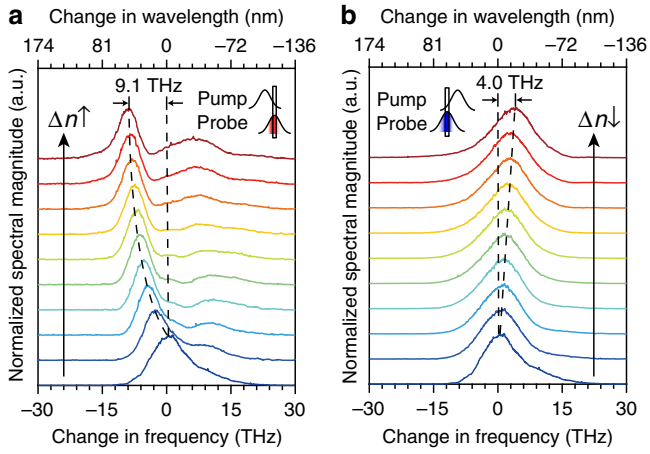

Fig. 2 Pump-induced frequency translation at a fixed delay time. a–b The frequency of a 1235 nm probe beam redshifts at the delay time $t_d = -60$ fs in **a** and blueshifts at the delay time $t_d = 60$ fs in **b**. The insets show the relative position of the pump and the probe. The top-most (bottom-most) spectra in both panels correspond to the largest (zero) pump intensity and, consequently, the largest (zero) change in the refractive index.

We find that both the pump intensity and the value of the pump-probe delay time modify the spectra of the transmitted probe. We present the results for $\lambda_0 = 1235$ nm for three pump intensities in Fig. 3a–c. In general, the time refraction leads to the modification of amplitude, bandwidth, temporal width, and the carrier frequency of the probe pulse (see Supplementary Note 3). In order to focus on the spectral shift, the magnitude of spectrum for each pump-probe delay value is individually normalized in Fig. 3. We find that when the absolute value of the pump-probe delay time $|t_d|$ is increased, the magnitude of the frequency translation for the probe decreases. Furthermore, when pump-probe delays are small, the leading portion of the probe pulse experiences an increase in refractive index (thus redshifts), whereas the trailing portion experiences a decrease of refractive index (thus blueshifts). This is evident in Fig. 3a–c by the presence of two peaks at $t_d \approx 0$. For a fixed pump-probe delay time an increase in pump intensity leads to larger change in index and, as a result, a larger shift in the central frequency of the probe pulse. Furthermore, we find that the fall time of the index change is slower than the rise time of the index change. The fall time of the index change is longer because it—within the formalism of the two-temperature model—is dictated by the intrinsic electron–phonon coupling rate, the maximum temperature of the conduction band electrons, and the thermodynamical properties of the lattice. As a result, the rate of decrease in index after the pump leaves the ITO film is smaller compared with that of the rising edge, and therefore the magnitude of the achievable redshift for a constant pump intensity is larger than the achievable blueshift. At a sufficiently high pump intensity, we observe an appearance of a large blueshifted spectral peak when the pump is at 1235 nm owing to higher-order nonlinear optical effects. At a peak pump intensity of 483 GW cm^{-2} the blueshift can be as large as 10.6 THz (~52 nm in wavelength), and the total maximum frequency translation can be larger than 20 THz (see Supplementary Note 4). This value corresponds to a fractional frequency shift ($\Delta f/f_0$) of ~9%.

We model the time-refraction effect in ITO using the nonlinear Schrödinger equation, and the split-step Fourier method is used to numerically solve the Schrödinger equation[48]. We use an iterative algorithm to calculate the approximate shape of the time-varying nonlinear phase variations induced by the index change to fit the experimentally measured spectra (see Supplementary Note 2). The simulation results are shown in Fig. 3d–f. Our numerical model is in excellent agreement with the experimental data, confirming that the origin of the shift is owing to the rapid change of index experienced by the probe pulse while transiting through the ITO sample.

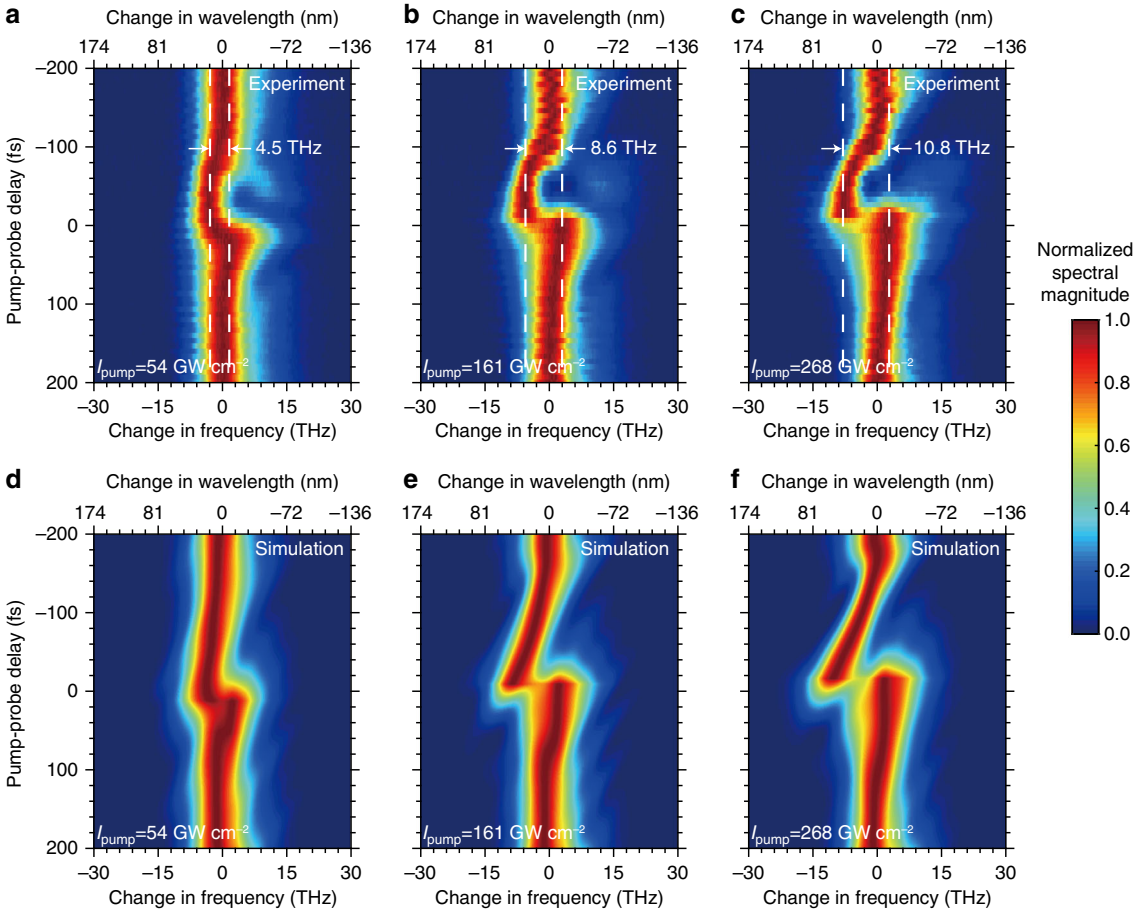

Fig. 3 Experimental and simulated probe spectra at $\lambda_0 = 1235$ nm. a–c Experimental probe spectra as a function of the pump-probe delay time for varying pump intensities. The spectral magnitude for each pump-probe delay is normalized individually. **d–f** The corresponding numerically simulated probe spectra modeled by the nonlinear Schrödinger equation. The spectra of the probe show a strong dependence on the pump intensity and pump-probe delay time. For a pump intensity of 268 GW cm^{-2}, the total frequency translation at this wavelength is 10.8 THz.

Measurements over a broad spectral range. Next, we investigate the dynamics away from the zero-permittivity wavelengths. We repeat the measurements at different excitation wavelengths from $\lambda_0 = 1000$ nm−1500 nm. For each excitation wavelength and pump intensity, we extract the maximum frequency translation of the probe over a range of pump-probe delay time (see Supplementary Note 5). We summarize the wavelength- and intensity-dependent maximum frequency translations in Fig. 4a–e. Here, we limit the pump intensities to avoid the occurrence of significant higher-order nonlinearities. Our results reveal a number of trends. First, both the total achievable frequency translation (redshift and blueshift) and the maximum achievable redshift for a constant pump intensity are the highest near 1235 nm (where $\mathrm{Re}(\varepsilon) \approx 0$) than at other wavelengths. For example, at $\lambda_0 = 1495$ nm the measured maximum magnitude of the redshift (5.4 THz) is a factor of two smaller than what can be achieved at $\lambda_0 = 1235$ nm using a lower pump intensity. Nevertheless, we find that the total maximum fractional frequency translation ($\Delta f/f_0$) at near-zero permittivity is unprecedentedly large (Fig. 4f). The maximum total frequency translation of 14.9 THz (redshift of 11.1 THz and blueshift of 3.8 THz) at $\lambda_0 = 1235$ nm (redshift plus blueshift) is over 53 times larger than what was achieved using a silicon ring resonator of a 6 μm diameter exhibiting a Q-factor greater than 18,000[20]. In contrast, the propagation distance in our material is only 620 nm which is 30 times shorter in physical length and four orders of magnitude smaller than the effective interaction length in a high-Q cavity. Moreover, our results show the operation bandwidth of ITO is much larger than what can be achieved using high-Q resonant structures.

Discussion

As the refractive index of the ENZ material depends on the intensity of the pump, the work presented here may be formally described by cross-phase modulation with a delayed response[8]. However, the concept of time refraction is independent of the source type of the index change (e.g., thermally, optomechanically, or electrically induced index change) and is a more general effect than the simple cross-phase modulation that arises when the temporal boundary is specifically induced by an optical pulse. Furthermore, in contrast to a typical four-wave-mixing-based frequency conversion, the frequency shift obtained through time refraction does not depend on the frequency difference between the pump and the probe and is completely free from phase-mismatching. Although in this work the pump and the probe are frequency degenerate and produced from the same source using a beam splitter, it is not necessary for the beams to be frequency degenerate. Nevertheless, the maximum frequency shift with minimum energy expenditure can be achieved when both the pump and the probe lie within the ENZ spectral range. As the maximum index change happens at the zero-permittivity wavelength, the probe will undergo maximum frequency shift if its wavelength is at or near the zero-permittivity wavelength, whereas the energy expenditure will be

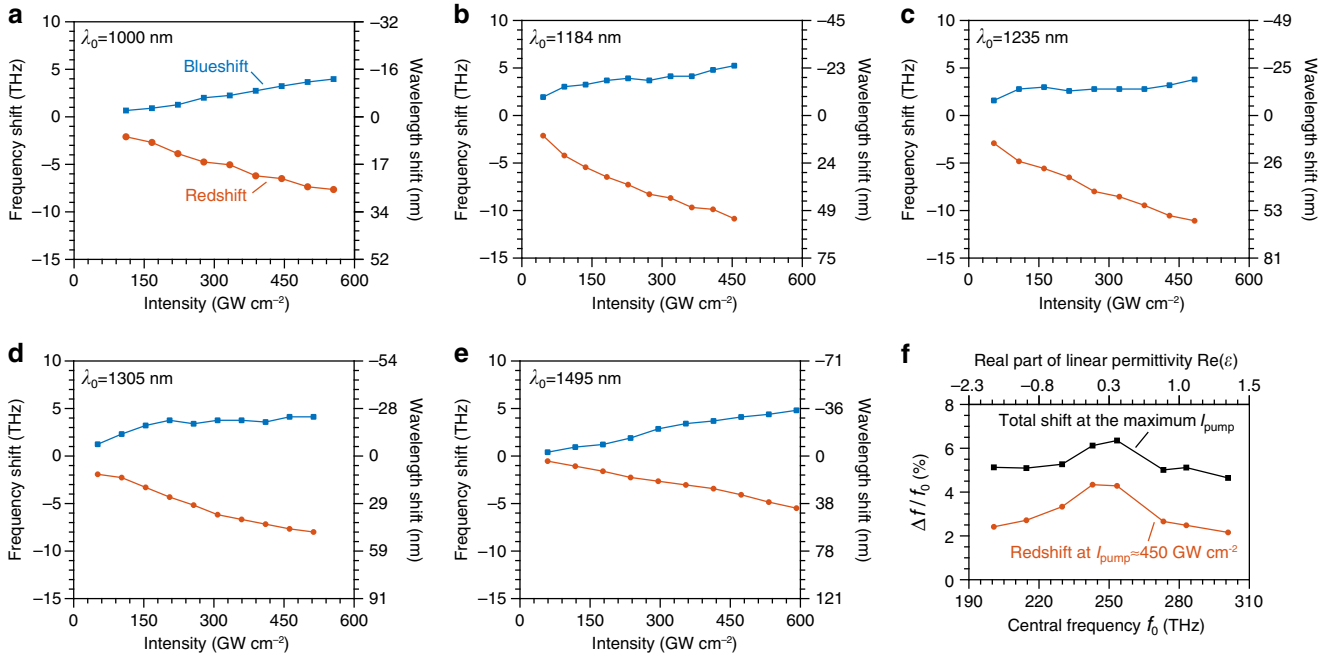

Fig. 4 Wavelength-dependent time-refraction effect. a–e Experimentally measured maximum redshifts and blueshifts at different wavelengths λ_0 as a function of peak pump intensities. **f** The red line denotes the fractional redshift $|\Delta f_{red}|/f_0$ as a function of probe beam's central frequency f_0 at a peak pump intensity ~450 GW cm^{-2}. The real part of the linear permittivity Re(ε) of ITO film at the corresponding central frequency f_0 is shown in the top axis. The black line shows the total fractional shift (redshift plus blueshift) measured at the maximum pump intensities before the onset of higher-order nonlinear optical effects. We find that both the maximum fractional redshift and the total shift occur near the zero-permittivity wavelength.

minimum if the wavelength of pump is also at or near the zero-permittivity wavelength.

In conclusion, we have shown that a subwavelength-thick ITO film can be used to obtain unprecedentedly large (~6.5% of the carrier frequency), broadband and tunable frequency translation. The large time-refraction effect in the ENZ material raises the intriguing possibility of wavelength conversion over an octave using a time-varying ENZ medium. The magnitude of the frequency translation is primarily limited by the linear loss, higher-order nonlinear optical effects, dispersion, and the interplay between the pulse width and the interaction time. We note that the ENZ spectral region of ITO and other conducting oxides can be tuned at any wavelength between 1 μm and 3 μm by choosing the appropriate doping level[49,50]. Furthermore, because the effect is present in a bulk, homogeneous and isotropic material, one can engineer nanostructures incorporating ENZ media such as plasmonic waveguides, photonic crystal waveguides, and dynamic metasurfaces to arbitrarily control the sign and the magnitude of the frequency shift in order to build efficient octave-spanning frequency tuners while simultaneously lowering the required pump power by a few orders of magnitude[9]. For example, an appropriately engineered ITO-based platform can be used to shift an entire band of optical signals in the frequency domain. Such devices may find practical usage in quantum communication protocols requiring conversion of visible photons to infrared[51] and in classical coherent optical communications[52,53]. We anticipate that the large time-refraction effect, we report here, can be exploited to engineer magnet-free nonreciprocal devices[54,55], spatiotemporal metasurfaces[13], and to investigate photonic time crystals and other topological effects in the time domain[16,56] using free-space or on-chip ENZ-based structures.

Methods

Measurements. We use a tunable optical parametric amplifier (OPA) pumped by an amplified Ti:sapphire laser of ~120 fs for the experiments. The output of the OPA is split into two beams to produce the degenerate pump and probe beams using a pellicle beam splitter. Both beams are rendered *p*-polarized. The pump beam is focused onto the sample by a 25 cm lens yielding to a spot size of ~100 μm. The probe beam is focused by a 10 cm lens and its spot diameter is ~45 μm at 1235 nm. Although the spot size can change when the wavelength of the OPA output is adjusted, we always keep the probe beam spot size significantly smaller than the pump beam so that the probe beam experiences a nearly uniform change in the refractive index in the transverse dimensions. The angles of incidences are 15° and 10° for the pump and probe, respectively. The transmitted probe light is coupled to an optical spectrum analyzer via a multimode fiber with a 50 μm core diameter. The commercially available ITO thin film (PGO GmbH) has a thickness of 310 nm and is deposited on a 1.1-mm-thick glass substrate. We sandwich two such ITO films to make the 620 nm thick ITO sample by using a customized sample holder with adjustable tightening screws (See Supplementary Note 6). We use a translation stage to control the delay time between the pump and the probe beams. The experimental setup is presented in Supplementary Note 1.

Data availability

All data supporting this study are available from the corresponding author upon request.

Code availability

All relevant computer codes supporting this study are available from the corresponding author upon request.

Received: 6 March 2020; Accepted: 19 March 2020;
Published online: 01 May 2020

References

1. Akhmanov, S., Sukhorukov, A. & Chirkin, A. Nonstationary phenomena and space-time analogy in nonlinear optics. *Sov. Phys. JETP* **28**, 748–757 (1969).
2. Kolner, B. H. Space-time duality and the theory of temporal imaging. *IEEE J. Quant. Electron* **30**, 1951–1963 (1994).
3. Xiao, Y., Maywar, D. N. & Agrawal, G. P. Reflection and transmission of electromagnetic waves at a temporal boundary. *Opt. Lett.* **39**, 574–577 (2014).
4. Xiao, Y., Agrawal, G. P. & Maywar, D. N. Spectral and temporal changes of optical pulses propagating through time-varying linear media. *Opt. Lett.* **36**, 505–507 (2011).

5. Plansinis, B. W., Donaldson, W. R. & Agrawal, G. P. What is the temporal analog of reflection and refraction of optical beams? *Phys. Rev. Lett.* **115**, 183901 (2015).
6. Mendonça, J., Guerreiro, A. & Martins, A. M. Quantum theory of time refraction. *Phys. Rev. A* **62**, 033805 (2000).
7. Mendonça, J. & Guerreiro, A. Time refraction and the quantum properties of vacuum. *Phys. Rev. A* **72**, 063805 (2005).
8. Boyd, R. W. *Nonlinear optics*. 3rd edn (Elsevier, 2003).
9. Alam, M. Z., Schulz, S. A., Upham, J., De Leon, I. & Boyd, R. W. Large optical nonlinearity of nanoantennas coupled to an epsilon-near-zero material. *Nat. Photonics* **12**, 79–83 (2018).
10. Caspani, L. et al. Enhanced nonlinear refractive index in ε-near-zero materials. *Phys. Rev. Lett.* **116**, 233901 (2016).
11. Reshef, O., De Leon, I., Alam, M. Z. & Boyd, R. W. Nonlinear optical effects in epsilon-near-zero media. *Nat. Rev. Mat.* **4**, 535–551 (2019).
12. Yu, Z. & Fan, S. Complete optical isolation created by indirect interband photonic transitions. *Nat. Photonics* **3**, 91–94 (2009).
13. Shaltout, A. M., Shalaev, V. M. & Brongersma, M. L. Spatiotemporal light control with active metasurfaces. *Science* **364**, eaat3100 (2019).
14. Pendry, J. Time reversal and negative refraction. *Science* **322**, 71–73 (2008).
15. Fang, K., Yu, Z. & Fan, S. Realizing effective magnetic field for photons by controlling the phase of dynamic modulation. *Nat. Photonics* **6**, 782–787 (2012).
16. Lustig, E., Sharabi, Y. & Segev, M. Topological aspects of photonic time crystals. *Optica* **5**, 1390–1395 (2018).
17. Williamson, I. A. & Fan, S. Broadband optical switch based on an achromatic photonic gauge potential in dynamically modulated waveguides. *Phys. Rev. Appl.* **11**, 054035 (2019).
18. Wilson, C. M. et al. Observation of the dynamical casimir effect in a superconducting circuit. *Nature* **479**, 376–379 (2011).
19. Yacomotti, A. M. et al. Nonadiabatic dynamics of the electromagnetic field and charge carriers in high-q photonic crystal resonators. *Phys. Rev. Lett.* **96**, 093901 (2006).
20. Preble, S. F., Xu, Q. & Lipson, M. Changing the colour of light in a silicon resonator. *Nat. Photonics* **1**, 293–296 (2007).
21. Upham, J., Tanaka, Y., Asano, T. & Noda, S. On-the-fly wavelength conversion of photons by dynamic control of photonic waveguides. *Appl. Phys. Express* **3**, 062001 (2010).
22. Kampfrath, T. et al. Ultrafast adiabatic manipulation of slow light in a photonic crystal. *Phys. Rev. A* **81**, 043837 (2010).
23. Castellanos Muñoz, M., Petrov, A. Y. & Eich, M. All-optical on-chip dynamic frequency conversion. *Appl. Phys. Lett.* **101**, 141119 (2012).
24. Kondo, K. & Baba, T. Dynamic wavelength conversion in copropagating slow-light pulses. *Phys. Rev. Lett.* **112**, 223904 (2014).
25. Dekker, R. et al. Ultrafast kerr-induced all-optical wavelength conversion in silicon waveguides using 1.55 μm femtosecond pulses. *Opt. Express* **14**, 8336–8346 (2006).
26. Agrawal, G. P., Baldeck, P. & Alfano, R. Temporal and spectral effects of cross-phase modulation on copropagating ultrashort pulses in optical fibers. *Phys. Rev. A* **40**, 5063–5072 (1989).
27. Li, J., Olsson, B.-E., Karlsson, M. & Andrekson, P. A. Otdm add-drop multiplexer based on xpm-induced wavelength shifting in highly nonlinear fiber. *J. Lightwave Technol.* **23**, 2654–2661 (2005).
28. Mehta, P., Healy, N., Day, T., Badding, J. V. & Peacock, A. Ultrafast wavelength conversion via cross-phase modulation in hydrogenated amorphous silicon optical fibers. *Opt. Express* **20**, 26110–26116 (2012).
29. Bloembergen, N. Laser-induced electric breakdown in solids. *IEEE J. Quant. Electron.* **10**, 375–386 (1974).
30. Yablonovitch, E. Self-phase modulation of light in a laser-breakdown plasma. *Phys. Rev. Lett.* **32**, 1101–1104 (1974).
31. Wood, W. M., Siders, C. & Downer, M. Measurement of femtosecond ionization dynamics of atmospheric density gases by spectral blueshifting. *Phys. Rev. Lett.* **67**, 3523–3526 (1991).
32. Lopes, N. et al. Laser pulse frequency up-shifts by relativistic ionization fronts. *Europhys. Lett.* **66**, 371–377 (2004).
33. Fan, L. et al. Integrated optomechanical single-photon frequency shifter. *Nat. Photonics* **10**, 766–770 (2016).
34. Del'Haye, P. et al. Optical frequency comb generation from a monolithic microresonator. *Nature* **450**, 1214–1217 (2007).
35. Li, Q., Davanço, M. & Srinivasan, K. Efficient and low-noise single-photon-level frequency conversion interfaces using silicon nanophotonics. *Nat. Photonics* **10**, 406–414 (2016).
36. Gaafar, M. A. et al. Reflection from a free carrier front via an intraband indirect photonic transition. *Nat. Commun.* **9**, 1447 (2018).
37. Beggs, D. M., Krauss, T. F., Kuipers, L. & Kampfrath, T. Ultrafast tilting of the dispersion of a photonic crystal and adiabatic spectral compression of light pulses. *Phys. Rev. Lett.* **108**, 033902 (2012).
38. Lee, K. et al. Linear frequency conversion via sudden merging of meta-atoms in time-variant metasurfaces. *Nat. Photonics* **12**, 765–773 (2018).
39. Shcherbakov, M. R. et al. Photon acceleration and tunable broadband harmonics generation in nonlinear time-dependent metasurfaces. *Nat. Commun.* **10**, 1345 (2019).
40. Gaburro, Z. Photonic energy lifters and event horizons with time-dependent dielectric structures. *J. Nanophotonics* **2**, 021853 (2008).
41. Silveirinha, M. & Engheta, N. Tunneling of electromagnetic energy through subwavelength channels and bends using ε-near-zero materials. *Phys. Rev. Lett.* **97**, 157403 (2006).
42. Engheta, N. Pursuing near-zero response. *Science* **340**, 286–287 (2013).
43. Liberal, I. & Engheta, N. Near-zero refractive index photonics. *Nat. Photonics* **11**, 149–158 (2017).
44. Alam, M. Z., De Leon, I. & Boyd, R. W. Large optical nonlinearity of indium tin oxide in its epsilon-near-zero region. *Science* **352**, 795–797 (2016).
45. Kinsey, N. et al. Epsilon-near-zero al-doped zno for ultrafast switching at telecom wavelengths. *Optica* **2**, 616–622 (2015).
46. Ferrera, M. & Carnemolla, E. G. Ultra-fast transient plasmonics using transparent conductive oxides. *J. Optics* **20**, 024007 (2018).
47. Capretti, A., Wang, Y., Engheta, N. & Dal Negro, L. Enhanced third-harmonic generation in si-compatible epsilon-near-zero indium tin oxide nanolayers. *Opt. Lett.* **40**, 1500–1503 (2015).
48. Agrawal, G. P. Nonlinear fiber optics. in *Nonlinear Science at the Dawn of the 21st Century. Lecture Notes in Physics*, Vol. 542 (Springer, 2000).
49. Gui, Y. et al. Towards integrated metatronics: a holistic approach on precise optical and electrical properties of indium tin oxide. *Sci. Rep.* **9**, 1–10 (2019).
50. Yang, Y. et al. Femtosecond optical polarization switching using a cadmium oxide-based perfect absorber. *Nat. Photonics* **11**, 390–395 (2017).
51. Saglamyurek, E. et al. Quantum storage of entangled telecom-wavelength photons in an erbium-doped optical fibre. *Nat. Photonics* **9**, 83–87 (2015).
52. Yanik, M. F. & Fan, S. Stopping light all optically. *Phys. Rev. Lett.* **92**, 083901 (2004).
53. Yoo, S. B. Wavelength conversion technologies for wdm network applications. *J. Lightwave Technol.* **14**, 955–966 (1996).
54. Caloz, C. et al. Electromagnetic nonreciprocity. *Phys. Rev. Appl.* **10**, 047001 (2018).
55. Sounas, D. L., Caloz, C. & Alu, A. Giant non-reciprocity at the subwavelength scale using angular momentum-biased metamaterials. *Nat. Commun.* **4**, 2407 (2013).
56. Giergiel, K., Dauphin, A., Lewenstein, M., Zakrzewski, J. & Sacha, K. Topological time crystals. *N. J. Phys.* **21**, 052003 (2019).
57. Bruno, V. et al. Broad frequency shift of parametric processes in epsilon-near-zero time-varying media. *Appl. Sci.* **10**, 1318 (2020).

Acknowledgements

R.W.B. C.L., Y.Z. and A.E.W. acknowledge support from DARPA (grant No. W911NF-18-0369). O.R. acknowledges the support of the Banting Postdoctoral Fellowship from the Natural Science and Engineering Research Council, Canada. This work was supported by the US Office of Naval Research and the Natural Science and Engineering Research Council, Canada. Note: while our paper was in review, a complementary paper was submitted and published[57]. In contrast to our work, they demonstrate wavelength conversion using four-wave mixing process in a time-varying ENZ thin film.

Author contributions

M.Z.A., J.U., and R.W.B. conceived the work after serendipitous observation of the effect in the laboratory by M.Z.A. M.Z.A. performed the first set of laboratory tests. M.Z.A., Y.Z., O.R., and J.U. designed the experiment. Y.Z. with help from M.Z.A., M.K., O.R., J.U., and C.L. performed laboratory measurements. Y.Z. with help from M.Z.A. performed data analysis and developed the numerical model. Y.Z and M.Z.A. wrote the first draft. All authors contributed to the discussion of the results and the preparation of the final version of the manuscript. A.E.W. and R.W.B. supervised the work.

Competing interests

The authors declare no competing interests.

Additional information

Supplementary information is available for this paper at https://doi.org/10.1038/s41467-020-15682-2.

Correspondence and requests for materials should be addressed to Y.Z.

Peer review information *Nature Communications* thanks the anonymous reviewers for their contribution to the peer review of this work. Peer reviewer reports are available.

Reprints and permission information is available at http://www.nature.com/reprints

Publisher's note Springer Nature remains neutral with regard to jurisdictional claims in published maps and institutional affiliations.

Supplementary Information

Broadband frequency translation through time refraction in an epsilon-near-zero material

Zhou *et al*.

Supplementary Information

Yiyu Zhou[1,†,*], M. Zahirul Alam[2,†], Mohammad Karimi[2], Jeremy Upham[2], Orad Reshef[2], Cong Liu[3], Alan E. Willner[3] and Robert W. Boyd[1,2]

[1]The Institute of Optics, University of Rochester, Rochester, New York 14627, USA

[2]Department of Physics, University of Ottawa, Ottawa, Ontario K1N 6N5, Canada

[3]Department of Electrical Engineering, University of Southern California, Los Angeles, California, 90089, USA

[†]These authors contributed equally

[*]corresponding author: yzhou62@ur.rochester.edu

Supplementary Note 1: Experimental setup

We use a wavelength-tunable optical parametric amplifier (TOPAS prime, Spectra Physics) pumped by an amplified Ti:sapphire laser (Mai Tai, Spectra Physics) as the ultrafast pulse source. A 45:55 pellicle beamsplitter (BP245B3, Thorlabs) is used to split the input beam, and a high-precision translation stage (DDSM100, Thorlabs) is used to tune the delay time between pump and probe pulses. We use a thin film polarizer mounted on a rotation stage and a Glan-Taylor polarizing beam splitter to control the pulse intensity while keeping the polarization to be *p*-polarized. We use a multimode fiber with 50 μm core diameter to collect the probe pulse after the sample and use an optical spectrum analyzer to record the spectra of the probe.

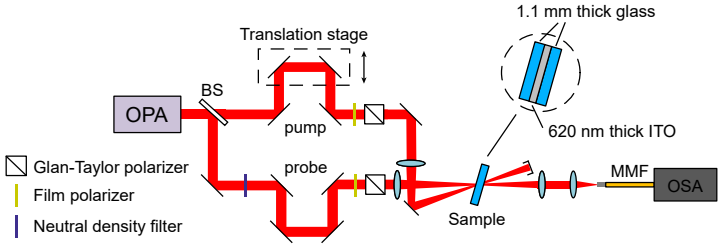

Supplementary Figure 1. The schematic of the experimental setup. In the pump beam arm, we rotate the first polarizer to control the peak pump intensity. BS, pellicle beamsplitter. OPA, optical parametric amplifier. OSA, optical spectrum analyzer. MMF, multimode fiber.

Supplementary Note 2: Numerical simulation

We use a split-step Fourier method to solve the nonlinear Schrödinger equation (NLSE)[1] to model the nonlinear interactions between the pump and the probe beam pulses propagating through the ITO sample. We ignore all nonlinear optical effects higher than the third-order effects[2]. The propagation of the probe pulse through the time-varying ITO can be described as[3]

$$\frac{\partial A}{\partial z}+\beta_1\frac{\partial A}{\partial t}+\mathrm{i}\frac{\beta_2}{2}\frac{\partial^2 A}{\partial t^2}=\mathrm{i}\frac{\omega_0}{c}\Delta n_{\mathrm{eff}}(t-t_{\mathrm{d}},I_{\mathrm{pump}}(t))A, \tag{1}$$

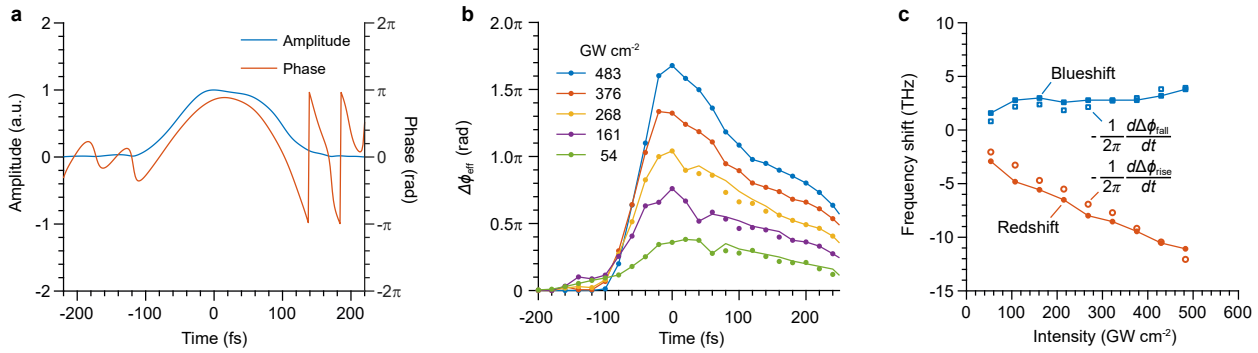

Supplementary Figure 2. **a**, Amplitude and phase of the optical pulses at 1235 nm retrieved by frequency-resolved optical gating. **b**, Numerically retrieved nonlinear phase variations $\Delta\phi_{\mathrm{eff}}(t)$ at different pump intensities. The dots represent the numerical results and the solid lines connecting the dots are to facilitate visualization. **c**, The experimentally measured redshifts and blueshifts as a function of pump intensity are represented by the solid lines, and the calculated maximum local frequency shifts are represented by hollow circles.

where $A(z,t)$ is the slowly varying envelope of the probe pulse, $\beta_1 \equiv (1/v_{\mathrm{g}})$ is the inverse of the group velocity, $\beta_2 \equiv \frac{\partial}{\partial\omega}(1/v_{\mathrm{g}})$ is the group velocity dispersion, c is the speed of light in vacuum, t_{d} is the pump-probe delay time, and ω_0 is the angular frequency of the light beams. The effective time-dependent refractive index index $\Delta n_{\mathrm{eff}}(t, I_{\mathrm{pump}})$ on the right-hand side is a function of pump intensity and the delay time between the pump and the probe. This term acts as the driving term for the nonlinear pulse propagation and is responsible for the frequency translation. The relative permittivity of ITO around its epsilon-near-zero spectral range can be modeled by a Drude function as[4]

$$\varepsilon(\omega) = \varepsilon_\infty - \omega_{\mathrm{p}}^2/(\omega^2 + \mathrm{i}\gamma\omega), \tag{2}$$

where $\varepsilon_\infty = 3.80$, $\omega = 2\pi c/\lambda$ is the frequency of light, $\omega_{\mathrm{p}} = 2\pi\cdot 473$ THz is the plasma frequency, and $\gamma = 0.0468\cdot 2\pi\cdot 473$ THz is the damping rate. The refractive index of ITO can thus be expressed as $n(\omega) = \sqrt{\varepsilon(\omega)}$. The dispersion coefficients can be calculated as $\beta_m = \left(\frac{d^m\beta}{d\omega^m}\right)_{\omega=\omega_0}$, where $\beta(\omega) = \mathrm{Re}(n(\omega))\omega/c$. At $\lambda = 1235$ nm we have $\beta_1 = 1.53\times 10^7$ fs m^{-1} and $\beta_2 = 1.10\times 10^8$ fs^2 m^{-1}. The dispersion length is found to be $L_{\mathrm{D}} = T_0^2/\beta_2 = 47.1$ μm, where $2\sqrt{\ln(2)}T_0 = 120$ fs is the FWHM pulse width. Since the dispersion length is two orders of magnitude larger than the ITO thickness of 0.62 μm, we neglect higher-order dispersion terms.

For the numerical simulation we ignore the changes in $\Delta n_{\mathrm{eff}}(t)$ that occur at the time scale of the oscillation of the carrier waves of the pump pulse. We only take into account the pump-envelope-dependent changes in the refractive index. Thus, in our simulation we approximate $\Delta n_{\mathrm{eff}}(t)$ as a function of the envelope of the pump pulse only. We use an iterative least squares curve fitting algorithm to extract an approximate shape of pump-intensity-dependent $\Delta n_{\mathrm{eff}}(t)$ that results in the experimentally obtained output probe spectra for a fixed pump intensity as follows: (1) We begin with an initial guess $\Delta n^1_{\mathrm{eff}}(t)$. For j-th iteration, the corresponding index change is denoted as $\Delta n^j_{\mathrm{eff}}(t)$. (2) For the index change $\Delta n^j_{\mathrm{eff}}(t)$ and a specific pump-probe delay time t'_{d}, we use $\Delta n^j_{\mathrm{eff}}(t - t'_{\mathrm{d}})$ in Supplementary Eq. (1) and perform the split-step Fourier method to generate an output pulse $A^j(z_1, t; t'_{\mathrm{d}})$,

where $z_1 = 620$ nm. The output spectrum can be calculated via Fourier transform as $S^j(f,t_d') = |\int A^j(z_1,t;t_d')\exp(-i2\pi ft)\,dt|^2$. We repeat this procedure for different delay times and therefore obtain the two-dimensional spectrogram $S^j(f,t_d)$ with -200 fs $\leq t_d \leq 200$ fs. (3) We use a fitting algorithm (lsqcurvefit, MATLAB) to fit $S^j(f,t_d)$ to the experimental data $S^{exp}(f,t_d)$ by adjusting $\Delta n_{eff}^j(t)$. In other words, $\Delta n_{eff}^j(t)$ is the parameter to be tuned iteratively. The final results of $S^j(f,t_d)$ at different pump intensities are presented in Fig. 3(d-f) in the manuscript.

In order to obtain the temporal amplitude and phase of the input probe pulses at the wavelengths of interest, i.e. $A(z=0,t)$, we performed a series of frequency-resolved optical gating (FROG) measurements[5]. In our simulation we always assume a homogeneous index change throughout the entire ITO film for simplification. We also ignore the time difference of the index change between the front and the back ends of the sample since the transit time through the sample is roughly two-orders of magnitude smaller than the temporal width of the pump pulse. We also ignore the Fresnel-reflection- and absorption-induced change in the pump intensity inside the sample for simplification. In addition, we also ignore nonlinear change in dispersion. The experimentally measured temporal amplitude and phase of the input probe pulse at 1235 nm is shown in Supplementary Fig. 2a.

An alternative way to understand the effect of index change is to use the concept of a local frequency shift. The local frequency shift can be used as an approximate estimation of spectral shift and can be expressed as[6]

$$\Delta f(t) = \frac{1}{2\pi}\Delta\omega(t) = -\frac{1}{2\pi}\frac{d\Delta\phi_{eff}(t)}{dt}, \tag{3}$$

where the nonlinear phase variation induced by Δn_{eff} is $\Delta\phi_{eff}(t) = k\cdot L\cdot\Delta n_{eff}(t)$, where $k = 2\pi/\lambda$ is the wavenumber, and $L = 620$ nm is the ITO thickness. The retrieved phase variation $\Delta\phi_{eff}$ is displayed for different peak pump intensities in Supplementary Fig. 2b. For a given $\Delta\phi_{eff}$, the maximum local frequency redshift is determined by the rising edge of the nonlinear phase change as $\Delta f_{red} = \min(\Delta f(t)) = -\frac{1}{2\pi}\frac{d\Delta\phi_{rise}}{dt}$, while the maximum local frequency blueshift is determined by the falling edge as $\Delta f_{blue} = \max(\Delta f(t)) = -\frac{1}{2\pi}\frac{d\Delta\phi_{fall}}{dt}$. The numerically retrieved maximum local frequency shifts at different pump intensities are shown in Supplementary Fig. 2c. The retrieved maximum local frequency shifts are in good agreement with the experimentally measured frequency shifts.

Supplementary Note 3: Additional time refraction effects and unnormalized spectra

Since the focus of this work is on frequency translation, we presented spectral data with normalized amplitude in the main text. However, time refraction also affects the amplitude of the frequency-translated pulse[7]. Let us consider the simplest time-refraction model — a Gaussian pulse with carrier frequency ω_0 and pulse width T_0 is travelling through a medium whose

refractive index changes from n_1 to n_2. We assume that the longitudinal length of the medium is larger than the longitudinal length of the pulse. In such an idealized case the input (E_{in}) and output (E_{out}) pulses can be expressed as[8]

$$E_{\text{in}} = E_0 \exp(-\frac{t^2}{2T_0^2}) \exp(-\mathrm{i}\omega_0 t), \qquad E_{\text{out}} = (\frac{n_1}{n_2} E_0)\ \exp(-\frac{t^2}{2(T_0 n_2/n_1)^2})\ \exp(-\mathrm{i}\frac{n_1}{n_2}\omega_0 t). \tag{4}$$

The above simple model shows that the time refraction effect can modify amplitude, temporal width (by Fourier relation the spectral width), and the central frequency. Therefore, the relative changes in spectral amplitude may also be of interest. Below we present the spectral data for five different probe wavelengths for various pump-probe delays in Supplementary Fig. 3-7, where the spectral peak magnitude in the absence of pump pulse is normalized to unity. However, it should be noted that in addition to time refraction there are several other competing effects in ITO that can significantly modulate the transmittance of the probe pulse. Since the ITO has a small linear index and exhibits a large nonlinear index change, the Fresnel reflection coefficients exhibit strong time-dependent variations. In addition, due to saturable absorption, the imaginary part of the refractive index and, consequently, the loss in ITO can drop significantly in the presence of a pump pulse. Thus the spectral amplitude of the probe for a given pump-probe delay and pump intensity depends on time-refraction effects, nonlinear changes in Fresnel reflection coefficient, and changes in absorption. Therefore a sophisticated model is required to isolate these three effects to accurately quantify the effect of time refraction on the amplitude, which is beyond the scope of this work. Nevertheless, it can be noticed that for all wavelengths of interest, the transmittance of the probe beam significantly increases when the probe is blueshifted.

We also note that the absorption loss in ITO in the ENZ spectral range is large compared to standard dielectric materials. We note that a fair figure of merit for such a medium should be the magnitude of nonlinear change over one absorption length. Clearly ITO cannot be used to make optical fibre or nanophotonics waveguides of hundreds of microns in length. The crucial advantage of these ENZ materials over other conventional materials is that one needs to propagate over only a sub-micron distance in a nonlinear ENZ material for a comparable effect that is achieved by a hundreds of microns long nanophotonic waveguide made of a conventional photonics material. It should be noted that for this work we are using a commercially available sample that has never been optimized for the purpose of this work. In addition, there are still many opportunities to further enhance the performance of ENZ materials. A few promising routes are: i) use an ENZ material with higher electron mobility, ii) nanostructure the ENZ material or include plasmonic systems to achieve higher effective index change within reduced thickness and loss, iii) integrate ENZ material with optical waveguides as the cladding, etc. We also note that in the presence of strong pump the transmittance of the probe can actually increase due to the increased refractive index and reduced loss. Finally, we note that the use of optical amplifiers to boost a weak signal is a standard system protocol. Furthermore, the recent advancement in short pulse amplification might also be of interest for particular applications[9].

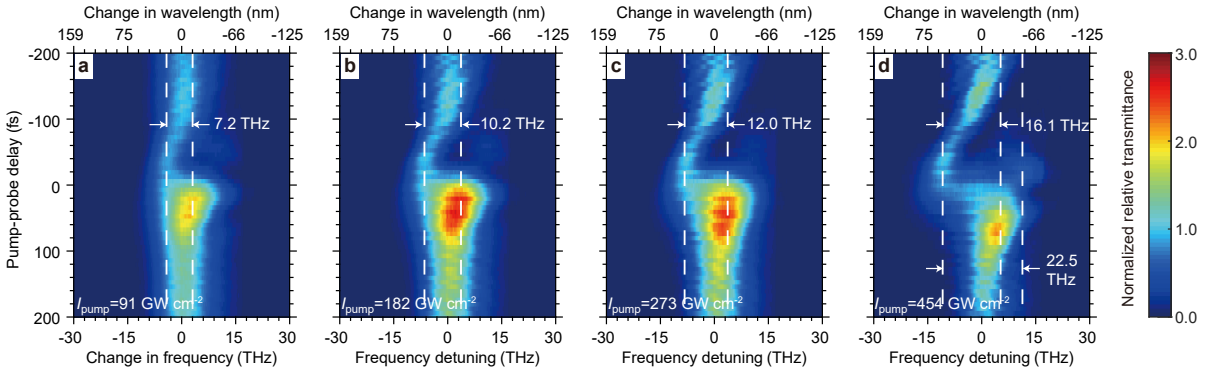

Supplementary Figure 3. **a-d**, The experimentally measured spectra of 1184 nm probe pulse at different pump intensities. The spectral peak of the probe beam in the absence of pump beam is normalized to unity.

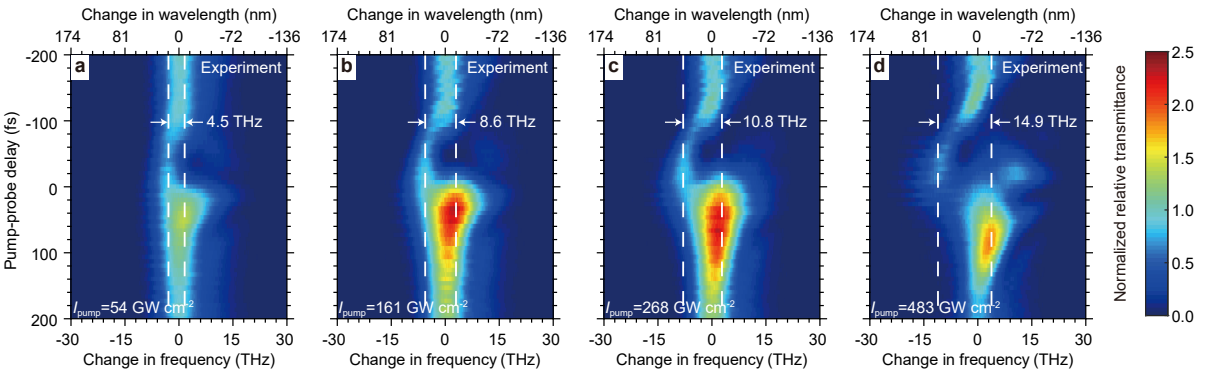

Supplementary Figure 4. **a-d**, The experimentally measured spectra of 1235 nm probe pulse at different pump intensities. The spectral peak of the probe beam in the absence of pump beam is normalized to unity.

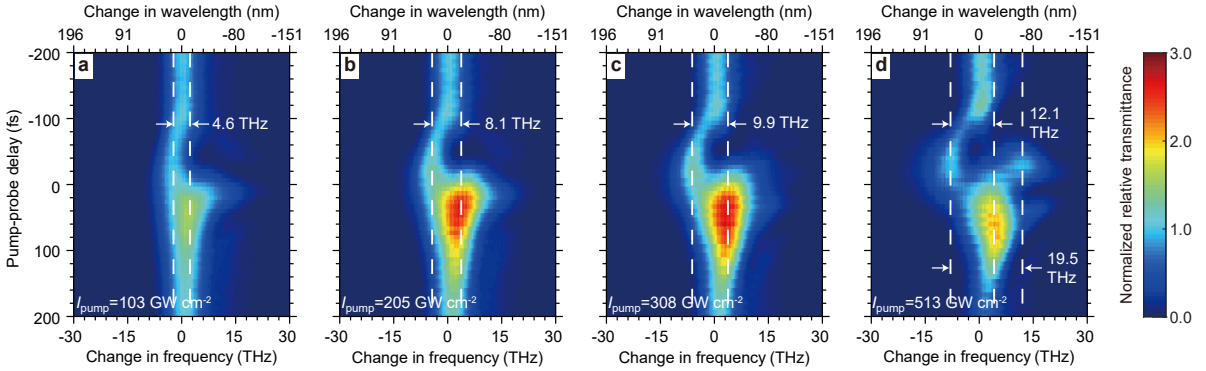

Supplementary Figure 5. **a-d**, The experimentally measured spectra of 1305 nm probe pulse at different pump intensities. The spectral peak of the probe beam in the absence of pump beam is normalized to unity.

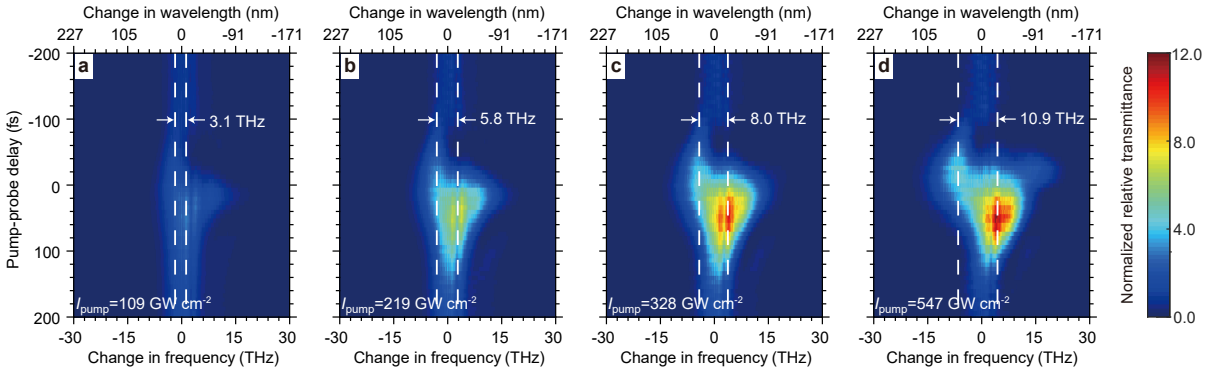

Supplementary Figure 6. **a-d**, The experimentally measured spectra of 1398 nm probe pulse at different pump intensities. The spectral peak of the probe beam in the absence of pump beam is normalized to unity.

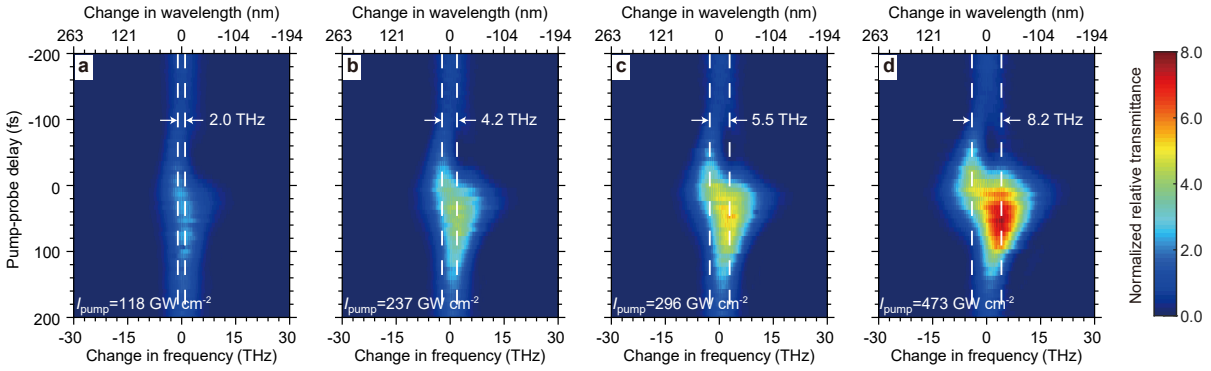

Supplementary Figure 7. **a-d**, The experimentally measured spectra of 1495 nm probe pulse at different pump intensities. The spectral peak of the probe beam in the absence of pump beam is normalized to unity.

Supplementary Note 4: Effects of fifth-order nonlinearity

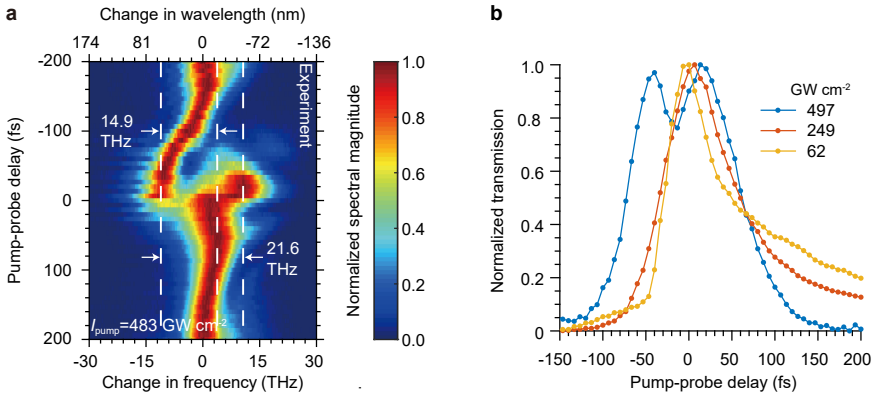

Supplementary Figure 8. **a**, The experimentally measured probe spectrogram at the peak pump intensity of 483 GW cm^{-2}. **b**, The experimentally measured probe transmission at different pump intensities as a function of pump-probe delay time.

At a high pump intensity of greater than 450 GW cm^{-2} close to the zero permittivity wavelength we observe onsets of higher-order nonlinear optical effects. For example, at $\lambda_0 = 1235$ nm at a pump intensity of 480 GW cm^{-2} we observe a relatively large blueshifted peak as shown in Supplementary Fig. 8a due to an effective fifth-order nonlinear optical process. In a pump-probe transmission measurement this effective fifth-order process leads to a sudden drop in the transmission of the probe Supplementary Fig. 8b. From these results we conclude that the effective fifth-order process has an opposite sign to that of the effective third-order process and that the relevant time scales for the fifth-order-nonlinearity-induced blue shift is much shorter compared to the effective third-order-nonlinearity-induced blue shift at lower intensities.

Supplementary Note 5: Normalized spectra at other wavelengths

Here, we provide the detailed measurement results for pump-probe wavelengths ranging from $\lambda = 1000$ nm to 1500 nm in Supplementary Fig. 9-14.

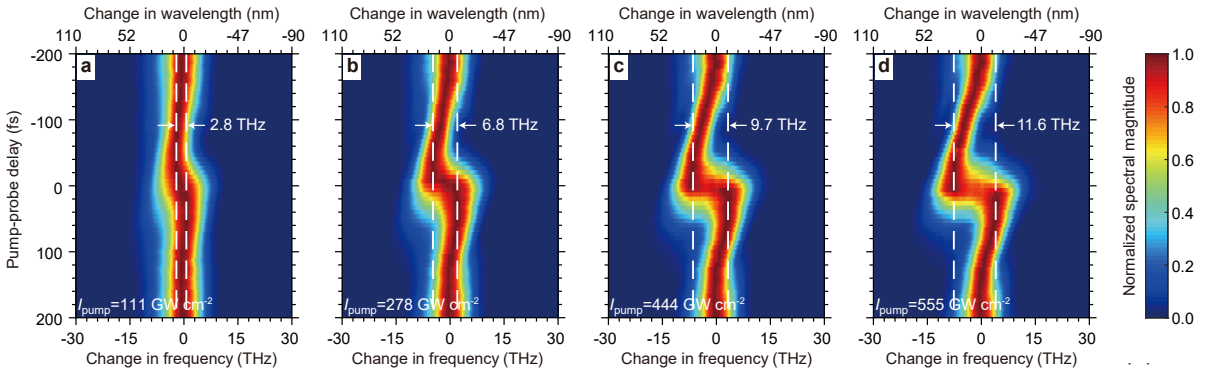

Supplementary Figure 9. a-d, The experimentally measured spectra of 1000 nm probe pulse at different pump intensities. The magnitudes of the measured maximum redshift and blueshift are denoted by the corresponding white dashed lines.

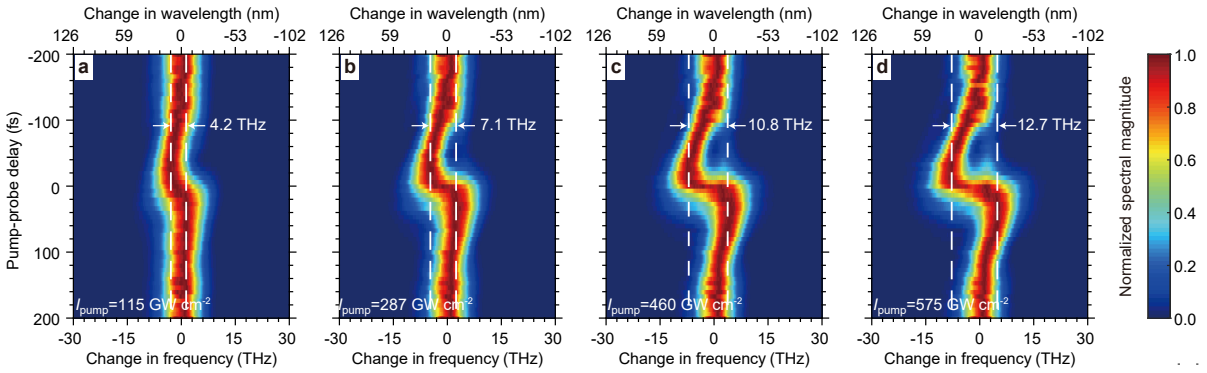

Supplementary Figure 10. a-d, The experimentally measured spectra of 1060 nm probe pulse at different pump intensities. The magnitudes of the measured maximum redshift and blueshift are denoted by the corresponding white dashed lines.

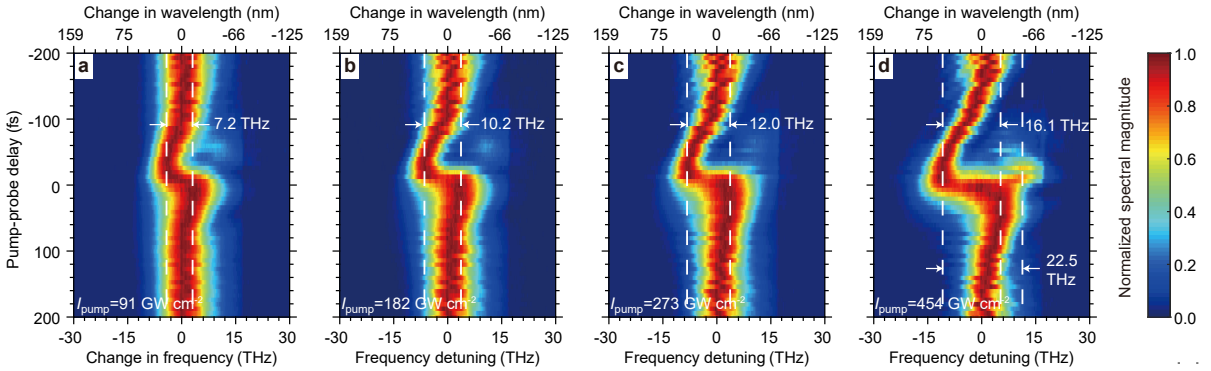

Supplementary Figure 11. a-d, The experimentally measured spectra of 1184 nm probe pulse at different pump intensities. The magnitudes of the measured maximum redshift and blueshift are denoted by the corresponding white dashed lines. The subpanel **d** also shows the an additional blueshifted peak (6.4 THz) due to the effective fifth-order nonlinear process.

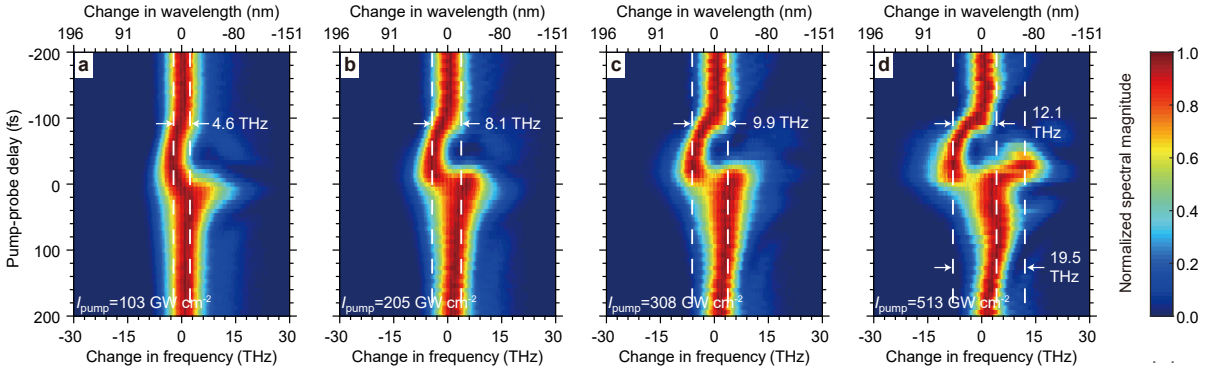

Supplementary Figure 12. a-d, The experimentally measured spectra of 1305 nm probe pulse at different pump intensities. The magnitudes of the measured maximum redshift and blueshift are denoted by the corresponding white dashed lines.The subpanel **d** also shows the an additional blueshifted peak (7.4 THz) due to the effective fifth-order nonlinear process.

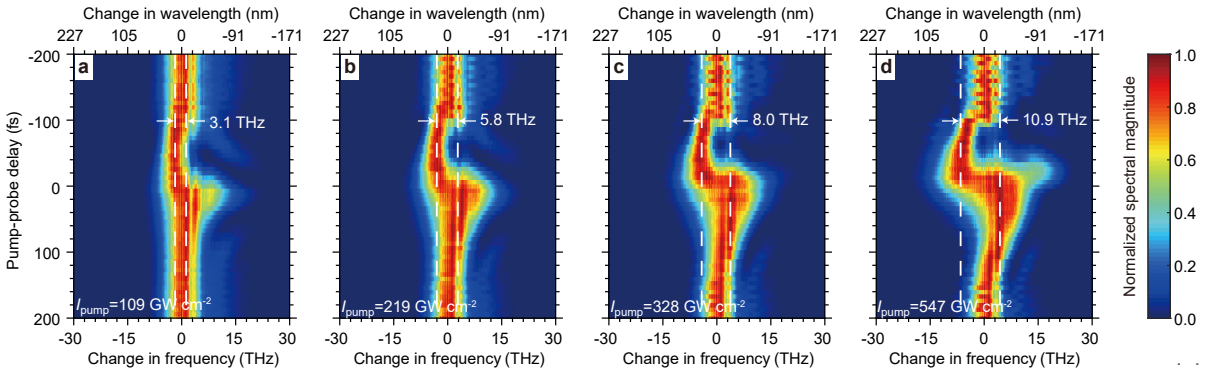

Supplementary Figure 13. a-d, The experimentally measured spectra of 1398 nm probe pulse at different pump intensities. The magnitudes of the measured maximum redshift and blueshift are denoted by the corresponding white dashed lines.

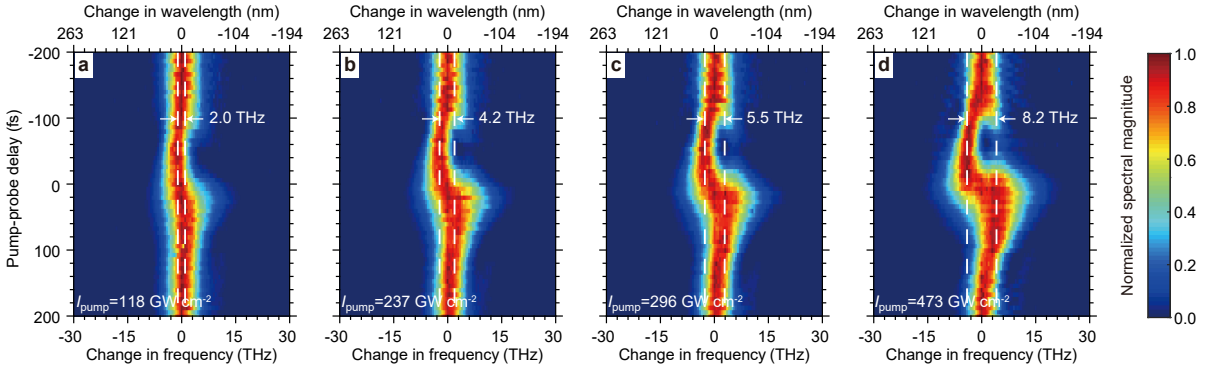

Supplementary Figure 14. a-d, The experimentally measured spectra of 1495 nm probe pulse at different pump intensities. The magnitudes of the measured maximum redshift and blueshift are denoted by the corresponding white dashed lines.

Supplementary Note 6: Analysis of the air gap between ITO films

In our experiment, we form a 620-nm-thick medium by sandwiching two commercially available 310-nm-thick ITO films deposited on 1.1-mm-thick glass. However, a white-light interferometric measurement reveals that there remains an air gap between two layers of the ITO thin films. We measure the air gap to be roughly 2200 nm thick. Air has a higher refractive index than ITO at the wavelengths of interest (e.g. $n_{\mathrm{ITO}} = 0.42 + 0.42\mathrm{i}$ at $\lambda_0 = 1240$ nm) and the air gap has a thickness slightly larger than the free-space wavelength. Thus one may expect that there is an unintended weak cavity effect due to thin film interference effects for our structure. However we posit that this unintended air gap affects our results minimally for two reasons. First, compared to ITO the nonlinear response of the air gap at the pump intensities relevant for this experiment is negligible. Second, the effective third-order nonlinear response of ITO leads to an increase in refractive index at all wavelengths of interest in this work. Thus at high pump intensities for which the frequency translation of the probe pulses are the largest, the thin-film interference effects effectively disappears.

Supplementary References

1. Agrawal, G. P. *Nonlinear fiber optics* (Springer, 2000).

2. Boyd, R. W. *Nonlinear optics* (Elsevier, 2003).

3. Plansinis, B. W., Donaldson, W. R. & Agrawal, G. P. What is the temporal analog of reflection and refraction of optical beams? *Phys. Rev. Lett.* **115**, 183901 (2015).

4. Alam, M. Z., De Leon, I. & Boyd, R. W. Large optical nonlinearity of indium tin oxide in its epsilon-near-zero region. *Science* **352**, 795–797 (2016).

5. Trebino, R. et al. Measuring ultrashort laser pulses in the time-frequency domain using frequency-resolved optical gating. *Rev. Sci. Instrum.* **68**, 3277–3295 (1997).

6. Dekker, R. et al. Ultrafast kerr-induced all-optical wavelength conversion in silicon waveguides using 1.55 μm femtosecond pulses. *Opt. Express* **14**, 8336–8346 (2006).

7. Xiao, Y., Maywar, D. N. & Agrawal, G. P. Reflection and transmission of electromagnetic waves at a temporal boundary. *Opt. Lett.* **39**, 574–577 (2014).

8. Xiao, Y. *Propagation of optical pulses in dynamic media: a time transformation method* (PhD thesis, University of Rochester, 2014).

9. Vampa, G. et al. Light amplification by seeded kerr instability. *Science* **359**, 673–675 (2018).

7 ENHANCED SPIN-ORBIT COUPLING IN AN EPSILON-NEAR-ZERO MATERIAL

CONTRIBUTION STATEMENT:

This project started as a collaboration with Peter Banzer when Robert Fickler and I were attending WEH-Seminar on "Nanophotonics and Complex Spatial Modes of Light" in Bad Honnef, Germany in 2016. At the time we were interested in strong focusing dynamics in ENZ materials. After almost a year in the discussion stage, we finally decided to perform the experiment. By the time we initiated the experiment, a paper by Ciattoni et al. was published which theoretically predicted some of the effects we were interested in[1]. I contributed in designing the experiment and supervised laboratory measurements by L. Ackermann during her visit to Ottawa. I also performed numerical simulations and wrote the first draft of the manuscript.

1 A. Ciattoni, A. Marini, and C. Rizza, "Efficient vortex generation in subwavelength epsilon-near-zero slabs," Physical Review Letters 118, 104301 (2017)

Research Article Vol. X, No. X / July 2019 / Optica 1

Enhanced Spin-Orbit Coupling in an Epsilon-Near-Zero Material

M. Zahirul Alam[1], Lisa Ackermann[2], Joerg Eismann[2,3], Sergey Nechayev[2,3], Robert Fickler[1,4], Peter Banzer[2,3], and Robert W. Boyd[1,5]

[1] Department of Physics, University of Ottawa, Ottawa, ON K2P 2M8, Canada
[2] Max Planck Institute for the Science of Light, Staudtstr. 2, D-91058 Erlangen, Germany
[3] Institute of Optics, Information and Photonics, University Erlangen-Nuremberg, Staudtstr. 7/B2, D-91058 Erlangen, Germany
[4] Photonics Laboratory, Physics Unit, Tampere University, Tampere, FI-33720, Finland
[5] The Institute of Optics, University of Rochester, Rochester, New York 14627, USA

Compiled June 24, 2020

Light can carry both spin and orbital angular momentum. It is known that a conversion from spin to orbital angular momentum of light naturally occurs at the focal plane of a nonparaxially focused circularly polarized beam. However, that angular momentum conversion is spatially localized at the focal plane and vanishes upon collimation of the nonparaxial beam into a paraxial one. Here, we experimentally show that a permanent conversion of spin-to-angular momentum can naturally occur from a nonparaxial field due to the asymmetry in the Fresnel coefficients in the presence of a homogeneous isotropic thin film of arbitrary dielectric constant. We also show that the conversion efficiency can be significantly enhanced in the presence of an epsilon-near-zero thin film due to the highly nonparaxial nature of light-matter interaction.

OCIS codes:

http://dx.doi.org/10.1364/optica.XX.XXXXXX

A circularly polarized photon carries spin angular momentum of $\pm\hbar$ due to the nature of the electric field polarization vector. In addition, a spatially structured photon with a helical phase front can carry orbital angular momentum (OAM) of $\pm l\hbar$, where l is the number of windings in the phase front and is an integer [1–3]. The polarization and the spatial degrees of freedom of a light beam are typically taken to be decoupled in standard paraxial optics. Thus, when one changes the polarization of a light beam using a half-wave plate, the spatial mode does not change. However, when light interacts with wavelength-scale inhomogeneities of a material, the propagation of a particular OAM mode can become dependent on the spin degree of freedom. This effect is somewhat analogous to the spin-orbit interaction of electrons in a solid and is known as the spin-orbit interaction (SOI) of light [4–7]. Such spatial modes of light have been used to probe fundamental light-matter interactions, which has led to the finding of a number of promising applications in classical and quantum optics including optical manipulation, trapping, superresolution imaging, high dimensional quantum communication, selective excitation of modes in nanoparticles etc. [2, 6, 8–15]. A light beam carrying OAM can be generated in various ways: cavities, astigmatism, forked holograms, spiral phase plates, and spatial light modulators [16–19]. All of these techniques rely on introducing phase discontinuity in the wavefront and do not necessarily depend on the polarization of the input light beam. In contrast, structures made of Berry phase elements can be used to convert a beam carrying only the spin angular momentum of light into a beam carrying OAM by using a q-plate, dielectric or plasmonic antenna array that introduce position-dependent geometric phases and holograms [20–23]. Furthermore, spin-orbit interac-

Research Article Vol. X, No. X / July 2019 / Optica 2

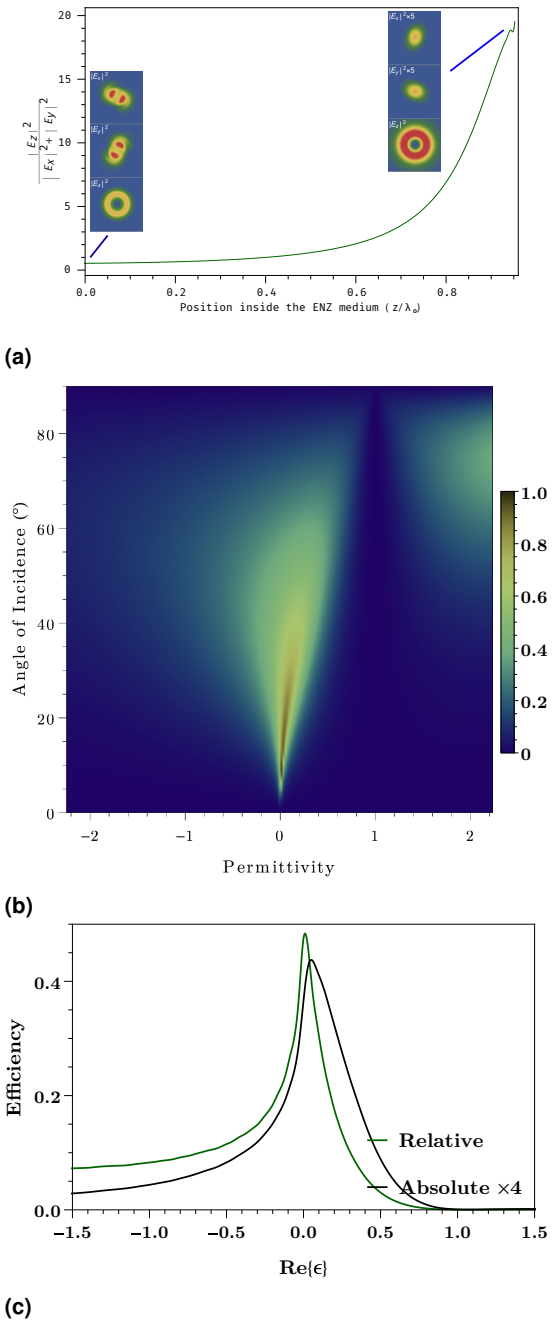

Fig. 1. a) When a circularly polarized nonparaxial light beam propagates in an ENZ medium ($\epsilon = 0.0001 + 0.0003i$), the z-polarized component of the electric field grows in relative strength to become the dominant electric field component. b) The absolute value of difference in Fresnel transmission coefficients of TE and TM polarized light for a 300-nm-thick film. c) The relative and absolute efficiency of permanent conversion from spin angular momentum to paraxial OAM with the opposite handedness.

tion naturally arises in the Fourier plane of a nonparaxial circularly symmetric focused field [24–26]. However, upon collimation to the paraxial regime, the effect simply disappears. In this paper, we show that the spin-orbit coupling that naturally arises in a nonparaxially focused circularly polarized beam can be used to produce propagating paraxial OAM modes of $l = \pm 2$ in the presence of a thin film at the focal plane. The permanent conversion from a circular polarization, of left or right handedness, to an OAM mode of opposite handedness with $l = \pm 2$ occurs due to the polarization-dependent asymmetry in Fresnel coefficients. Thus, the effect is present for any type of optical interface. Furthermore, we show that the efficiency of conversion of spin angular momentum to orbital angular momentum is significantly enhanced in the presence of an epsilon-near-zero (ENZ) thin film.

The behaviour of light at an interface is determined by the complex values of the relative permittivities (ϵ) and the relative permeabilities (μ) of materials on the both sides of the interface. At optical frequencies, a nonmagenetic material has unit permeability and thus the values of the relative permittivites of the two materials primarily dictate the light-matter interactions at the interface. A material is defined as a dielectric or metal if $\epsilon \geq 1$ and $\epsilon \leq -1$ respectively. Since the turn of the century, there has been growing research interest in understanding and utilizing the light-matter interaction in materials with vanishingly small permittivities, otherwise known as epsilon-near-zero (ENZ) materials. Such a material has a permittivity value that lies between ± 1 ($-1 < \epsilon < 1$). In general the permittivity of a material is a complex number, and if the imaginary part is small while the real part is zero or near zero, the refractive index is also near zero ($n = \sqrt{\epsilon}$). Consequently, the wavelength ($\lambda = \lambda_0/n$) inside the medium gets stretched, the phase velocity ($v = c/n$) diverges, and the electric field becomes spatially "static-like" over the entire material while oscillating in time. Epsilon-near-zero materials allow tunneling of electromagnetic waves through deep subwavelength narrow channels and arbitrary bends, enhances the directivities of antennas, and leads to strong nonlinear light-matter interactions [27–31]. Due to the stretching of wavelength, the propagation of the light beam in such a medium can become highly nonparaxial (i.e. the beam waist on the order of the effective wavelength inside the medium). It has been shown that nonparaxial focusing of a circularly polarized Gaussian beam gives rise to a conversion of the spin angular momentum to orbital angular momentum at the focal plane [24–26]. Since the wavelength is stretched in an ENZ medium and due to the fact that an obliquely incident k-vector bends away from the surface normal, a nonparaxial light beam becomes even more nonparaxial as it enters an ENZ medium, leading to a much stronger conversion of spin angular momentum to orbital angular momentum in a low index medium.

The propagation of a Gaussian light beam (Gaussian amplitude distribution in the transverse xy plane) and its

Research Article Vol. X, No. X / July 2019 / Optica 3

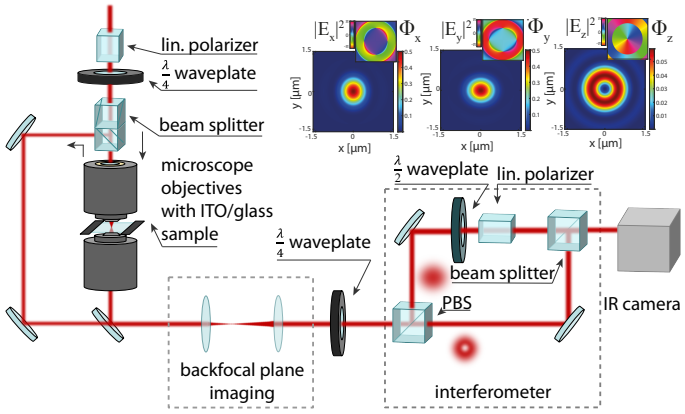

(a)

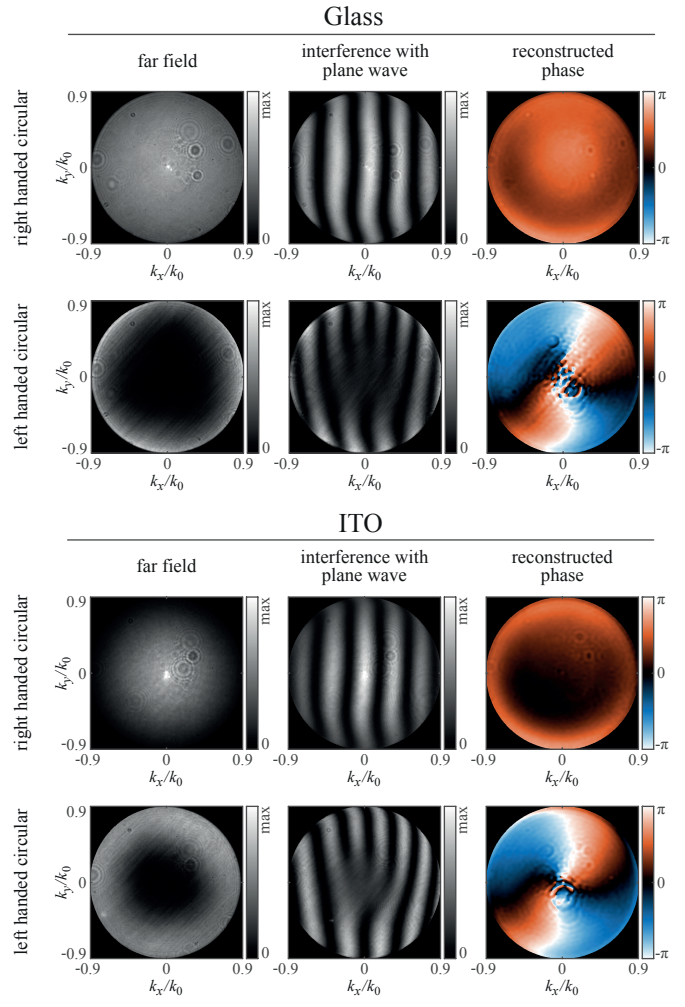

(b)

Fig. 2. a) Experimental setup. b) The image of the measured intensity and phase profiles of two arms of the interferometer part of the setup above. We measured interference and the phase structures for both a microscope slide and 310-nm-thick ITO on glass. at the focus of the high-NA objectives in the experimental setup.

interaction with a material can be described using paraxial wave equations if the the transverse beam size is much larger than the wavelength of light, i.e. the electric field does not appreciably change in amplitude within one wavelength of light along the direction of propagation (along z) [32]. Thus, in the Fourier space a well defined k-vector with minimum spread is used to describe the light-matter interaction. The beam divergence – a measure of how quickly a beam spreads in the transverse plane as it propagates – is inversely proportional to the beam waist. Thus, if the waist or spot size of the beam is on the order of wavelength, a large spread of k-vectors are needed due to a large beam divergence to describe the light-matter interaction. A high numerical aperture (NA) objective can focus light to a spot size that is on the order of the free-space wavelength of light. The light-matter interaction at the focal plane of such as objective is described by the rules of nonparaxial optics and requires a large spread of k-vectors to be modeled [33]. It has been reported by several authors that when focused using a high-NA objective, a circularly polarized light beam (with right or left helicity) leads to an excitation of an electric field distribution that carries orbital angular momentum. For example, let us assume that we are focusing a right circularly polarized Gaussian beam with zero orbital angular momentum using a high NA objective. Within the context of ray optics, a high-NA objective rotates a meridional ray proportional to the NA of the lens and produces a conical distribution of k-vectors at the focal plane within a solid angle defined by the NA of the lens. Since polarization is always defined with respect to the plane transverse to the k-vector, the plane of the polarization also rotates by an angle defined by the NA. Due to this 3D rotational transformation of the electric field by the lens, and the requirement that the total angular momentum (spin and orbital angular momentum) of light transformed by a rotationally symmetric lossless system is always conserved, the z-polarized component of the electric field acquires a circular polarization of opposite handedness with a vortex component with $l = 2$, i.e. has an azimuthal phase. The excitation of the OAM component at the focal plane has been experimentally verified through rotation of gold particles. The relative magnitude of the z-component carrying the orbital angular momentum component is directly proportional to the NA of the optical system [25]. However, typically only a small fraction of the overall power is carried by the component. As a next step we will discuss that if focused onto an epsilon-near-zero material, the z-polarized component can become much stronger compared to the transverse components.

Let us now consider propagation of a light beam that is nonparaxially focused at hte interface between air and an ENZ material. If one places a slab of material with near-zero permittivity at the focal region, Fresnel refraction requires that the refracted angle inside the medium of a non-normal k-vector –light is incident from air– is larger than the incident angle and consequently, the beam

Research Article Vol. X, No. X / July 2019 / Optica 4

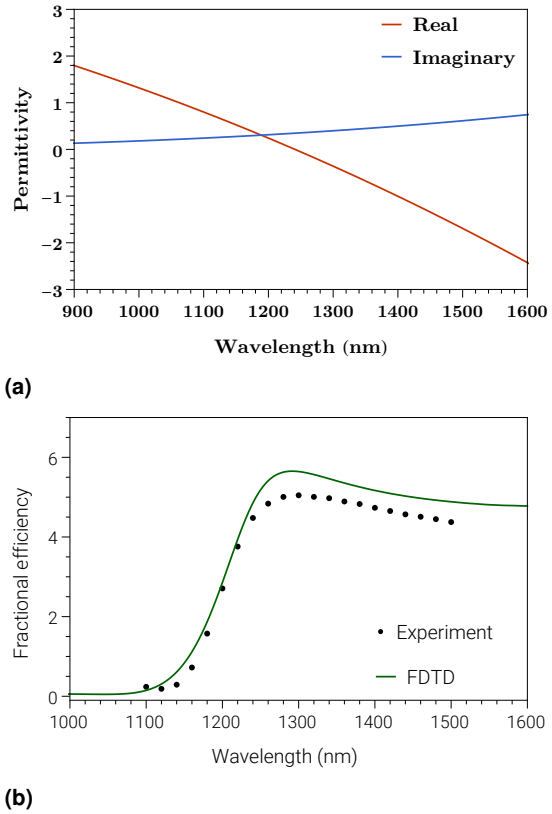

Fig. 3. a) The permittivity of ITO as measured using a spectroscopic ellipsometer. (b) Theoratically calculated and measured fractional efficiency. The fractional efficiency is defined as the the ratio of the power of the vortex carrying beam to that of the total output light.

becomes even more nonparaxial. In general, if the plane-wave spectrum of a beam is not small with respect to the radius of the circle ($= 1/(\lambda/n)$) centered at the origin in the Fourier space, the beam is considered to be nonparaxial. Thus, as refractive index approaches zero, the radius of the circle vanishes, such that in the limit of $\epsilon \to 0 + 0i$ ($Re\{n\} \to 0$) even a paraxial k-vector can produce nonparaxial light due to a larger divergence of the beam and a significant stretching of the wavelength ($\lambda = \lambda_0/c$). However, in this work we focus on the case where a nonparaxially focused beam – that is, nonparaxially focused in air – enters into an ENZ medium from air. To understand the coupling strength between the spin angular momentum to orbital angular momentum, we will look into the relative strength of the z-component of the electric field of strongly focused beam in an ENZ medium. Figure 1a shows how the z-component of the electric field varies as a function of propagation distance inside an ENZ medium ($\epsilon = 0.001 + 0.0003i$). It can be seen that as the beam propagates z-component of the electric field gets larger at the expense of the transverse components. For a sufficiently long propagation distance, the power carried by the z-component can even become many times larger than the transverse components. This occurs due to the remarkable fact that the propagation of light in an ENZ medium is highly nonparaxial due to the effective stretching of the wavelength ($\lambda = lambda_0/\sqrt{\epsilon}$). In a lossy ENZ medium the real part of the refractive index approaches zero but does not completely vanish. Nevertheless, even in a lossy ENZ material a beam that is nonparaxial in air can become significantly more nonparaxial. Thus, the spin-orbit interaction of light naturally occurs in nonparaxial optics, and can dominate the behaviour of light propagation in an ENZ medium.

The polarization-dependent asymmetry in the Fresnel coefficient and the strong interaction of spin and angular momentum can be used to generate paraxial OAM with $l = \pm 2$ efficiently. It is well known that the Fresnel coefficients for any interface depend on the angle of incidence and the polarization. The difference in the Fresnel transmission coefficients for TE and TM polarized light is largest when the permittivity of a thin film approaches zero. The impedance of an infinitely thick ENZ medium is infinite suggesting that no light can be coupled into such a medium. However, the transmittance of a transversely magnetic (TM) polarized plane wave through an ENZ slab is inversely proportional to the electrical thickness of the slab [31]. Furthermore, TM light of near-zero angle of incidence shows a large tunneling through such a medium. In contrast, a TE polarized plane wave shows no such anomalous large transmission coefficient even when the permittivity is near zero. Figure 1b shows permittivity-dependent difference in transmission for a 300-nm-thick film for a free space wavelength of 1 μm. It can be seen that the difference in the Fresnel transmission coefficients of TE and TM polarized waves is the largest when the relative permittivity is close to zero. The difference shows a resonance for the near-zero-permittivity due to the phase discontinuity and the anomalous tunneling for TM polarized light. The resonance broadens in the presence of loss and the peak moves to a larger angle of incidence.

The strong Fresnel transmission asymmetry and the large spin-to-orbit conversion that happens in an ENZ medium leads to a permanent generation of OAM beams with $l = \pm 2$, where the sign depends on the handedness of the input circular polarization. Figure 1c shows permittivity-dependent conversion efficiency for a 300-nm-thick medium placed on the focus of a high-NA lens (NA =0.9). Both relative and absolute conversion efficiencies have resonances for vanishing permittivity. We define relative efficiency as the ratio of power in the OAM component to the total output power, and absolute efficiency as the ratio of power in the OAM component at the output to total incident power. We now verify these effects experimentally.

Figure 2a shows the experimental setup. A linearly polarized beam from a supercontinuum source that is spectrally filtered is sent through a linear Glan-Taylor polarizer and a quarter wave plate to introduce circular polarization of either left or right handedness. We used a high-NA

Research Article Vol. X, No. X / July 2019 / Optica 5

(NA=0.9) microscope objective to tightly focus the Gaussian beam onto the target sample. The objective enables tight focusing of the beam to roughly a micron spot size in air. The transmitted light is collected with a high NA = 1.3 immersion oil microscope objective in confocal alignment to collimate the output beam. As the converted and non-converted beams have opposite handedness, they can be separated as follows. We use a quarter wave plate to project each circular polarization components to a linear basis, i.e. convert into vertical or horizontal polarizations. A polarizing beam splitter (PBS) is then used to divide both parts in two separate beam paths. We then record the far field patterns and the angular spectra of the two separated beams. The back focal plane can be imaged optionally with a set of two lenses in 4f configuration. We record the converted and the non-converted beams with an infrared camera. To verify that the converted beam possesses the predicted OAM with $l = \pm 2$, we perform a phase measurement with a Mach-Zehnder interferometer. The two output beams from the two output ports of the PBS are interfered on a camera after letting one of the beams pass through a half waveplate and a linear polarizer so that both beams have the same polarization and amplitude at the plane of the interference. We used the recorded spectra to reconstruct the azimuthal phase of the OAM beam [34]. We then also reconstructed the transverse phase of the OAM-carrying beam to remove all ambiguity. The interference pattern recorded by the camera depends on the carrier frequency and the transverse phase. The transverse phase can be reconstructed by applying a series of transformations: Fourier transform the interference pattern; filtering to get rid of the carrier frequency and the lower sideband; frequency translation of the leftover upper sideband to the zero frequency; and finally, we do an inverse Fourier transform and take the natural logarithm of the inverse Fourier. The imaginary part of the logarithm returns the transverse phase of the OAM beam.

In order to verify the effect we did two sets of experiments. In the first set of experiments we measured the efficiency of conversion and the investigated the intensity and phase profile of the output beam by following the procedures described above using a simple microscope slide. We chose the microscope slide to show that spin-to-orbit conversion can be achieved using a generic interface. Figure 2b shows the interference patterns for glass. The presence of two fork dislocations in the interference fringe and the two 2π windings in the reconstructed phase confirms that the generated OAM beam has a topology $l = 2$. We measured the fractional conversion efficiency for glass to be 0.53% and 0.62% for right and left handed polarzed input light beam.

In the second set of experiments we measured the wavelength-dependent conversion efficiencies using a 310-nm-thick ITO layer on a glass substrate, as well as the intensity and the phase profile of the output beam (2b). ITO is a highly doped semiconductor. At the near-

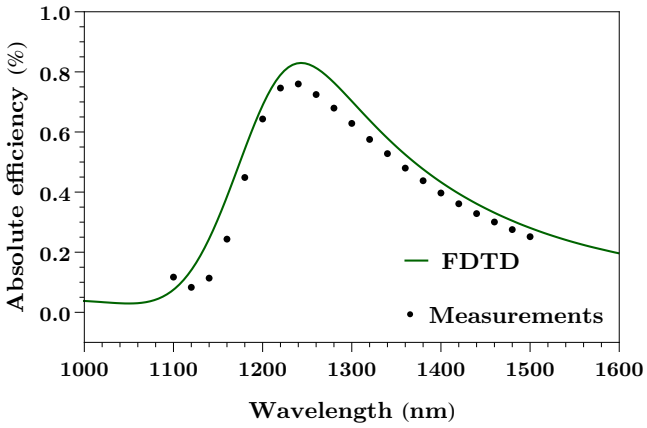

Fig. 4. (a) Absolute conversion efficiency as a function of wavelength and permittivity.

IR frequency, the permittivity of ITO can be modeled using Drude parameters. Figure 3a shows the permittivity of ITO as a function of wavelength. Thus, a set of wavelength-dependent measurements in the spectral range of 1100 nm to 1500 nm allows us to measure the conversion efficiencies as a function of permittivity. These measurements also allow us to probe the effect of low refractive index. In the spectral range of interest the permittivity of ITO goes from a value slightly less than 1 to a negative value of -2. We find that at 1100 nm the permittivity of ITO is $0.8 + 0.25i$ and the conversion efficiency is 0.23% (input is right handed circularly polarized). The conversion efficiency steadily increases as we tune the laser to a longer wavelength and reach a peak. We find that the maximum fractional conversion efficiency is not obtained at the zero-crossing wavelength of $\sim$ 1240 nm but at a slightly larger wavelength of 1280 nm where $\epsilon = -0.235809 + 0.381i$. The fractional conversion efficiency is both a function of the real and the imaginary part of the index. Due to the finite imaginary part of the permittivity, the refractive index does not reach zero when the real part of the permittivity is zero, and for our material the real part of the refractive index continues to decrease as the wavelength is increased. At the same time, the imaginary part of the refractive index also increases with increase in the wavelength. The interplay of both parameters then lead to a peak at a wavelength which is slightly longer than the zero-permittivity wavelength. Nevertheless, the maximum fractional conversion efficiency of 5% at 1280 nm wavelength is roughly 10 times larger than what was obtained at 1100 nm or that obtained for a simple air-glass interface. We note that a beam with a free space wavelength of 1280 nm has an effective wavelength of larger than 3 μm inside the ITO layer. Thus, a beam that is nonparaxial in air due to high-NA focusing becomes even more nonparaxial inside the ITO layer resulting in a stronger spin-orbit coupling. For an incident wavelength that is longer than the zero permittivity wavelength, the relative conversion efficiency slowly decreases because

Research Article Vol. X, No. X / July 2019 / Optica 6

of the existence of a fairly large imaginary part of the index. To verify the experimental result we subsequently performed a series of FDTD simulations. We find that the fractional conversion efficiency measured agrees well with the FDTD results although there is a constant offset, and we measure a slightly lower efficiency than what is expected based on the FDTD calculations. We attribute these differences primarily to the calibration uncertainties of the detector and to Fresnel reflection as the light passes through various optical elements placed before the detectors after the confocal arrangements.

In Figure 4 we show the absolute conversion efficiency, that is, the ratio of the power in the OAM carrying beam to the total incident power. Since the measurement of the incident beam power after a tight focusing objective is problematic, we take the wavelength-dependent transmittance values obtained in the FDTD simulation and the measured relative efficiency to calculate the absolute efficiency. The absolute efficiency is a product of the transmittance and the fractional efficiency. It can easily be seen that the absolute efficiency also shows a peak at the low permittivity wavelength. Specifically, we note that the peak of the absolute efficiency is at 1240 nm, which is exactly the wavelength where the ITO has zero real permittivity. The absolute efficiency goes up as the permittivity goes down from a positive value to zero and then the efficiency goes down as the permittivity becomes negative (and the transmittance also goes down due to the negative values of the permittivity). Nevertheless, we note that the absolute efficiency show a pole at the zero permittivity wavelength.

In conclusion, we have shown that the spin angular momentum to orbital angular momentum conversion that occurs at the focal plane of a high-NA objective can be made permanent with the presence of any interface. This occurs primarily due to the asymmetry in the Fresnel coefficients. Furthermore, the effect is greatly enhanced in the presence of an ENZ medium due to the effective stretching of the wavelength and the presence of a pole in the differential Fresnel transmission coefficient for TE and TM light. We note that an even larger conversion efficiency can be achieved if the imaginary part of the permittivity be lowered as that sets the floor of the refractive index at the ENZ wavelengths [35, 36]. Furthermore, the propagation of a paraxial beam in air can become nonparaxial in an ENZ material if the absorption is low or if perimittivity and the permeability are both simulateneously zero resulting in near-zero refractive index. For such a material the enhanced spin-to-orbit conversion can be observed even for a beam that is paraxial in air and not require a tight focusing geometry. Our findings have implications in the nonlinear propagation of optical beam in an ENZ medium, designing ENZ-based metasurfaces, and for designing nanophotonic devices that exploit the spin-orbit-interactions. We also note that the large nonlinearity that is typically associated with an ENZ medium can be used to introduce dynamic control of the spin-to-orbit coupling in nanophotonics [30].

ACKNOWLEDGEMENT

REFERENCES

1. R. A. Beth, "Mechanical detection and measurement of the angular momentum of light," Phys. Rev. **50**, 115 (1936).
2. L. Allen, S. Barnett, and M. Padgett, *Optical Angular Momentum* (CRC Press, 2016).
3. L. Allen, M. W. Beijersbergen, R. J. C. Spreeuw, and J. P. Woerdman, "Orbital angular momentum of light and the transformation of laguerre-gaussian laser modes," Phys. Rev. A **45**, 8185–8189 (1992).
4. K. Y. Bliokh, F. Rodríguez-Fortuño, F. Nori, and A. V. Zayats, "Spin–orbit interactions of light," Nat. Photonics **9**, 796 (2015).
5. A. T. O'Neil, I. MacVicar, L. Allen, and M. J. Padgett, "Intrinsic and extrinsic nature of the orbital angular momentum of a light beam," Phys. Rev. Lett. **88**, 053601 (2002).
6. N. B. Simpson, K. Dholakia, L. Allen, and M. J. Padgett, "Mechanical equivalence of spin and orbital angular momentum of light: an optical spanner," Opt. Lett. **22**, 52–54 (1997).
7. H. He, M. E. J. Friese, N. R. Heckenberg, and H. Rubinsztein-Dunlop, "Direct observation of transfer of angular momentum to absorptive particles from a laser beam with a phase singularity," Phys. Rev. Lett. **75**, 826–829 (1995).
8. E. Brasselet, Y. Izdebskaya, V. Shvedov, A. S. Desyatnikov, W. Krolikowski, and Y. S. Kivshar, "Dynamics of optical spin-orbit coupling in uniaxial crystals," Opt. letters **34**, 1021–1023 (2009).
9. P. Banzer, U. Peschel, S. Quabis, and G. Leuchs, "On the experimental investigation of the electric and magnetic response of a single nano-structure," Opt. express **18**, 10905–10923 (2010).
10. A. Mair, A. Vaziri, G. Weihs, and A. Zeilinger, "Entanglement of the orbital angular momentum states of photons," Nature **412**, 313 (2001).
11. J. Wang, J.-Y. Yang, I. M. Fazal, N. Ahmed, Y. Yan, H. Huang, Y. Ren, Y. Yue, S. Dolinar, M. Tur *et al.*, "Terabit free-space data transmission employing orbital angular momentum multiplexing," Nat. photonics **6**, 488 (2012).
12. N. Bozinovic, Y. Yue, Y. Ren, M. Tur, P. Kristensen, H. Huang, A. E. Willner, and S. Ramachandran, "Terabit-scale orbital angular momentum mode division multiplexing in fibers," science **340**, 1545–1548 (2013).
13. R. Fickler, R. Lapkiewicz, W. N. Plick, M. Krenn, C. Schaeff, S. Ramelow, and A. Zeilinger, "Quantum entanglement of high angular momenta," Science **338**, 640–643 (2012).
14. J. Leach, B. Jack, J. Romero, A. K. Jha, A. M. Yao, S. Franke-Arnold, D. G. Ireland, R. W. Boyd, S. M.

Barnett, and M. J. Padgett, "Quantum correlations in optical angle–orbital angular momentum variables," Science **329**, 662–665 (2010).
15. S. W. Hell and J. Wichmann, "Breaking the diffraction resolution limit by stimulated emission: stimulated-emission-depletion fluorescence microscopy," Opt. letters **19**, 780–782 (1994).
16. F. Manni, K. G. Lagoudakis, T. Paraïso, R. Cerna, Y. Léger, T. C. H. Liew, I. Shelykh, A. V. Kavokin, F. Morier-Genoud, and B. Deveaud-Plédran, "Spin-to-orbital angular momentum conversion in semiconductor microcavities," Phys. Rev. B **83**, 241307 (2011).
17. M. W. Beijersbergen, L. Allen, H. Van der Veen, and J. Woerdman, "Astigmatic laser mode converters and transfer of orbital angular momentum," Opt. Commun. **96**, 123–132 (1993).
18. V. Y. Bazhenov, M. Soskin, and M. Vasnetsov, "Screw dislocations in light wavefronts," J. Mod. Opt. **39**, 985–990 (1992).
19. A. M. Yao and M. J. Padgett, "Orbital angular momentum: origins, behavior and applications," Adv. Opt. Photonics **3**, 161–204 (2011).
20. L. Marrucci, C. Manzo, and D. Paparo, "Optical spin-to-orbital angular momentum conversion in inhomogeneous anisotropic media," Phys. review letters **96**, 163905 (2006).
21. E. Karimi, B. Piccirillo, L. Marrucci, and E. Santamato, "Light propagation in a birefringent plate with topological charge," Opt. letters **34**, 1225–1227 (2009).
22. A. Niv, Y. Gorodetski, V. Kleiner, and E. Hasman, "Topological spin-orbit interaction of light in anisotropic inhomogeneous subwavelength structures," Opt. letters **33**, 2910–2912 (2008).
23. R. C. Devlin, A. Ambrosio, N. A. Rubin, J. B. Mueller, and F. Capasso, "Arbitrary spin-to–orbital angular momentum conversion of light," Science **358**, 896–901 (2017).
24. T. A. Nieminen, A. B. Stilgoe, N. R. Heckenberg, and H. Rubinsztein-Dunlop, "Angular momentum of a strongly focused gaussian beam," J. Opt. A: Pure Appl. Opt. **10**, 115005 (2008).
25. Y. Zhao, J. S. Edgar, G. D. Jeffries, D. McGloin, and D. T. Chiu, "Spin-to-orbital angular momentum conversion in a strongly focused optical beam," Phys. Rev. Lett. **99**, 073901 (2007).
26. K. Y. Bliokh, E. A. Ostrovskaya, M. A. Alonso, O. G. Rodríguez-Herrera, D. Lara, and C. Dainty, "Spin-to-orbital angular momentum conversion in focusing, scattering, and imaging systems," Opt. express **19**, 26132–26149 (2011).
27. N. Engheta, "Pursuing near-zero response," Science **340**, 286–287 (2013).
28. R. W. Ziolkowski, "Propagation in and scattering from a matched metamaterial having a zero index of refraction," Phys. Rev. E **70**, 046608 (2004).
29. M. Silveirinha and N. Engheta, "Tunneling of electromagnetic energy through subwavelength channels and bends using ε-near-zero materials," Phys. review letters **97**, 157403 (2006).
30. M. Z. Alam, I. De Leon, and R. W. Boyd, "Large optical nonlinearity of indium tin oxide in its epsilon-near-zero region," Science **352**, 795–797 (2016).
31. A. Alu, M. G. Silveirinha, A. Salandrino, and N. Engheta, "Epsilon-near-zero metamaterials and electromagnetic sources: Tailoring the radiation phase pattern," Phys. review B **75**, 155410 (2007).
32. S. Nemoto, "Nonparaxial gaussian beams," Appl. optics **29**, 1940–1946 (1990).
33. B. Richards and E. Wolf, "Electromagnetic diffraction in optical systems. ii. structure of the image field in an aplanatic system," in "Proceedings of the Royal Society of London A: Mathematical, Physical and Engineering Sciences," , vol. 253 (The Royal Society, 1959), vol. 253, pp. 358–379.
34. M. Takeda, H. Ina, and S. Kobayashi, "Fourier-transform method of fringe-pattern analysis for computer-based topography and interferometry," JosA **72**, 156–160 (1982).
35. A. Ciattoni, A. Marini, and C. Rizza, "Efficient vortex generation in subwavelength epsilon-near-zero slabs," Phys. review letters **118**, 104301 (2017).
36. Y. Li, S. Kita, P. Muñoz, O. Reshef, D. I. Vulis, M. Yin, M. Lončar, and E. Mazur, "On-chip zero-index metamaterials," Nat. Photonics **9**, 738 (2015).

8 CONCLUSION

In this thesis, I have presented six research publications on the linear and the nonlinear responses of epsilon-near-zero materials.

In the introductory chapter, I tried to give the intuition as to why in a zero-permittivity material the nonlinear response can become the dominant optical response. This view challenges the long-standing assumptions of nonlinear response, namely that the nonlinear optical responses are only perturbative to the linear optical response. The results presented in Chapters 2 and 5 should convince a reader the value of the above claim.

We have shown in Chapters 3 and 4 how strong-coupling-induced dynamics between low-Q plasmonic antennas and a thin ENZ film can be used to design nonlinear optical nanostructures with a tailored sign at a wavelength of interest while simultaneously enhancing both Δn by a few times and the nonlinear refractive index coefficient n_2 by three orders of magnitude compared to the bare ENZ film. Specifically, we note that the $\Delta n \approx \pm 2.5$ extracted from such material at a sub-ps timescale is larger than the linear refractive index of most materials at the visible and near-IR frequencies.

In Chapter 7 we have presented how the time refraction effect can be used to translate the carrier frequency of an optical pulse by nearly 15 THz using a sub-wavelength-thick ENZ material. The performance of our system, defined as frequency shift per unit propagation length, is four to seven orders of magnitude larger than all previously demonstrated solid-state systems [14]–[18]. We note that with the advent of high powered lasers large adiabatic frequency conversions have been demonstrated using plasmas [19]–[21]. The typical interaction lengths in a gaseous plasma are a few hundred microns. In contrast, we demonstrated appreciable frequency shifts in ITO with four to eight orders of magnitude lower pump intensity as well as at least four orders of magnitude shorter interaction length. Furthermore, ionization of a high-pressure gas jet system is not suitable for integration, whereas our we used a CMOS-compatible material. Furthermore, AWC resulting from laser-induced ionization exhibits only a limited redshift due to

the long relaxation time of gaseous plasma and thus lacks tunability in the sign of frequency shift.

8.1 CONCLUDING REMARKS

Perhaps the holy grail of research in modern nanophotonics is to find efficient ways for the complete spatiotemporal control of the vectorial nature of a light field by another light field. For these techniques to be technologically relevant the required interaction volume must be much smaller than λ^3. In this aspect, our findings that the low linear refractive index of a material can dictate how strong the nonlinear optical responses a material possess is a breakthrough in furthering our understanding of light-matter interactions in the nanoscale.

We have used indium tin oxide, a highly doped semiconductor, as an ENZ medium. The zero-permittivity in such a material arises from a large density of free electrons in the conduction band. In contrast, laser excitation near the phonon resonance of a material can show show ENZ behaviour in the mid-IR frequency range. On the other hand, metamaterial-based implementations can exhibit ENZ response—as per the effective medium approximation—from the UV to RF. It is not entirely clear how agnostic the nonlinear enhancement is to the specific mechanisms underlying the ENZ response. It is also worth investigating as to what parameters set the upper limit for the maximum achievable nonlinear changes in the refractive index in each class of ENZ materials. Furthermore, it is likely that in Drude-type ENZ materials and in highly correlated oxides and nitrides the collective dynamics of electrons play a strong role in determining the magnitude of the nonlinear response. It would be worth investigating the coherence properties of such dynamics, and to see if there are any emergent or topological aspects to these interactions in nanostructured ENZ materials. The integration of plasmonic nanostructures as shown in Chapters 3 and 4 present unique opportunities to implement all-optical control to mold the far-field pattern of an optical field with low pump power. This particular technique can be extended to be used in silicon-based integrated optical platforms. For example, one can envision an optical switch that is designed by incorporating a single ENZ-based nonlinear plasmonic or dielectric antenna on the cladding of a waveguide for controlling the propagation dynamics of the guided modes.

Similarly, there are exciting opportunities in achieving ultrafast control of quantum properties of emitters embedded in an ENZ medium. The spontaneous emission rate of an emitter depends on the local density of optical states (LDOS). The spontaneous emission rate of an emitter can be dynamically controlled by varying the LDOS. ENZ materials present unique opportunities in this aspect for three reasons. First, the near-zero refractive index of an ENZ material suggests that spontaneous emission is suppressed inside such a material. Second, the large ultrafast nonlinear change in the refractive index provides a way of controlling the LDOS in an ultrafast manner. Furthermore, a large, ultrafast, and localized change to the LDOS can be imparted by modulating the optical properties of nanostructures such as dynamically tuning the resonance wavelength of plasmonic cavities in the vicinity of an ENZ medium. It is not clear as to what happens to the quantum state of an emitter if the density of the state is modified in a nonadiabatic but periodic manner. This gives rise to an interesting question. Is there a specific topological nature to the emission dynamics that can be impressed on to quantum emitters experiencing a large time-periodic modulation of the density of states? Research in this direction will also allow one to investigate the nonlinear properties of thermal emission in ENZ materials.

In the above discussion, I have raised a few questions motivated by the results presented in this thesis. It is clear that the extraordinarily large change in refractive index in ENZ materials raises many research questions and opportunities. As such this field is poised to be very active for the next decade.

BIBLIOGRAPHY

[1] N. Bloembergen, "Nonlinear optics: Past, present, and future," *IEEE Journal of Selected Topics in Quantum Electronics*, vol. 6, no. 6, pp. 876–880, 2000.

[2] R. W. Boyd, *Nonlinear optics*. Elsevier, 2003.

[3] R. W. Boyd, "The impact of Charles H. Townes on nonlinear optics," *IEEE Journal of Selected Topics in Quantum Electronics*, vol. 6, no. 6, pp. 881–884, 2000.

[4] D. M. Pozar, *Microwave engineering*. John Wiley & Sons, 2009.

[5] A. Alu, M. G. Silveirinha, A. Salandrino, and N. Engheta, "Epsilon-near-zero metamaterials and electromagnetic sources: Tailoring the radiation phase pattern," *Physical review B*, vol. 75, no. 15, p. 155 410, 2007.

[6] B. Edwards, A. Alù, M. E. Young, M. Silveirinha, and N. Engheta, "Experimental verification of epsilon-near-zero metamaterial coupling and energy squeezing using a microwave waveguide," *Physical review letters*, vol. 100, no. 3, p. 033 903, 2008.

[7] R. Liu, Q. Cheng, T. Hand, J. J. Mock, T. J. Cui, S. A. Cummer, and D. R. Smith, "Experimental demonstration of electromagnetic tunneling through an epsilon-near-zero metamaterial at microwave frequencies," *Physical review letters*, vol. 100, no. 2, p. 023 903, 2008.

[8] R. W. Ziolkowski, "Propagation in and scattering from a matched metamaterial having a zero index of refraction," *Physical Review E*, vol. 70, no. 4, p. 046 608, 2004.

[9] S. Enoch, G. Tayeb, P. Sabouroux, N. Guérin, and P. Vincent, "A metamaterial for directive emission," *Physical Review Letters*, vol. 89, no. 21, p. 213 902, 2002.

[10] J. Brown, "Artificial dielectrics having refractive indices less than unity," *Proceedings of the IEE-Part IV: Institution Monographs*, vol. 100, no. 5, pp. 51–62, 1953.

[11] M. Silveirinha and N. Engheta, "Tunneling of electromagnetic energy through subwavelength channels and bends using ε-near-zero materials," *Physical review letters*, vol. 97, no. 15, p. 157 403, 2006.

[12] I. Liberal and N. Engheta, "Nonradiating and radiating modes excited by quantum emitters in open epsilon-near-zero cavities," *Science advances*, vol. 2, no. 10, e1600987, 2016.

[13] P. W. Milonni, J. R. Ackerhalt, and W. A. Smith, "Interpretation of radiative corrections in spontaneous emission," *Physical Review Letters*, vol. 31, no. 15, p. 958, 1973.

[14] G. P. Agrawal, P. Baldeck, and R. Alfano, "Temporal and spectral effects of cross-phase modulation on copropagating ultrashort pulses in optical fibers," *Physical Review A*, vol. 40, no. 9, p. 5063, 1989.

[15] J. Li, B.-E. Olsson, M. Karlsson, and P. A. Andrekson, "Otdm add-drop multiplexer based on xpm-induced wavelength shifting in highly nonlinear fiber," *Journal of lightwave technology*, vol. 23, no. 9, p. 2654, 2005.

[16] R. Dekker, A. Driessen, T. Wahlbrink, C. Moormann, J. Niehusmann, and M. Först, "Ultrafast kerr-induced all-optical wavelength conversion in silicon waveguides using 1.55 μm femtosecond pulses," *Optics express*, vol. 14, no. 18, pp. 8336–8346, 2006.

[17] P. Mehta, N. Healy, T. Day, J. V. Badding, and A. Peacock, "Ultrafast wavelength conversion via cross-phase modulation in hydrogenated amorphous silicon optical fibers," *Optics express*, vol. 20, no. 24, pp. 26 110–26 116, 2012.

[18] S. Preble, Q. Xu, and M. Lipson, "Changing the color of light in a silicon resonator," in *Frontiers in Optics*, Optical Society of America, 2006, PDP_FC2.

[19] E. Yablonovitch, "Self-phase modulation of light in a laser-breakdown plasma," *Physical Review Letters*, vol. 32, no. 20, p. 1101, 1974.

[20] W. M. Wood, C. Siders, and M. Downer, "Measurement of femtosecond ionization dynamics of atmospheric density gases by spectral blueshifting," *Physical review letters*, vol. 67, no. 25, p. 3523, 1991.

[21] N. Lopes, G. Figueira, J. Dias, L. Silva, J. Mendonça, P. Balcou, G. Rey, and C. Stenz, "Laser pulse frequency upshifts by relativistic ionization fronts," *EPL (Europhysics Letters)*, vol. 66, no. 3, p. 371, 2004.